

# Classical and quantum phases of low-dimensional dipolar systems

Dissertation  
zur Erlangung des Grades  
des Doktors der Naturwissenschaften  
der Naturwissenschaftlich-Technischen Fakultät  
der Universität des Saarlandes

und

l'Université Grenoble Alpes

von  
Florian Cartarius

Saarbrücken  
2016

Tag des Kolloquiums: 22.09.2016

m.d.W.d.G.b. Dekan: Univ.-Prof. Dr. Christoph Becher

Mitglieder des Prüfungsausschusses: Univ.-Prof. Dr. Giovanna Morigi  
Dr. Anna Minguzzi  
Univ.-Prof. Dr. Jordi Boronat  
Dr. Chiara Menotti  
Univ.-Prof. Dr. Ludger Santen  
Univ.-Prof. Dr. Julia Meyer  
Dr. Bruno Laburthe-Tolra

---

## Eidesstattliche Erklärung

---

Hiermit versichere ich an Eides statt, dass ich die vorliegende Arbeit selbstständig und ohne Benutzung anderer als der angegebenen Hilfsmittel angefertigt habe. Die aus anderen Quellen oder indirekt übernommenen Daten und Konzepte sind unter Angabe der Quelle gekennzeichnet. Die Arbeit wurde bisher weder im In- noch im Ausland in gleicher oder ähnlicher Form in einem Verfahren zur Erlangung eines akademischen Grades vorgelegt.

**Ort, Datum**

---

**Unterschrift**

---



---

## Short abstract

---

In this thesis we present a detailed study of the phase diagram of ultracold bosonic atoms confined along a tight atomic wave guide, along which they experience an optical lattice potential. In this quasi-one dimensional model we analyse the interplay between interactions and quantum fluctuations in (i) determining the non-equilibrium steady state after a quench and (ii) giving rise to novel equilibrium phases, when the interactions combine the s-wave contact interaction and the anisotropic long range dipole-dipole interactions. In detail, in the first part of the thesis we study the depinning of a gas of impenetrable bosons following the sudden switch off of the optical lattice. By means of a Bose-Fermi mapping we infer the exact quantum dynamical evolution and show that in the thermodynamic limit the system is in a non-equilibrium steady state without quasi-long range order. In the second part of the thesis, we study the effect of quantum fluctuations on the linear-zigzag instability in the ground state of ultracold dipolar bosons, as a function of the strength of the transverse confinement. We first analyse the linear-zigzag instability in the classical regime, and then use our results to develop a multi-mode Bose-Hubbard model for the system. We then develop several numerical methods, to determine the ground state.



---

## Zusammenfassung

---

In dieser Arbeit präsentieren wir die detaillierte Untersuchung des Phasendiagramms von ultrakalten bosonischen Atomen, welche in einem engen Wellenleiter gefangen sind, entlang dessen ein optisches Gitter läuft. In diesem eindimensionalen Modell analysieren wir das Zusammenspiel zwischen Wechselwirkungen und Quantenfluktuationen und (i) bestimmen den Nichtgleichgewichtszustand nach einem Quench und (ii) führen zu neuen Quantenphasen, in denen die Wechselwirkung sich aus der s-Wellen-Kontaktwechselwirkung und den anisotropen langreichweitigen Dipol-Dipol-Wechselwirkung zusammensetzen. Im Detail wird im ersten Teil der Arbeit das Depinning von einem Bose-Gas mit harten Kernen untersucht, nachdem das optische Gitter plötzlich ausgeschaltet wird. Mit Hilfe eines Bose-Fermi-Mappings kann man die exakte dynamische Entwicklung ableiten und zeigen, dass im thermodynamischen Limes das System sich in einen Zustand ohne quasi-langreichweitige Korrelationen begibt. Im zweiten Teil wird der Effekt von Quantenfluktuationen auf den Linear-Zigzag-Übergang im Grundzustand ultrakalter dipolaren Bosonen als Funktion der transversalen Falle untersucht. Zuerst analysieren wir die Instabilität im klassischen Bereich und benutzen dann unsere Resultate um ein Bose-Hubbard-Modell mit mehreren Moden aufzustellen. Wir benutzen mehrere numerische Methoden um den Grundzustand zu bestimmen und sagen ein reiches Phasendiagramm voraus.



Cette thèse étudie les phases classiques et quantiques des systèmes atomiques ou moléculaires de basse dimension en mettant un accent particulier sur le crossover dimensionnel de une à deux dimensions.

La première partie de la thèse est consacrée à la description d'un système d'atomes froids interagissants avec un potentiel de contact. Plus précisément, nous étudions le dé-piégeage dynamique qui, suite à l'extinction rapide d'un réseau optique, s'opère dans un gaz composé de bosons impénétrables dans un guide d'onde atomique linéaire. Nous employons une solution exacte, basée sur une correspondance entre bosons en forte interaction et fermions sans interaction pour déduire l'évolution dynamique quantique exacte. Dans la limite thermodynamique, nous observons l'approche vers un état stationnaire hors équilibre, caractérisé par l'absence d'ordre hors diagonal à longue distance et une visibilité réduite de la distribution en impulsions. Des caractéristiques similaires sont observées dans un système de taille finie pour des temps correspondant à la moitié du temps de récurrence, lors desquels nous observons que le système approche un état quasi-stationnaire auquel le système s'approche avec une dépendance temporelle en loi de puissance.

La deuxième partie de la thèse analyse l'effet des interactions dipolaires sur l'état fondamental du système. L'inclusion de l'interaction dipôle-dipôle donne lieu à de nouvelles phases quantiques du système unidimensionnel, mais peut également entraîner une instabilité transverse.

Cette instabilité est tout d'abord analysée dans le régime classique. Nous considérons des particules classiques avec interactions dipolaires, confinés sur un anneau par un potentiel harmonique radiale. Les dipôles sont polarisés perpendiculairement au plan de confinement. En diminuant le confinement dans la direction radiale, les particules classique montrent une transition entre une chaîne simple et une chaîne double (en zigzag). Nous montrons que cette transition est faiblement du premier ordre. Nous expliquons que la nature de cette transition est déterminée par le couplage entre les modes d'excitation transversaux et axiaux de la chaîne des dipôles. Ce résultat est très différent du comportement observé dans les systèmes Coulombiens, où la transition entre la chaîne linéaire et la chaîne en zigzag est continue et appartient à la classe d'universalité de la transition ferromagnétique. Nos résultats s'appliquent aux systèmes dipolaires classiques et aux atomes Rydberg, qui peuvent constituer un banc d'essai pour simuler le comportement critique des aimants couplés à

des grilles.

Dans le régime quantique, nous considérons un système des bosons dipolaires sur un réseaux optique, confinés par un potentiel harmonique anisotrope. Dans le régime favorisant l'instabilité d'une chaîne simple, nous démontrons que le système peut être décrit par un modèle de Bose-Hubbard étendu à plusieurs modes couplés entre eux, dont les coefficients peuvent être déterminés en utilisant une théorie de basse énergie. La méthode d'intégrale de chemin Monte Carlo, la diagonalisation exacte et TEBD sont utilisés pour déterminer l'état fondamental de modèle de Bose-Hubbard étendu et démontrent que ce modèle capture la transition entre la chaîne linéaire et la chaîne en zigzag.

---

## Abstract

---

In this work, the classical and quantum phases of low-dimensional atomic or molecular systems is studied with a particular focus on the regime where a system goes over from a strictly one-dimensional to a two dimensional system.

The first part of the thesis is dedicated to atoms interacting via contact interactions. In particular, we study the dynamical depinning following a sudden turn off of an optical lattice for a gas of impenetrable bosons in a tight atomic waveguide. We use an exact solution, which is based on an equivalence between strongly interacting bosons and noninteracting fermions, in order to derive the exact quantum dynamical evolution. At long times, in the thermodynamic limit, we observe the approach to a nonequilibrium steady state, characterized by the absence of quasi-long-range order and a reduced visibility in the momentum distribution. Similar features are found in a finite-size system at times corresponding to half the revival time, where we find that the system approaches a quasisteady state with a power-law behavior.

In the second part, we study the effect of additional dipolar interactions on the ground state of the system. The inclusion of dipole-dipole interaction leads to new quantum phases of the one-dimensional system, but can also lead to a transverse instability.

This instability is first analyzed in the classical regime. We study classical particles with dipolar interactions, that are confined on a chain by a harmonic potential. The dipoles are polarised perpendicular to the plane of confinement. Classical particles with repulsive power-law interactions undergo a transition from a single to a double chain (zigzag) by decreasing the confinement in the transverse direction. We theoretically characterize this transition when the particles are classical dipoles, polarized perpendicularly to the plane in which the motion occurs, and argue that this transition is of first order, even though weakly. The nature of the transition is determined by the coupling between transverse and axial modes of the chain and contrasts with the behavior found in Coulomb systems, where the linear-zigzag transition is continuous and belongs to the universality class of the ferromagnetic transition. Our results hold for classical dipolar systems and Rydberg atoms, which can offer a test bed for simulating the critical behavior of magnets with lattice coupling.

In the quantum regime, we consider dipolar bosons in an optical lattice, tightly confined by an anisotropic harmonic potential. In the regime where a single chain becomes unstable, we show that the system can be mapped onto

an extended multi-mode Bose-Hubbard model, where the coefficients can be determined by means of a low energy theory. A path integral Monte Carlo method, exact diagonalization and TEBD are used to determine the ground state of the extended Bose-Hubbard models. and show that the model captures the linear to zigzag transition.

---

# Contents

---

<b>Introduction</b>	<b>1</b>
<b>1 Introduction</b>	<b>1</b>
<b>I Neutral atoms in optical lattices</b>	<b>3</b>
<b>2 Ultracold atoms in optical lattices</b>	<b>5</b>
2.1 The optical lattice . . . . .	5
2.2 Strong lattices . . . . .	8
2.3 Weak lattices . . . . .	11
<b>3 Dynamical depinning of a Tonks Girardeau gas</b>	<b>13</b>
3.1 Model and exact solution . . . . .	14
3.2 Time evolution of the density profiles . . . . .	16
3.3 The non-equilibrium steady state . . . . .	16
3.4 First-order coherence and momentum distribution . . . . .	17
3.5 Conclusions and outlook . . . . .	21
<b>II Interacting dipoles</b>	<b>23</b>
<b>4 Atomic Dipolar gases</b>	<b>25</b>
4.1 Dipole-Dipole interaction . . . . .	25
4.2 Interacting dipoles in low dimensions . . . . .	27
<b>5 The classical limit</b>	<b>29</b>
5.1 Microscopic model . . . . .	29
5.2 Stability of the linear chain . . . . .	30
5.3 Minimum configurations . . . . .	32
5.4 Low energy description of the transition . . . . .	37
5.5 Finite-size system . . . . .	42

<b>6</b>	<b>The quantum regime</b>	<b>49</b>
6.1	The structural transition for pinned particles . . . . .	49
6.2	Derivation of the multi-mode Bose-Hubbard model . . . . .	52
6.3	Observables and Phases . . . . .	56
6.4	Phase diagrams . . . . .	61
6.5	Time Evolving Block Decimation . . . . .	68
6.6	Conclusion and Outlook . . . . .	73
<b>7</b>	<b>Conclusions</b>	<b>77</b>
<b>A</b>	<b>The 2d effective potential</b>	<b>79</b>
<b>B</b>	<b>Path Integral Monte Carlo</b>	<b>81</b>
<b>C</b>	<b>Time Evolving Block Decimation</b>	<b>87</b>
	<b>Bibliography</b>	<b>88</b>

# CHAPTER 1

---

## Introduction

---

The realization of isolated quantum systems has become an experimental reality with ultracold quantum gases. These systems indeed provide a unique platform for simulating dynamics and models predicted for condensed-phase systems, statistical mechanics, as well as to test quantum-field theoretical hypotheses. Strongly correlated ensembles of trapped ions, atoms and dipolar systems allow one to study and simulate Wigner crystallization [DO99, BDL<sup>+</sup>07, ABKL07], supersolidity [GSL02], and quantum magnetism [PC04, FSG<sup>+</sup>08, KCK<sup>+</sup>10], to mention a few. The interplay of quantum fluctuations, external confinement and interactions in gases of ultracold bosons is the subject of this thesis. We analyze the quantum phases under different settings and characterize the effect of quantum fluctuations at the onset of quantum and classical structures.

In chapter 2 we introduce some basic concepts of ultracold atoms in optical lattices, which will be useful for the discussion in the following chapters.

In chapter 3 we focus on hard-core bosons in one dimension and confined by an optical lattice, when the lattice is suddenly switched off. The ground state of the Hamiltonian before and after the quench is a gapped insulating state and a superfluid, respectively [BBZ03]. The steady state reached after the quench, however, is out-of-equilibrium and displays no quasi long-range order.

In chapters 4-6 we additionally consider that the bosons interact repulsively along the wave-guide by means of the dipole-dipole interaction and analyse the quantum phases as a function of the transverse confinement. The ratio between the on-site repulsion and the dipolar interaction gives rise to transitions between the Mott insulator, charge density wave and in one dimension the Haldane insulator. The interplay with the kinetic energy is expected to originate superfluid, supersolid and pair superfluid phases, whose appearance is controlled, amongst others, by the transverse density distribution.

At the same time, the transverse confinement also controls the structural stability of dipolar arrays: For repulsive interactions, when the transverse trap frequency reaches a critical value controlled by the linear density, one dimensional arrays become unstable and the dipoles tend to form a zigzag structure [AMDCB08]. While the interplay between quantum fluctuations and struc-



**Figure 1.1** – *Schematic representation of the linear to zigzag transition. In strong anisotropic confinement repulsively interacting particles arrange in a linear configuration (left). If the transverse confinement is relaxed, the linear chain splits into a zigzag (right).*

tural order is relevant to several experimental setups, yet the associated properties of the phase diagram are still unknown. This transverse instability has been studied extensively in linear arrays of ions [BKW92]. If the transverse confinement is lowered below a critical value, the ion chain will split into two, a zigzag, as shown in figure 1.1. The transition is described by a Landau model [FDCCM08], is continuous and is a quantum phase transition in the quantum regime [SMF11, SDCC<sup>+</sup>13, MML07].

In chapter 5 we first analyse the properties of the linear-zigzag instability when the particles interact via the dipole-dipole interaction. This is the starting point for the systematic derivation of a multi-mode Bose-Hubbard model, which is performed in chapter 6. This model is valid deep in the quantum regime, setting the basis for a systematic numerical characterization of the phase diagram. Here, the structure of the numerical programs, which are based on a path-integral Monte Carlo and on a TEBD method, is then detailed.

# PART I

## Neutral atoms in optical lattices



# CHAPTER 2

---

## Ultracold atoms in optical lattices

---

In this thesis we will study the phases of ultracold bosonic particles in periodic potentials. The purpose of this chapter is to introduce some basic concepts, which will be useful for the discussion in the following chapters.

### 2.1 The optical lattice

In the dipole approximation, the interaction of an atom or molecule with an electric field is given by

$$H_{\text{opt}} = -\mathbf{d} \cdot \mathbf{E}, \quad (2.1)$$

where  $\mathbf{E}$  is the electric field and  $d$  is the electric dipole moment. If the electric field stems from a laser which is far detuned from any atomic or molecular transitions, the interaction is described by the AC Stark shift and leads to the energy correction[PS08]

$$\Delta E_{\text{opt}} = -\alpha(\omega_L) \langle |\mathbf{E}(\mathbf{r})|^2 \rangle_t, \quad (2.2)$$

where  $\alpha(\omega_L)$  is the dynamic polarizability and  $\langle \dots \rangle_t$  is the time average over one oscillation period of the electric field. If the laser is far detuned from the particle resonances, the laser field acts as an effective potential in which the particles move. In this dressed atom picture the energy shift is

$$\Delta E_{\text{opt}} \propto \frac{\langle |\mathbf{E}(\mathbf{r})|^2 \rangle_t}{\hbar\Delta}, \quad (2.3)$$

where  $\Delta$  is the detuning of the laser to the next particle resonance.

For red-detuned light ( $\Delta < 0$ ), the particles are pushed towards regions of high intensity of the laser, whereas for blue detuned light ( $\Delta > 0$ ) they are pulled towards regions of low light intensity.

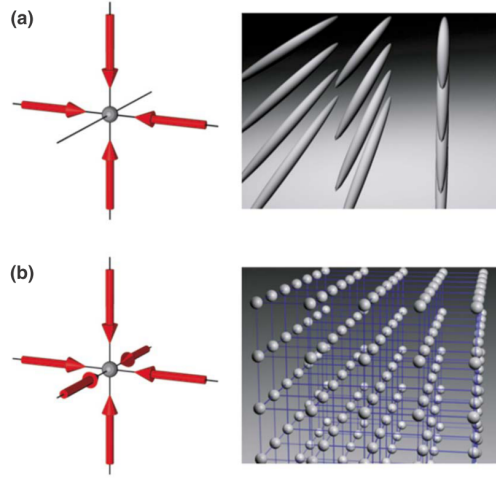


**Figure 2.1** – *Picture of an optical lattice potential taken from Bloch et al. [BDZ08]. (a) a 2D square lattice creating an array of tightly confining tubes; b) a 3D cubic lattice potential.*

By crossing three sets of counter-propagating lasers, it is possible to produce regular patterns of high and low intensity. If the lasers are aligned to produce a simple cubic pattern, the potential that the particles feel is

$$V_{\text{opt}}(\mathbf{r}) = V_x \sin^2(k_x x) + V_y \sin^2(k_y y) + V_z \sin^2(k_z z), \quad (2.4)$$

where the lattice heights  $V_\nu$  are tuned by the intensity of the lasers, and  $k_\nu$  depend on the laser frequencies. By varying the laser frequencies and lattice heights, it is possible to create quasi-1d or 2d lattices, in which the particles will arrange in. For the following calculations, we will assume that the optical lattice is simple cubic and the wave vectors are given by  $k = k_x = k_y = k_z = \pi/a$ , where  $a$  is the distance between two lattice sites.

### The scattering length and the effective contact interaction

For low energies elastic s-wave scattering dominates the scattering problem of two particles. The scattering problem for two particles is described by a single parameter, the scattering length, which is to lowest order [PS08]

$$a_{3D} = \frac{m}{4\pi\hbar} \int dr U_{\text{int}}(r). \quad (2.5)$$

The low-energy description of the two body interaction can be thought arising from an effective interaction

$$g = \int d^3r U_{\text{eff}}(\mathbf{r}) = \frac{4\pi\hbar a_{3D}}{m}. \quad (2.6)$$

The scattering remains the only important quantity for dilute gases, where three particle collisions are rare compared to two particle ones and the interaction potential falls off rapidly enough. This is for example correct for typical experiments using Alkali atoms, that interact via van-der-Waals interactions. The interaction between two particles sitting at position  $\mathbf{r}$  and  $\mathbf{r}'$  is thus proportional to a contact interaction,

$$U_{\text{eff}}(\mathbf{r} - \mathbf{r}') = g\delta(\mathbf{r} - \mathbf{r}'). \quad (2.7)$$

The scattering length can be interpreted as the radius of the atom or molecule. With Feshbach resonances it is possible to tune the scattering length by varying external magnetic fields. One can even reach regimes where the effective interaction is attractive with  $a_{3D} < 0$ , or the hard core limit with  $a_{3D} \rightarrow \infty$ .

In addition, the scattering length can be changed via the transverse confinement in low dimensional settings. If the atom is in the ground state of a transverse harmonic oscillator with oscillator length  $a_{\perp} = \sqrt{\hbar/m\omega_{\perp}}$ , where  $\omega_{\perp}$  is the oscillator frequency, the transverse wavefunction can be approximated by  $\phi_{\perp}(\rho) = e^{-\rho^2/a_{\perp}^2}/(a_{\perp}\sqrt{\pi})$ . Integrating out the transversal density in the 3D pseudopotential allows one to find the one dimensional one as [Ols98]

$$g_{1D}\delta(r) = \int d\rho \rho 2\pi |\phi_{\perp}(\rho)|^2 g_{3D}\delta(\mathbf{r}) \quad (2.8)$$

$$= \frac{2\hbar^2 a_{3D}}{ma_{\perp}^2} \delta(r). \quad (2.9)$$

This result is a good approximation of the weakly interacting system, but if the radial confinement approaches the transverse one, it breaks down and an additional term has to be included [Ols98]. The effective one dimensional coupling is then given by

$$g_{1D} = \frac{2\hbar^2 a_{3D}}{ma_{\perp}^2} \frac{1}{1 - C a_{3D}/(a_{\perp})}, \quad (2.10)$$

where  $C = -\zeta(1/2)$  and  $\zeta(x)$  is the Riemann zeta-function [Ols98]. Therefore, the radial confinement can lead to scattering resonances of the effective one-dimensional interaction.

## 2.2 Strong lattices

### 2.2.1 Wannier functions

In this section, we want to review the Bose-Hubbard model, and introduce the nomenclature for the next sections. The Hamiltonian of atomic gases in optical lattices in second quantization is  $H = H_0 + H_{\text{int}}$ , with

$$H_0 = \int d^3r \Psi^\dagger(\mathbf{r}) \left[ -\frac{\hbar^2 \nabla^2}{2m} + V_{\text{opt}}(\mathbf{r}) - \mu \right] \Psi(\mathbf{r}), \quad (2.11)$$

$$H_{\text{int}} = \frac{g}{2} \int d^3r \Psi^\dagger(\mathbf{r}) \Psi^\dagger(\mathbf{r}) \Psi(\mathbf{r}) \Psi(\mathbf{r}), \quad (2.12)$$

where  $\Psi(\mathbf{r})$  is the bosonic field operator of the atoms and  $V_{\text{opt}}$  is the optical lattice potential with period  $a$ . We work in the grand-canonical ensemble, where the number of particles is fixed by the chemical potential  $\mu$ . If the amplitude of the optical lattice is large compared to the recoil energy  $V_L \gtrsim 6E_R$ , and the temperature is low enough, it is sufficient to only consider the lowest Bloch band, provided that the interactions between the particles are small enough that they do not induce transition between the different bands. In an experiment, there is an additional harmonic confinement superimposed to the optical lattice. However, if the harmonic confinement changes on scales much larger than the optical lattice period, one may take into account the effect of confinement in an approximate way through a local-density approximation on the results of the homogeneous system. Hence, in the rest of this thesis we will not treat the effects of harmonic confinement.

As most of the thesis will discuss quasi one-dimensional systems, we will restrict the following calculations to the one-dimensional case. (The calculation for the three dimensions is identical to the one shown here.) The non interacting Hamiltonian  $H_0$  can be diagonalized by expanding the field operator on the basis of the first band Bloch's functions  $\chi_q(x)$  according to [EFG<sup>+</sup>05]

$$\Psi(x) = \sum_q \chi_q(x) a_q \quad (2.13)$$

where  $a_q$  is a bosonic field operator satisfying the commutation relations  $[a_q, a_p^\dagger] = \delta_{p,q}$ ,  $\chi_q(x)$  are the solutions of the single-particle Schroedinger equation

$$\left( -\frac{\hbar^2}{2m} \frac{\partial^2}{\partial x^2} + V_{\text{opt}}(x) \right) \chi(x) = E \chi(x)$$

and  $\pi/a < q < \pi/a$  is the quasi-momentum.

When taking into account the full interacting Hamiltonian, it is more con-

venient to write the Hamiltonian in the basis of Wannier functions, which are defined as the Fourier transform of Bloch functions [EFG<sup>+</sup>05]

$$w(x) = \frac{1}{M} \sum_q e^{-iqx} \chi_q(x), \quad (2.14)$$

where  $M$  is the number of lattice sites. Just as the Bloch functions, Wannier functions form a complete set of the non-interacting Hamiltonian and the field operator can be expanded in Wannier functions

$$\Psi(x) = \sum_i w(x - x_i) a_i, \quad (2.15)$$

where  $a_i$  destroys a particle in the site  $x_i$ . By representing the interaction part of the Hamiltonian (2.12) using the Wannier function basis (2.15) for the field operator we obtain

$$H = - \sum_{j,l} J_{j,l} a_j^\dagger a_l + \frac{1}{2} \sum_{i,j,k,l} U_{ijkl} a_i^\dagger a_j^\dagger a_k a_l - \mu \sum_j a_j^\dagger a_j, \quad (2.16)$$

where

$$J_{j,l} = - \int d^3r w^*(x - x_j) \left[ -\frac{\hbar^2 \nabla^2}{2m} + V_{\text{opt}}(x) \right] w(x - x_l), \quad (2.17)$$

$$U_{i,j,k,l} = g \int d^3r w^*(x - x_i) w^*(x - x_j) w(x - x_k) w(x - x_l). \quad (2.18)$$

Figure 2.2 shows the shape of the Wannier function for different lattice depths. The Wannier function  $w(x - x_j)$  is centered at lattice site  $x_j$  and for increasing optical lattice depth, the Wannier functions become more localized. For this reason it is sufficient to only take into account the on-site and the nearest neighbor contributions for large optical lattice depths. In this *tight-binding limit*, one finds the well known Bose-Hubbard Hamiltonian [JBC<sup>+</sup>98, LSA<sup>+</sup>07]

$$H_{\text{BH}} = -J \sum_j (a_j^\dagger a_{j+1} + a_{j+1}^\dagger a_j) + \frac{U}{2} \sum_j n_j (n_j - 1) - \bar{\mu} \sum_j n_j, \quad (2.19)$$

where  $J = J_{j,j+1}$ ,  $U = U_{j,j,j,j}$  and  $\bar{\mu} = \mu - J_{j,j}$ .

## 2.2.2 The ground state

The Bose-Hubbard Hamiltonian (2.19) has two different phases: a superfluid (SF) and a Mott insulator (MI). This can best be understood by considering

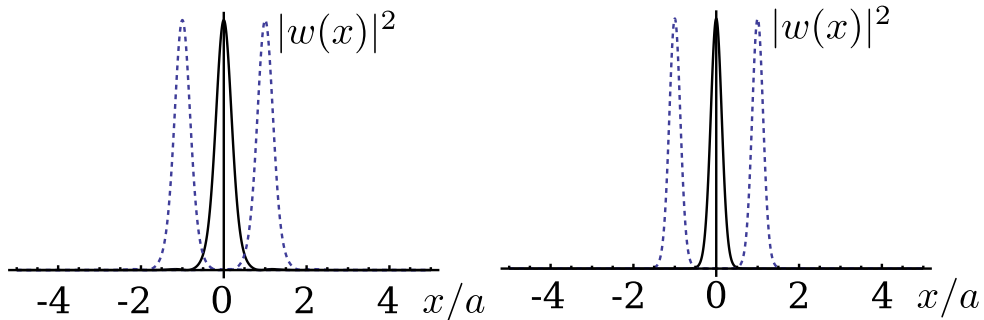


**Figure 2.2** – The 1d lowest Bloch band Wannier function centered at  $x = 0$  (black line). The dashed lines show the Wannier functions centered at adjacent lattice sites. Left for a small lattice depth  $V_L = 3E_R$ , right for  $V_L = 10E_R$ . The Wannier functions become more localized for increasing optical lattice depth.

the two limiting cases of large and small tunneling.

In the limit of small interactions  $U/|J| \ll 1$  the eigenstates are Bloch states, which are completely delocalized over the whole lattice. This gapless superfluid state is well approximated by [BDZ08]

$$|\Psi\rangle \sim \left( \sum_{j=1}^M a_j^\dagger \right)^N |\text{vac}\rangle,$$

where  $N$  is the number of particles,  $M$  the number of lattice sites and  $|\text{vac}\rangle$  denotes the vacuum state.

In the limit  $U/|J| \rightarrow \infty$ , the density fluctuations are fully suppressed and in the ground state there is an integer number of particles at each site. This gapped ground state is called the Mott Insulator. If  $\bar{n}$  is the particle number per site, the ground state wave function is [BDZ08]

$$|\Psi(\bar{n})\rangle = \prod_{j=1}^M \frac{(a_j^\dagger)^{\bar{n}}}{\sqrt{\bar{n}}} |\text{vac}\rangle.$$

The chemical potential must be in the range  $\bar{n} - 1 < \mu/U < \bar{n}$ , for it to be the ground state.

The MI as well as the SF phase extends to finite values of  $U/|J|$  and the regions of fixed density per site with zero density fluctuations are called Mott lobes. The boundary between the two phases can be estimated using a mean field approach or can be calculated numerically. In Chapter 6.4.3, we show how to calculate the ground state using a path integral Monte Carlo method, and in chapter 6.5 we discuss a TEBD method that can be used to calculate the

ground state.

## 2.3 Weak lattices

If the optical lattice is commensurate with the particle density, i.e. the atom density is inversely proportional to the lattice spacing  $n \sim 1/a$ , for strong interactions, any arbitrarily weak optical lattice will pin the particles in a gapped state and only for no optical lattice the ground state is gapless. This is called pinning transition [HHM<sup>+</sup>10].

For weak optical lattices, it is not possible to expand the wave function in the lowest Bloch band Wannier functions, as the particles can occupy multiple vibrational bands. The system may be rather described by including the lattice as a perturbation on top of an interacting, homogenous quantum fluid. A low energy description is given by the sine-Gordon Hamiltonian [BBZ03]

$$H = \frac{\hbar v_s}{2\pi} \int dx \left[ (\partial_x \theta)^2 + (\partial_x \phi)^2 + \frac{V_L n \pi}{\hbar v_s} \cos(\sqrt{4K}\theta) \right], \quad (2.20)$$

which describes a one dimensional gas, where  $\theta$  and  $\phi$  are the density and phase fields, respectively and  $v_s$  is the sound velocity. Phase and density are related via the commutation relation  $[\partial_x \theta(x), \phi(x')] = i\pi \delta(x - x')$ .

The sine-Gordon Hamiltonian has been studied extensively in solid state and high energy physics [GNT04]. The Luttinger parameter  $K = \frac{\hbar \pi n}{m v_s}$  determines the quasi long-range order of correlation functions of the unperturbed Hamiltonian with  $V_L = 0$ , such as  $\langle n(0)n(x) \rangle \sim |x|^{-2K}$ . For weak optical lattices, a perturbative renormalization group approach predicts that the system undergoes a quantum phase transition at  $K = K_C = 2$ . For  $K < K_C$  the system is in a Mott state, for  $K > K_C$  in an ungapped superfluid phase.

In the regime of strong interactions, the Luttinger parameter is related to the Lieb-Liniger parameter  $\gamma$  via  $K = (1 + 2/\gamma)^2$  [BBZ03], where  $\gamma = mg/(\hbar^2 n)$ . Feshbach resonances allow one to tune the interaction strength and thus  $\gamma$  and  $K$ . In the Tonks-Girardeau limit ( $\gamma \gg 1$ ) any arbitrarily weak optical lattice is enough to push the system into an insulating phase. This pinning transition has been first predicted in [BBZ03] and first observed in [HHM<sup>+</sup>10]. In chapter 3, we study a quench across the pinning transition.

Ultracold atomic gases confined by tight waveguides have been experimentally realized and the strongly interacting regime has been reached and characterized in detail [PWM<sup>+</sup>04, KWW04, vAvEW<sup>+</sup>08, PZSK09]. In this one-dimensional geometry, the pinning transition has been experimentally observed for atoms subjected to a longitudinal weak optical lattice [HHM<sup>+</sup>10].



## CHAPTER 3

---

### Dynamical depinning of a Tonks Girardeau gas

---

This chapter is based on:

- FLORIAN CARTARIUS, EIJI KAWASAKI, AND ANNA MINGUZZI,  
Dynamical depinning of a Tonks-Girardeau gas,  
*Phys. Rev. A* **92**, 063605 (2015).

The study of the dynamics following a quantum quench in isolated quantum systems allows one to address fundamental questions in quantum many-body systems (see, e.g., Ref. [CC06] as well as Ref. [SC14] and references therein). In one-dimensional integrable systems a relevant issue is the absence of thermalization as observed in the paradigmatic quantum Newton's cradle experiment [KWW06]. The concept of the generalized Gibbs ensemble has been introduced and developed to describe the state of integrable systems at long times [RDY07, Caz06, CK12, IC09].

In this chapter we analyze a quench across the pinning transition. In detail, we start in the pinned phase and consider a bosonic gas in the limit of infinite interactions in an optical lattice that is commensurate with the bosonic density [LŠBG12]. We follow its time evolution following a sudden turn off of the lattice while keeping the one-dimensional waveguide still present. This allows us to study the quench from an initially pinned, insulating ground state to an out-of-equilibrium depinned state. We describe the dynamical evolution of the system at arbitrary times using an exact mapping solution due to Girardeau [Gir60] and Girardeau and Wright [GW00]. This exact solution allows us to obtain the full dynamical solution for the quantum dynamics, going beyond the low-energy Luttinger-liquid model or conformal field theory approaches. Our method allows us also to study the approach in time to the non-equilibrium steady state. Finally, we focus on the experimentally relevant condition of a finite-size system, choosing a geometry that is amenable to experimental realization with ultracold atoms, e.g., by implementing a one-dimensional box-potential confinement to which an optical lattice is superimposed.

### 3.1 Model and exact solution

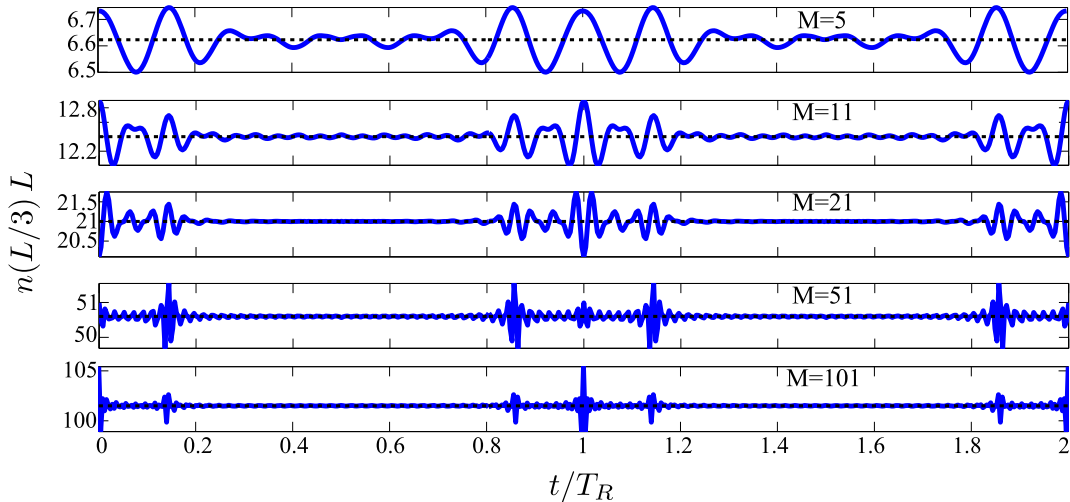


**Figure 3.1** – Time evolution of the particle density  $n(L/7, t)$  at position  $x = L/7$  as a function of time  $t$  for a commensurately filled lattice for various values of boson numbers as indicated in each panel. The horizontal dashed lines correspond to the (quasi) steady-state prediction in Eq. (3.9).

We consider  $M$  bosons of mass  $m$  at zero temperature, confined by a longitudinal box trap of size  $L$ . They are described by the Hamiltonian

$$\mathcal{H} = \sum_j \left[ -\frac{\hbar^2}{2m} \frac{\partial^2}{\partial x_j^2} + V(x_j) \right] + g \sum_{j < \ell} \delta(x_j - x_\ell). \quad (3.1)$$

The atoms are subjected to an optical lattice and to a box potential, ie  $V(x) = V_L \cos^2(k_L x) + V_b(x)$ , where  $k_L = M\pi/L$  and the box trap  $V_b(x)$  is described by imposing hard-walls boundary conditions on the interval  $[0, L]$ . The number of bosons is chosen such as to ensure unitary filling of the lattice. The interactions among the atoms is modelled by contact interactions of strength  $g$ . In the following we shall focus on the impenetrable-boson or Tonks-Girardeau limit corresponding to the limit  $g \rightarrow \infty$ . This amounts to replacing the interaction term in the Hamiltonian (3.1) by the cusp condition  $\Psi(\dots x_j = x_\ell \dots) = 0$ , imposing the vanishing of the wavefunction at contact for each pair of particles  $\{j, \ell\}$ .

At time  $t = 0^-$  we assume that the gas is at equilibrium in the optical lattice. We study the time evolution of the gas following a sudden quench of the lattice amplitude  $V_L$  to zero. The exact dynamics is described by the time-dependent Bose-Fermi mapping, stating that the time evolution of the bosonic

wavefunction  $\Psi_B(x_1 \dots x_M, t)$  can be obtained in terms of the one of a non-interacting Fermi gas subjected to the same time-dependent external potential according to

$$\Psi_B(x_1 \dots x_M, t) = \prod_{1 \leq j < \ell \leq M} \text{sign}(x_j - x_\ell) \Psi_F(x_1, x_2, \dots, x_M, t), \quad (3.2)$$

where  $\Psi_F(x_1, x_2, \dots, x_M, t) = \frac{1}{\sqrt{M!}} \det[\psi_j(x_k, t)]$ . Note that the solution (3.2) satisfies the cusp condition at all times. The single-particle orbitals  $\psi_j(x_k, t)$  are the solution of the time-dependent one-body Schrödinger equation

$$-\frac{\hbar^2}{2m} \partial_x^2 \psi_j(x, t) + V_b(x) \psi_j(x, t) = i\hbar \partial_t \psi_j(x, t), \quad (3.3)$$

As initial condition  $\psi_j(x, 0)$  we take the equilibrium single-particle problem in the presence of the lattice, corresponding to a Mathieu equation with hard walls boundary conditions,

$$-\frac{\hbar^2}{2m} \partial_x^2 \psi_j(x) + [V_L \cos^2(k_L x) + V_b(x)] \psi_j(x) = E_j \psi_j(x). \quad (3.4)$$

In the following it will be useful to scale all the energies in units of the recoil energy  $E_R = \hbar^2 k_L^2 / 2m$ , and set  $\lambda = V_L / E_R$ . The solution of Eq.(3.4) is given by a generalization of Mathieu functions. It amounts to search for a solution of the form  $\psi_j(x) = \sqrt{2/L} \sum_n b_n^{(j)} \sin(n\pi x/L)$  and determine the coefficients  $b_n^{(j)}$ . Substitution onto the Schrödinger equation (3.4) yields the linear algebra problem

$$\sum_n \sin(nk_L x) (b_n^{(j)} (n^2/M^2 - a) + q(b_{n+2M}^{(j)} + b_{n-2M}^{(j)})) = 0 \quad (3.5)$$

where  $a = E_j/E_R - \lambda/2$ ,  $q = \lambda/4$ . Equation (3.5) corresponds to an eigenvalue problem on a semi-infinite matrix. For the ground state of the TG gas we are interested in the first  $M$  eigenvalues and eigenvectors. These are obtained by numerical diagonalization, performing a truncation to a matrix size  $S \gg M$ . The time evolution of the single-particle orbitals after the sudden depinning is then readily given by

$$\psi_j(x, t) = \sqrt{2/L} \sum_n b_n^{(j)} e^{-i\varepsilon_n t/\hbar} \sin(n\pi x/L), \quad (3.6)$$

where  $\varepsilon_n = \hbar^2 (n\pi/L)^2 / 2m$ .

## 3.2 Time evolution of the density profiles

In order to explore the post-quench dynamics we analyze the time evolution of various observables. We consider first the time evolution of the density profile. This is obtained, using the Bose-Fermi mapping, as the one of the corresponding Fermi gas,

$$n(x, t) = \sum_j^M |\psi_j(x, t)|^2. \quad (3.7)$$

Substitution of the explicit solution for the lattice problem yields

$$\begin{aligned} n(x, t) &= \frac{2}{L} \sum_j^M \sum_{n, n'} e^{-i(\varepsilon_n - \varepsilon_{n'})t/\hbar} b_n^{(j)} b_{n'}^{(j)} \\ &\times \sin(n\pi x/L) \sin(n'\pi x/L). \end{aligned} \quad (3.8)$$

The time evolution of the density is shown in Fig. 3.1 for various numbers of bosons and several fixed sizes, at constant filling of one boson per site. Recurrences are clearly visible, as expected for a finite-size system. While one could estimate as trivial recurrence time  $T = 2\pi\hbar/\varepsilon_1$ , we note that the density profiles show revivals at earlier time  $T_R = T/4M$ . This property is specific to our choice of system and initial state. The time evolution in Eq. (3.8) is determined by the energy difference  $\varepsilon_n - \varepsilon_{n'} \propto (n^2 - n'^2)$ ; the most important contribution in the coefficients  $b_n^{(j)}$  is for  $n' - n = 0 \pmod{2M}$ , as one can infer from the numerical solution of Eq. (3.5) as well as from a perturbative approach [LŠBG12] at weak lattice strength, thereby yielding the observed recurrence time  $T_R$ .

A special point is the center of the box. The system will be in the same state as the initial one, once the unpinned excitations traveled to both borders of the box and back again. As the box is perfectly symmetric around its center, the central density is restored at a rate that is half the revival time of all other points.

## 3.3 The non-equilibrium steady state

For a value of  $M$  sufficiently large to be outside the mesoscopic regime of a few particles ( $M \geq 11$  in our case) and for sufficiently long times (ie at about half revival time) we observe in Fig. 3.1 that the system tends to a (quasi) steady state – as we shall denote this state for a finite-size system.<sup>1</sup> This state tends to a truly steady state once the thermodynamic limit is taken (see Section 3.4

<sup>1</sup>According to our numerical solution, the density profile is very close to the steady-state prediction (3.9) except for travelling wiggles due to reflections against the walls.

below for details). The (quasi) steady state can be well described by neglecting the oscillating terms in Eq. (3.8)

$$n(x, t) \rightarrow n^{SS}(x) = \frac{2}{L} \sum_{n=1}^{\infty} f_n \sin^2(n\pi x/L) \quad (3.9)$$

with nonthermal occupation numbers  $f_n$  given by  $f_n = \sum_{j=1}^N |b_n^{(j)}|^2$ . The above result (3.9) is illustrated as horizontal dashed lines in Fig.3.1. In the absence of the lattice  $f_n$  is given by a Fermi distribution at zero temperature. At increasing height of the initial lattice the (quasi) steady state is characterized by the occupation of more and more excited bands, as shown in Fig. 3.2. We notice that the occupation numbers  $f_n$  vanishes for  $n = M + 1$  to  $2M$ , and similarly for higher excited levels corresponding to even bands. This is due to the fact that the optical lattice acts as a backscattering potential creating excitations with wavevector  $2k_L$ , which corresponds to  $2k_F = 2M\pi/L$  in our choice of lattice filling. In energy space, this allows to excite only levels with quantum number difference  $\Delta n = 2M$ . Mathematically, the result follows from the linear algebra problem in equation (5): the optical lattice gives rise to off-diagonal terms into the matrix that are a distance  $2M$  from the diagonal. The corresponding eigenvectors have mostly zero components except  $b_n^{(j)} \neq 0, \forall n = 2M + 1$ . Combining this property with the definition of the occupation numbers  $f_n$  we obtain the result shown in Fig.2.

Furthermore, our exact solution allows also to explore the approach to steady state. By an extensive analysis of various systems sizes, we have found a power-law approach to the steady state ie,  $n(x, t) - n^{SS}(x) \sim 1/t$  as times approaches  $T_R/2$ , which corresponds to the large-time limit in our finite-size system. This is illustrated in Fig.3.3 for various values of particle number  $M$ .

### 3.4 First-order coherence and momentum distribution

In order to further characterize the properties of the (quasi) steady state we study the time-dependent one-body density matrix

$$\rho_1(x, y, t) = M \int dx_2 \dots dx_N \Psi_B^*(x, x_2, \dots, x_M, t) \Psi_B(y, x_2, \dots, x_M, t).$$

This allows to determine the coherence properties of this state and in particular the presence of quasi-off-diagonal long-range order (QODLRO). Furthermore, this allows to obtain the momentum distribution of the gas  $n(k, t) = \int dx \int dy \rho_1(x, y, t) e^{ik(x-y)}$ , which is experimentally accessible with a high pre-

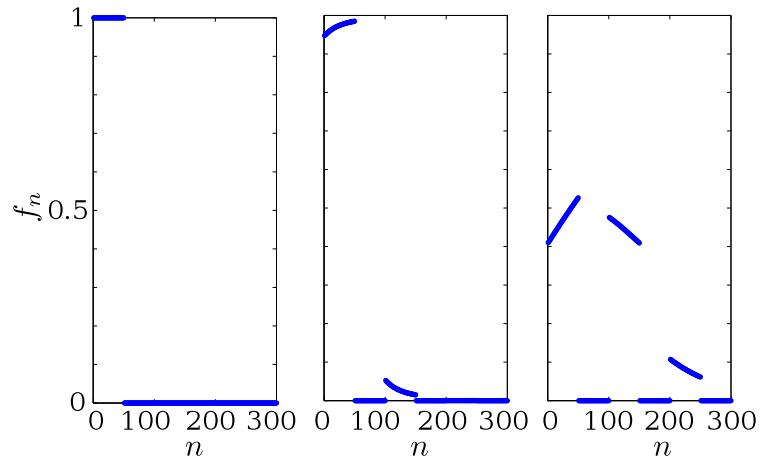


**Figure 3.2** – Occupation numbers  $f_n$  as a function of the quantum number  $n$  for  $M = 50$  particles, for various values of the dimensionless lattice strength, from left to right,  $\lambda = 0, 4, 50$ .

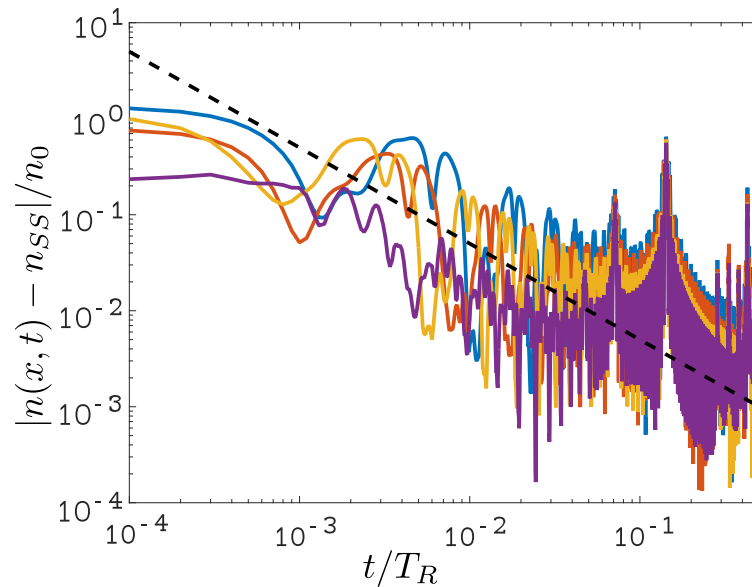


**Figure 3.3** – Approach to nonequilibrium steady-state: time evolution (time in units of  $T_R$ ) in double logarithmic scale for the difference between the particle density and its corresponding steady-state value  $|n(x,t) - n^{SS}(x)|$  (in units of  $n_0 = M/L$ ), evaluated at  $x = L/7$  and for  $\lambda = 40$ , for 81 (blue), 111 (red), 151 (orange) and 201 particles (purple). The particle density has been time averaged over a short time interval  $\Delta t = 0.001 T_R$  in order to decrease the noise in the figure. The dashed line indicates the  $1/t$  power law decay.

cision (see eg [JFB<sup>+</sup>12]).

Following the approach of Ref. [PB07] the one-body density matrix of a time-evolving Tonks-Girardeau gas is given by

$$\rho_1(x, y, t) = \sum_{j,l=1}^M \psi_j^*(x, t) A_{jl}(x, y, t) \psi_l(y, t). \quad (3.10)$$

where the matrix

$$A(x, y, t) = (P^{-1})^T \det P,$$

$P(x, y, t) = \mathbb{1} - Q$ , with

$$Q_{jl}(x, y) = 2 \operatorname{sign}(y - x) \int_x^y dx' \psi_j^*(x', t) \psi_l(x', t).$$

For our specific case, the matrix elements  $Q_{jl}(x, y)$  are readily evaluated analytically using Eq. (3.6).

The resulting density matrices are illustrated in Fig.3.4 for 15 bosons. As compared with the equilibrium case in absence of the lattice (panels a) and d)), the effect of the lattice at time  $t = 0$  is a pinning along the diagonal  $x = y$  and a reduction of the off-diagonal coherences, as evident from the sections taken along the direction  $x = -y$  (panels e) and f)). As a main result, we find that the (quasi) steady state at time  $t = T_R/2$  displays no QODLRO, and the one-body density matrix decays exponentially<sup>2</sup>. This is especially striking since the system is evolving in a homogeneous box, ie it is depinned: While the corresponding equilibrium state in the box displays QODLRO, ie the well-known power-law decay with power exponent  $-1/2$ , as shown in panel d) of Fig. 3.4, quite remarkably, the non-equilibrium aspect of the gas influences dramatically its coherence properties. This feature is found quite generally in integrable models, and has been first predicted by conformal-field methods for the state of the system at long times following a quench across a quantum critical point [CC06].

For weak lattice strength, the exponential decay of the one-body density matrix for the (quasi) steady state can be analytically obtained: the main contribution to the weights  $b_n^j$  is given by the term  $\delta_{n,j}$ , yielding for the matrix

---

<sup>2</sup>This result was checked by studying the density matrices for systems up to 31 bosons and an initial lattice strength of  $\lambda = 10$ . We have also checked that a similar behaviour is found for times close but not equal to  $T_R/2$ . Because of the symmetry around the center of the box, at the revival time  $t = T_R/2$  the central density is restored and the quasi-steady state is not reached. This is also the reason why at the off-diagonal  $x = L/2 - 2$  of the one-body density matrix in Fig. 3.4 (c), the pattern of the optical lattice is visible.

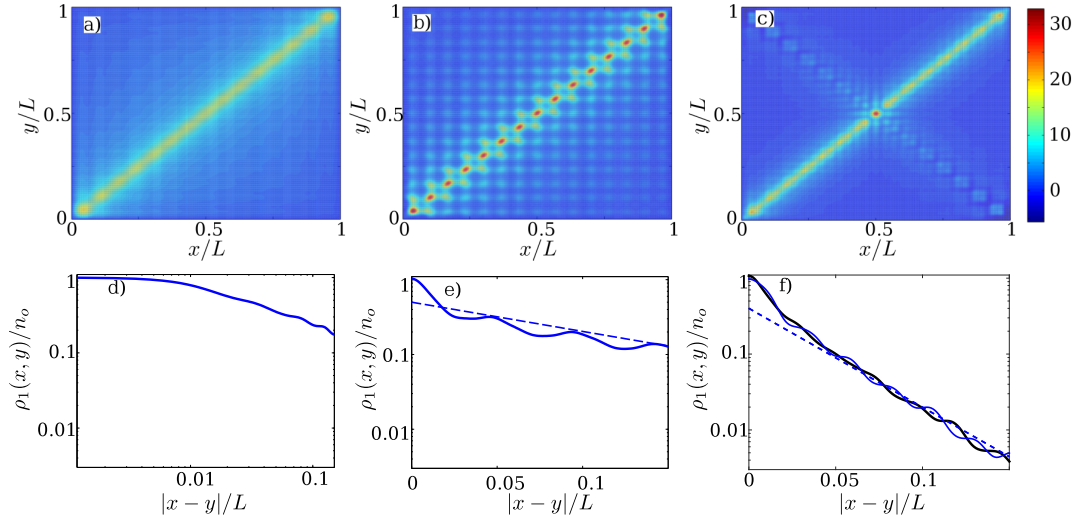


**Figure 3.4** – Real part of the one-body density matrix  $\rho_1(x, y)$  in units of  $n_0 = M/L$  as a function of the coordinates of the spatial coordinates  $x$  and  $y$  for  $M = 15$  bosons. Top panels: top view, bottom panels: corresponding cuts at fixed  $x + y = L/2$  as a function of the relative distance  $|x - y|$ . a) and d) equilibrium state in absence of the lattice. b) and e) equilibrium state in presence of the lattice, with lattice strength  $\lambda = 10$ . c) and f) depinned quasi steady state at time  $t = T_R/2$  (blue line) after a quench of the lattice to zero. The dashed line in panel e) is a guide to the eye and in panel f) indicates the exponential decay  $e^{-2n|x-y|}$  predicted in Eq.(3.11). The black line in f) shows the the depinned steady state at a time  $t = 0.45 T_R$ .

elements

$$P_{i,j} = \delta_{i,j} \left[ 1 - 2 \left| \frac{x-y}{L} - \frac{\sin(2\pi jx/L) - \sin(2\pi jy/L)}{2\pi j} \right| \right].$$

At large relative distances one may set

$$P_{i,j} \simeq \delta_{i,j} (1 - 2|x-y|/L),$$

and thereby obtaining

$$A = \mathbb{1} (1 - 2|x-y|/L)^{(N-1)}.$$

Taking the thermodynamic limit  $M \rightarrow \infty$  and  $L \rightarrow \infty$  at fixed  $n = M/L$  we find

$$A = \mathbb{1} \exp(-2n|x-y|)$$

and finally using (3.10) we obtain the bosonic quasi-steady state one-body density matrix

$$\rho_1(x, y, t \rightarrow \infty) = \rho_{1F}(x, y, t \rightarrow \infty) e^{-2n|x-y|}, \quad (3.11)$$

where  $\rho_{1F}(x, y, t) = \sum_{j=1}^M \psi_j^*(x, t) \psi_j(y, t)$  is the fermionic one-body density matrix. This result coincides with the one obtained in [CSC13] for the release of a harmonically trapped TG gas onto a ring: as expected, boundary conditions do not affect the result in the thermodynamic limit. Notice however the different way the steady state is reached: while in Ref. [CSC13] the long-time state is obtained by summing up all the periodically repeated images on the ring, in our case it is obtained by multiple reflections at the boundaries. Notice that our result can then be linked to the concept of Generalized Gibbs ensemble (GGE) for the thermodynamic limit of our model: as in [CSC13], the average of the fermionic occupation numbers  $\langle c_k^\dagger c_k \rangle$ , obtained from the initial fermionic one-body density matrix according to

$$\langle c_k^\dagger c_k \rangle = \frac{1}{2\pi} \int dx \int dy \rho_{1F}(x, y, 0) e^{ik(x-y)}$$

are conserved in the time evolution and can be used to determine the Lagrange multipliers  $\lambda_k$  defining the density matrix of the system at long times:  $\hat{\rho}_{GGE} \sim \exp(-\sum_k \lambda_k c_k^\dagger c_k)$ .

From the knowledge of the bosonic one-body density matrix  $\rho_1(x, y, t)$  we finally obtain the exact momentum distribution of the gas. We stress that our exact approach allows us to cover all the ranges of momenta, beyond the low-momentum region accessible by conformal-field methods. As shown in Fig.3.5, the momentum distribution of the (quasi) steady state is considerably different from the equilibrium ones both in absence and in presence of the lattice: it displays a considerably reduced intensity at low momenta, and does not show the typical backscattering peak at  $k = 2k_F$  found for the equilibrium gas in the presence of the lattice.

### 3.5 Conclusions and outlook

In conclusion, we have studied the exact time evolution of a Tonks-Girardeau gas following its sudden depinning off a weak optical lattice. We have identified a suitable long-time limit where a non-equilibrium steady state is reached in the thermodynamic limit, and we have shown a power-law approach to the steady state. Furthermore, we have shown that this state is characterized by the absence of quasi-long-range order ie an exponential decay of one-body correlations, in agreement with the predictions of the Generalized Gibbs Ensemble. Our numerical analysis for a system of finite size shows that this scenario could be reached with experimentally realistic numbers of bosons in a tight atomic waveguide, and that the time-dependent momentum distribution yields relevant information about this state. Our work opens to the study of the details of the quench depinning dynamics of a Lieb-Liniger gas at arbitrary interactions and

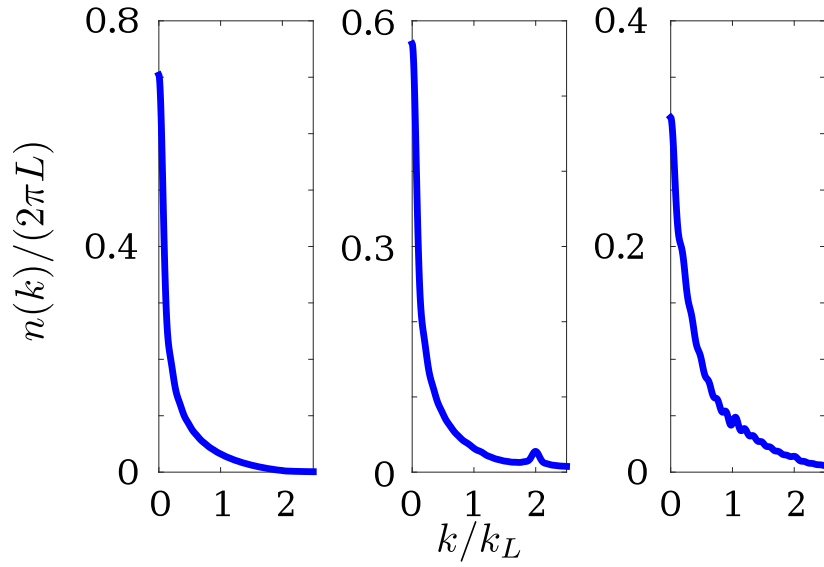


**Figure 3.5** – Momentum distribution  $n(k)$  as a function of wave vector  $k$  for  $M = 15$  particles. Left: equilibrium state in absence of the lattice, center: equilibrium state in presence of a lattice with  $\lambda = 10$ , right: quasi steady state at time  $t = T_R/2$  after a quench of the lattice to zero.

to further tests of the GGE hypothesis with hard walls boundary conditions (see eg [GA15]).

# PART II

## Interacting dipoles



# CHAPTER 4

---

## Atomic Dipolar gases

---

The previous part examined the commensurate-incommensurate transition of cold atoms in ultracold lattices where the transition can be observed by varying the height of the optical lattice compared to the contact interactions. In the following, we will consider particles with dipole-dipole interaction, which are generally anisotropic, are more long range than van-der-Waals interactions and will lead to new quantum phases. Before the new phases are discussed, this chapter will give an overview of the dipolar interactions in low dimensional lattices.

### 4.1 Dipole-Dipole interaction

The interaction energy of two particles with dipole moments  $\mathbf{p}_1$  and  $\mathbf{p}_2$  that are a distance  $\mathbf{r}$  apart is

$$U_{dd} = c \frac{\mathbf{p}_1 \mathbf{p}_2 - 3(\mathbf{p}_1 \hat{\mathbf{r}})(\mathbf{p}_2 \hat{\mathbf{r}})}{r^3}, \quad (4.1)$$

where  $\hat{\mathbf{r}} = \mathbf{r}/r$  and  $c$  is a constant that depends on the type of dipoles. The constant is

$$c = \frac{1}{4\pi\epsilon} \quad (4.2)$$

with the permittivity  $\epsilon$  in case of electric dipoles and

$$c = \frac{\mu_0}{4\pi} \quad (4.3)$$

with the permeability  $\mu_0$  in case of magnetic dipoles.

By applying a strong external magnetic or electric field, all the dipole moments arrange parallel to the external field,  $\mathbf{p}_1 = \mathbf{p}_2 = \mathbf{p}$ , and the resulting

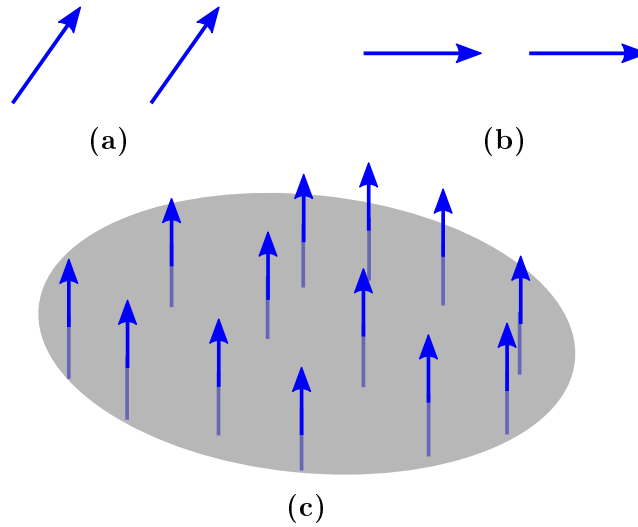


**Figure 4.1** – *Figure (a): two dipoles do not interact, if the angle between the dipole moment and the relative vector is  $\theta = \arccos(\sqrt{1/3})$ . In (b) the dipole moment is parallel to the vector that connects two dipoles, the interaction is attractive. In (c) the particles are confined in a two dimensional plane and the dipoles are polarized orthogonal to it. The dipolar interaction is then isotropic and repulsive within the plane.*

dipole-dipole interaction is

$$U_{dd} = C_D \frac{1 - 3(\hat{\mathbf{p}} \cdot \hat{\mathbf{r}})^2}{r^3}, \quad (4.4)$$

with  $C_D = c \cdot p^2$ . In the following, we will always assume that the dipoles are polarized by an external electric field and the interaction is given by (4.4).

This makes the interactions between dipoles fundamentally anisotropic, which has a big influence on the stability of the system. If the particles are confined in an highly anisotropic trap, where the confinement  $\omega_z$  along  $z$  is much larger than  $\omega_x, \omega_y$ , the particles will arrange in a pancake shaped configuration. If the dipoles are polarized in the  $x$ - $y$  plain, the interaction is mainly attractive and the gas is not stable, while, if the polarization is along  $z$ , the interaction between dipoles is mainly repulsive and the cloud will always be stable [KLM<sup>+</sup>08]. However, as we shall discuss later, the interaction also contains an attractive on-site contribution that changes the s-wave value of the contact interaction.

## 4.2 Interacting dipoles in low dimensions

In this work we always consider quasi one-dimensional systems, where in the thermodynamic limit, the system is translationally invariant along one axis, but not along the other two. In a physical system, this assumption is correct, as long as the confinement is highly anisotropic, and if the chemical potential and the temperature are smaller than the transverse trapping frequency  $\mu, k_B T < \hbar\omega_\perp$ . To find the correct one-dimensional theory, the other directions are integrated out assuming the system is in the lowest vibrational state of the transverse oscillators.

As was discussed in the first part of this thesis, particles in optical lattices with contact interactions are either in an insulating (Mott) phase, or an un-gapped (superfluid) phase. If the particles now interact via an additional dipole moment, it is generally not sufficient to only include s-wave scattering, as it is the case for dilute gases with van der Waals interactions. The dipole-dipole interaction is long-range in three dimensions, as it decays as  $V \sim r^{-3}$ . Also in a quasi one-dimensional system, the effect of the interaction has to be taken into account explicitly.<sup>1</sup> For example in the tight-binding limit, the Bose-Hubbard model must be extended in order to describe dipoles by including interactions between nearest neighbour sites. Extended Bose-Hubbard models have been the subject of increased interest in the last years [SDH<sup>+</sup>12, BSRG13], as the phase diagram can include supersolid, density wave and Haldane phases.

In a quasi-one dimensional system with tunable transverse trapping frequency  $\omega_\perp$ , there is another feature associated to dipolar interactions, namely a transverse instability. Let's consider that in a one dimensional optical lattice with commensurate filling ( $n \propto 1/a$ ) all the dipole moments are polarized such that the dipolar interaction is repulsive along the chain. In a classical system, the ground state needs to fulfill a balance between the confining potential and the interaction energy. If the interaction energy becomes of the same order as the confining potential,  $C_D/a^3 \approx \frac{1}{2}m\omega_\perp^2 a^2$ , then the quasi one-dimensional approximation can break down and the single chain will split into two chains.

In the next sections, we study the how the classical and the quantum effects of dipolar interactions come together to determine the full phase diagram. First, we will study the classical effect of the interactions, where we determine

---

<sup>1</sup>Interactions are defined to be long-range, if the interactions decay as  $1/r^\alpha$  [LPR<sup>+</sup>14], in  $d$  dimensions if  $\alpha \leq d$ . Systems with long-range interactions are not extensive or additive, which makes it hard to define thermodynamic limits. If a system of  $N$  particles in volume  $V$  interacts via a short range interaction within the range  $\gamma$ , then a particle will interact with  $N\gamma^2/V$  particles. The internal energy can be written as  $U(N, V) = Nu(N/V)$ , where  $u(n)$  depends on the microscopic properties of the system. This is also true for interactions that do not have a cutoff  $\gamma$ , but decay rapidly enough, i.e.  $\alpha > d$ . Therefore dipolar systems are short-range in one dimension and long-range in three [FR66].

the nature of the linear instability. After this, we turn to the study of the corresponding quantum problem in optical lattices.

# CHAPTER 5

---

## The classical limit

---

This chapter is based on:

- FLORIAN CARTARIUS, GIOVANNA MORIGI, AND ANNA MINGUZZI, Structural transitions of nearly second order in classical dipolar gases, *Phys. Rev. A* **90**, 053601 (2014).

Classical dipoles in one dimension can arrange in linear strings. By relaxing the transverse confinement, this linear configuration splits into a zigzag. In this chapter we study the classical structural transition before studying the quantum phase diagram in the next chapter. A low energy theory is introduced that describes the system close to the transition and provides a means to characterize the nature of the transition.

### 5.1 Microscopic model

In this section we consider  $N$  classical particles of mass  $m$  confined by an anisotropic trap on the  $x-y$  plane, assuming a very tight confinement along the  $z$  direction. If all the dipoles are polarized along the  $z$  direction, the interaction potential (4.4) simplifies and the particles interact via a power-law repulsive potential of the form

$$V_{\text{int}}(\mathbf{r}_1, \dots, \mathbf{r}_N) = \frac{C_D}{2} \sum_{j \neq l} \frac{1}{|\mathbf{r}_j - \mathbf{r}_l|^\alpha}, \quad (5.1)$$

where  $C_D = \frac{p^2}{4\pi\epsilon_0}$  is the interaction strength and  $\mathbf{r}_j = (x_j, y_j)$  is the position of particle  $j = 1, \dots, N$ . Here we introduced the generic power-law exponent  $\alpha$ . While for dipolar particles  $\alpha = 3$ , we will study also what configurations can be found for different power law interactions. For instance, this includes the case of for Van-der-Waals interactions where  $\alpha = 6$  or Coulomb interactions with

$\alpha = 1$ . The particles are confined by a ring-shaped harmonic trap,

$$V_{\text{trap}}(\mathbf{r}_1, \dots, \mathbf{r}_N) = \frac{1}{2} m \omega_t^2 \sum_{j=1}^N (r_j - R_0)^2, \quad (5.2)$$

with  $r_j = |\mathbf{r}_j|$  and  $\omega_t$  the frequency in the radial direction. Such trapping potential is currently realized for quantum gases [GMM<sup>+</sup>05, MCL<sup>+</sup>06, RAC<sup>+</sup>07, HNSF08, HRMB09, MBS<sup>+</sup>12]. For large radii it approaches a linear trap with periodic boundary conditions, which is studied in section 5.3.1 with a focus on configurations with more than two chains.

We will numerically seek in Sec.5.3 for the configuration which minimizes the energy in the total potential

$$V = V_{\text{int}} + V_{\text{trap}}, \quad (5.3)$$

close to the linear-zigzag instability. It is intuitive that for large trap frequencies  $\omega_t$  all the particles are pushed onto a perfectly ring shaped configuration, while for a weak trap strength, this single ring (linear) configuration cannot be stable. The regime of structural stability of the linear configuration is analytically identified by means of a Taylor expansion of the potential about the linear array. This has been performed in Refs. [AMDCB08, ACMB09]. In the next section we report the basic steps, here applied to the specific configuration of a ring trap. In section 5.3.1, we will study the configurations that are found for smaller trap frequencies with more than two chains in the limit of large trap radii.

## 5.2 Stability of the linear chain

Before studying the minimum energy configurations that are found in the system, this section will study the structural stability of the single ring configuration. This is done in a similar way in [AM76]. A single ring configuration is stable if the force is zero and the Hessian of the potential energy has only positive eigenvalues, i.e. all eigenfrequencies are real and positive. In order to analyse the stability properties of the ring chain, we first rewrite the interaction potential  $V_{\text{int}}$ , Eq. (5.1), in terms of polar coordinates, such that

$$V_{\text{int}} = (1/2) \sum_{j,l \neq j} U(r_j, \phi_j, r_l, \phi_l),$$

and

$$U(r_j, \phi_j, r_l, \phi_l) = \frac{C_D}{(r_j^2 + r_l^2 - 2r_j r_l \cos(\phi_j - \phi_l))^{\alpha/2}}.$$

We denote by  $R$  the ring radius, which results to be  $R > R_0$  due to the interparticle repulsion. Moreover, we denote by  $a$  the uniform interparticle distance along the ring, such that  $a = 2\pi R/N$ . Assuming that one dipole of the ring is pinned, the single ring is a regular structure which exhibits discrete translational invariance where the particles are located at radial position  $r_j = R$  and at angles  $\phi_j = 2\pi j/N$  ( $j = 0, \dots, N-1$ ). This configuration corresponds to equilibrium since the first derivatives of the total potential  $V$ , Eq. (5.3), vanish. In order to verify that the equilibrium is stable, we call  $\boldsymbol{\delta}_j$  the displacement out of the equilibrium position, and consider the second-order Taylor expansion

$$V_{\text{tot}} \approx V^{\text{eq}} + \frac{1}{2} \sum_{j,l} \boldsymbol{\delta}_j^T \mathbf{D}(j-l) \boldsymbol{\delta}_l, \quad (5.4)$$

where  $\mathbf{D}$  is called the dynamical matrix [AM76]. The equation of motion of the  $j$ -th particle is then

$$m\mathbf{a}_j = -\text{grad}_{\mathbf{r}_j} V_{\text{tot}}. \quad (5.5)$$

Because of the discrete periodicity, the equation of motion is diagonalized by the ansatz

$$\boldsymbol{\delta}_j = \boldsymbol{\epsilon} e^{i(qja - \omega t)}, \quad (5.6)$$

where  $q \in [-\frac{\pi}{a}, \frac{\pi}{a}]$  is the wave vector. Substituting (5.6) into the equation of motion (5.5) leads to the eigenvalue problem

$$m\omega^2 \begin{pmatrix} \epsilon_r \\ \epsilon_\phi \end{pmatrix} = \begin{pmatrix} D_{11} & D_{12} \\ D_{21} & D_{22} \end{pmatrix} \begin{pmatrix} \epsilon_r \\ \epsilon_\phi \end{pmatrix}, \quad (5.7)$$

where the components of the dynamical matrix are given by

$$D_{11} = m\omega_t^2 + \sum_{m=1}^{N-1} \left[ \frac{\partial^2 U(m)}{\partial r_j^2} + \frac{\partial^2 U(m)}{\partial r_j \partial r_l} e^{iqma} \right] \quad (5.8)$$

$$D_{12} = \frac{1}{R} \sum_{m=1}^{N-1} \left[ \frac{\partial^2 U(m)}{\partial r_j \partial \phi_j} + \frac{\partial^2 U(m)}{\partial r_j \partial \phi_l} e^{iqma} \right] \quad (5.9)$$

$$D_{21} = \frac{1}{R} \sum_{m=1}^{N-1} \left[ \frac{\partial^2 U(m)}{\partial r_j \partial \phi_j} + \frac{\partial^2 U(m)}{\partial r_l \partial \phi_j} e^{iqma} \right] \quad (5.10)$$

$$D_{22} = \frac{1}{R^2} \sum_{m=1}^{N-1} \left[ \frac{\partial^2 U(m)}{\partial \phi_j^2} + \frac{\partial^2 U(m)}{\partial \phi_j \partial \phi_l} e^{iqma} \right], \quad (5.11)$$

and we used the shorthand notation  $U(m) = U(R, 0, R, 2\pi m/N)$ .

Figure 5.1 shows the eigenmodes of the linear configuration. By decreasing the trap frequency  $\omega_t$  one of the eigenfrequencies at the edge of the Brillouin zone at  $q = \pi/a$  will become imaginary. Unlike in linear traps, the ring symmetry always leads to a coupling of angular and radial eigenmodes, at the edge of the Brillouin zone ( $q = \pi/a$ ), the modes are decoupled, as  $D_{12} = D_{21} = 0$ . This means that the critical trap frequency is given by  $\omega_t = \omega_t^{(c)}(N)$ , with

$$\left(\omega_t^{(c)}(N)\right)^2 = -\frac{C_D}{m} \sum_{m=1}^{N-1} \left[ \frac{\partial^2 U(m)}{\partial r_j^2} + \frac{\partial^2 U(m)}{\partial r_j \partial r_l} e^{i\pi m} \right]. \quad (5.12)$$

For  $R, N \rightarrow \infty$ , but keeping  $a = 2\pi R/N$  constant, we can define a thermodynamic limit. In this limit the critical trap frequency approaches

$$\lim_{N \rightarrow \infty} \omega_t^{(c)}(N) = \sqrt{\alpha(4 - 2^{-\alpha})\zeta(\alpha + 2) \frac{C_D}{m a^{\alpha+2}}},$$

and  $\zeta(x)$  the Riemann's zeta function. For the Coulomb interaction this instability is a second-order phase transition which is classically described by the Landau model [FDCCM08]. The mode at  $|q| = \pi/a$  is then the soft mode driving the instability, and the order parameter the displacement  $r_j - R$  in the radial direction. In Refs. [AMDCB08, SMF11, PHP10, RDTHA12] it has been conjectured that this may hold for any power-law repulsive interaction with  $\alpha \geq 1$ .

### 5.3 Minimum configurations

We proceed now in determining the minimum energy configurations of the total potential energy  $V = V_{\text{trap}} + V_{\text{int}}$  for different values of the trap frequency  $\omega_t$  using the Basin-Hopping Monte-Carlo method [WD97], with which we identify the equilibrium configurations corresponding to the global minimum of the potential energy for  $N$  ranging from 16 to 1100. We note that the configurations we find are expected to reproduce the correct ground state at  $T = 0$  when the interaction energy exceeds the kinetic energy, hence at sufficiently high densities and for large permanent dipoles [AMDCB08, CODPC07, SDCC<sup>+</sup>13, SCMM14].

As a result of the minimization procedure, for sufficiently large frequencies  $\omega_t$  (or, alternatively, small linear densities  $1/a$ ), we find a single array, or linear configuration, as in Fig. 5.2(a). Its equilibrium radius  $R$  is larger than the confining radius  $R_0$  due to the repulsive interactions. For  $\omega_t < \omega_t^{(c)}$  and a sufficiently large number of particles the minimal energy configurations determined numerically are inhomogeneous. In particular, they result to be a mixture of single-

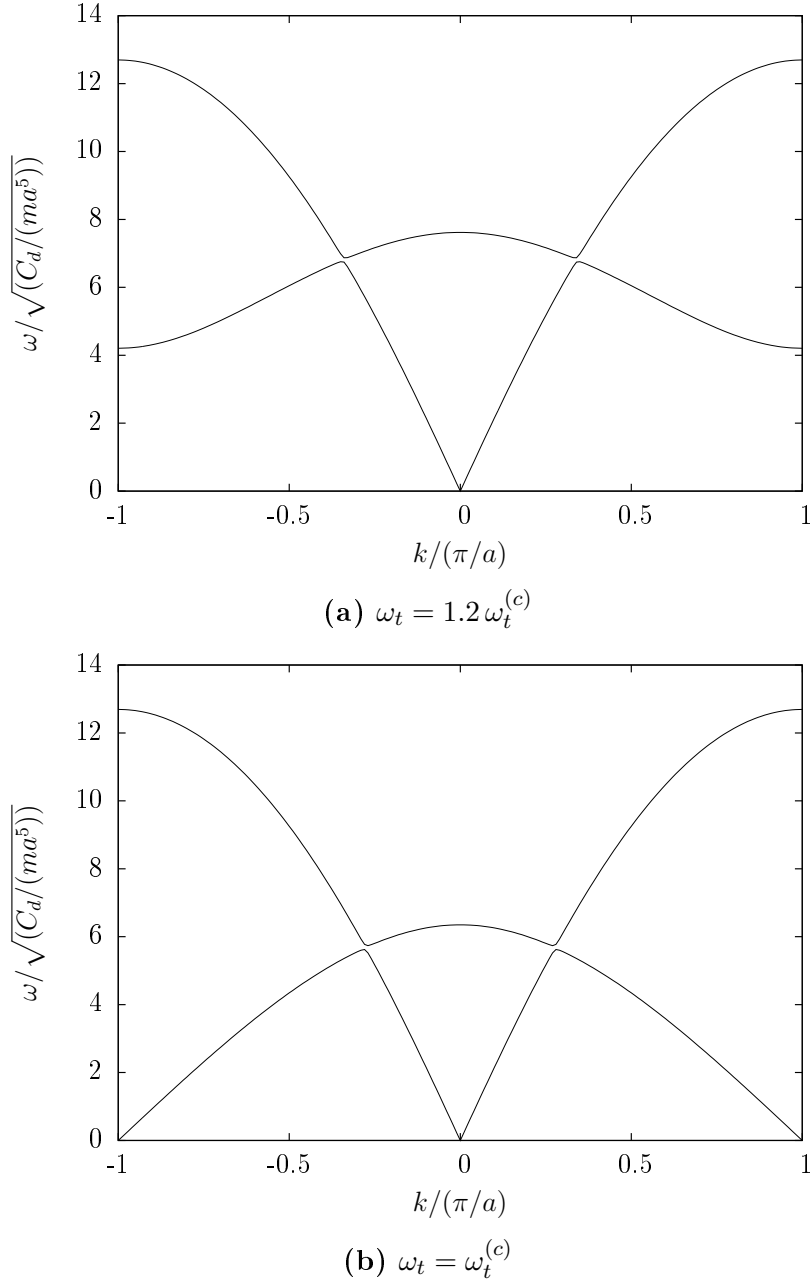


**Figure 5.1** – The vibrational spectrum of a linear ring configuration above (a) and at (b) the critical trap frequency. Because the radial and angular modes couple, there is a band gap between the two excitation branches.

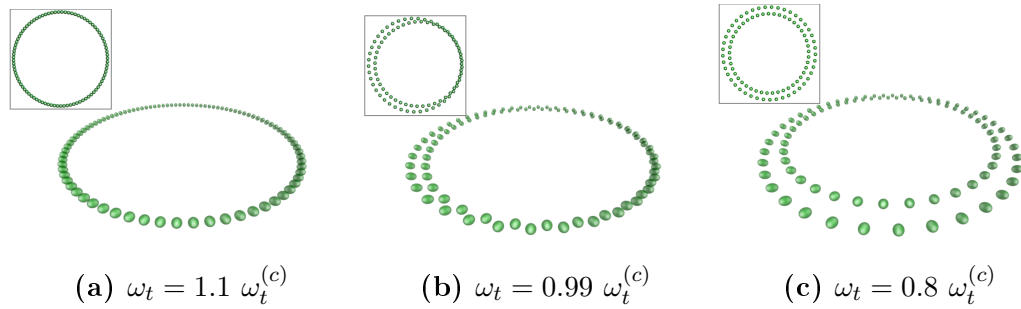


**Figure 5.2** – Side view (main panels) and top view (insets) of the various configurations found in the Monte-Carlo simulations: single ring (linear chain) (a), inhomogeneous configuration (b), and double ring (zigzag chain) (c) of classical dipolar particles confined in the plane perpendicular to the polarizing electric field. The different configurations correspond to three decreasing values of the radial confinement in the ring trap. The inhomogeneous configurations as in (b) indicate a coexistence of linear and zigzag structures, and are numerically found using periodic boundary conditions. Similar structures are found as well in a box with hard walls by varying the transverse frequency or the linear density.

and two-ring structures, as shown in Fig. 5.2(b). The inhomogeneous configurations appear when the number of dipoles exceeds a certain value  $N_0 > 32$ , and they are thus absent for  $N = 16$ , which was the case reported in Ref. [AMDCB08, ACMB09]. For this parameter range the homogeneous double ring (zigzag configuration) is metastable, separated by a small energy barrier from the linear chain. Both structures are at higher energy than the inhomogeneous one, which exhibits domains of linear and zigzag configurations. By further decreasing  $\omega_t$  the global minimum is the zigzag configuration, whose equilibrium positions are given by  $r_j = R + (-1)^j b$  and  $\phi_j = 2\pi j/N$ , where  $b > 0$  is half the radial distance between the two rings. The zigzag configuration is illustrated in Fig. 5.2(c). The zigzag configuration is found provided the number of particles is even, while for odd  $N$  the structure exhibits topological defects [CCM13]. By further decreasing the trap frequency, the two chain configuration will eventually split into more chains, as can be seen in Sec. 5.3.1.

A good indicator of the presence of the inhomogeneous configuration is the average displacement  $b$  of the linear configuration. Figure 5.3 (a) shows the displacement as a function of the trapping frequency as obtained by the numerical minimization. The region of inhomogeneous configurations is clearly visible as a deviation from the expected square-root behaviour predicted by the Landau theory for a second-order phase transition [FDCCM08, AMDCB08]. A zoom on the transition region also illustrates how the actual transition occurs quite suddenly (within the numerical accuracy) and at a frequency which is slightly larger than the frequency  $\omega_t^{(c)}$ . The frequency  $\omega_t$  below which inhomogeneous

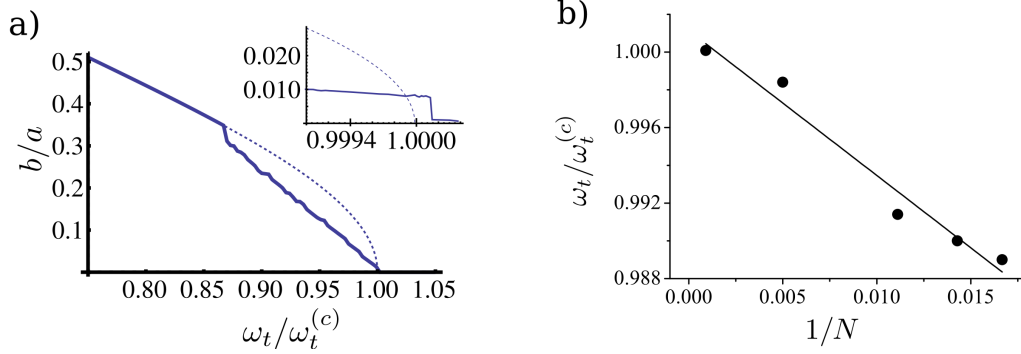


**Figure 5.3** – (a) Average transverse displacement  $b$  (solid line) along the ring (in units of the interparticle distance along the ring) as a function of  $\omega_t/\omega_t^{(c)}$  for  $N=500$  dipoles. The dashed line indicates the average displacement of a continuous transition, that is obtained by only allowing transverse particle movement. The inset shows the displacement  $b$  close to the transition region for 1100 dipoles. (b) Trap frequency below which inhomogeneous configurations are the minimal energy solutions in the numerical simulations as a function of  $1/N$ , where  $N$  is the number of particles along the ring. The red line is a linear fit  $\omega_t/\omega_t^{(c)} = a + b/N$  with parameters  $a = 1.0011 \pm 0.0009$  and  $b = -0.77 \pm 0.08$ .

configurations are found tends asymptotically to the value  $\omega_t = 1.0011(9)\omega_t^{(c)}$ . Finite-size corrections scale linearly with  $1/N$ , as illustrated in Fig.5.3 (b).

But are these inhomogeneous configurations a special case of the dipole interactions? To answer this, one can look for the minimum energy configurations for ions, with power-law interaction coefficient  $\alpha = 1$ , and particles that interact via van der Waals' interaction with  $\alpha = 6$ . For the long-range Coulomb interaction no inhomogeneous ground-state solutions can be found, in agreement with the results of Ref. [FDCCM08]. In the Coulomb case, indeed, the inhomogeneous configurations are excitations [LRB<sup>+</sup>13], and the linear-zigzag transition is continuous [FDCCM08]. On the other hand for the short-range van der Waals' interaction, inhomogeneous solutions are present and in general, our numerical results clearly indicate that the structural transition for dipolar gases (and in general for  $\alpha > 2$ ) deviates from the behaviour predicted from the Landau theory for second-order phase transitions.

### 5.3.1 The limit of the linear trap

In the previous section it was shown that chains of particles with short-range power-law interaction display inhomogeneous configurations in a ring trap. At this point it is not clear, whether the configurations are a special case of the ring trap, or the boundary conditions. For this reason, in this section a linear trap geometry is chosen to see whether these configurations also appear in other

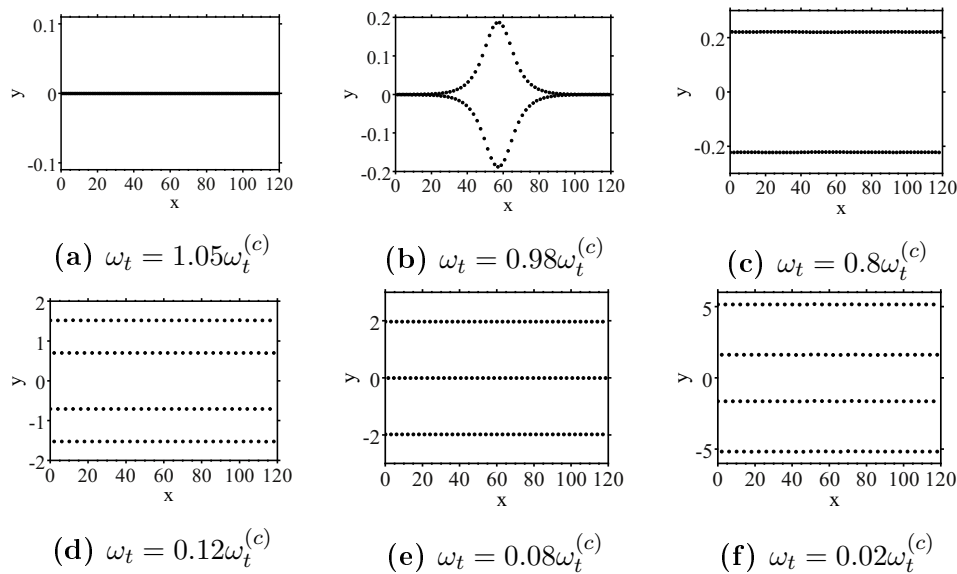


**Figure 5.4** – The minimum energy configuration of 120 dipoles found by the Monte-Carlo minimization for different trap frequencies in a linear trap with periodic boundary condition along  $x$ . The  $x$  and  $y$  coordinates are given in units of the linear density  $a$ .

traps. As we are interested in the limit of large system sizes, we consider no confinement along  $x$  and take either periodic or open boundaries along  $x$ . The confinement along  $y$  is given by an harmonic trap,

$$V_{\text{lin}}(\mathbf{r}_1, \dots, \mathbf{r}_N) = \frac{1}{2} m \omega_t^2 \sum_{j=1}^N y_j^2. \quad (5.13)$$

The trapping potential (5.13) with periodic boundary condition along  $x$  is the limit of (5.2) for large  $R_0$ .

Figure 5.4 shows typical minimum energy configurations found in the system. Similarly to the case of the ring trap, the particles arrange in a single chain for sufficiently high trap frequencies  $\omega_t^t$ . Around  $\omega_t = \omega_t^{(c)}$  inhomogeneous configurations the inhomogeneous configurations that were found previously are found once more, which will turn into regular zigzag structures for lower trap frequencies. The inhomogeneous configurations are therefore not a peculiarity of the ring trap. We also find them using open boundary conditions.

By further decreasing the radial confinement, the minimum energy configuration will eventually consist of more than two chains. With decreasing trap frequency, the minimum energy configuration consists of 1 chain, 2 chains, 4 chains, 3 chains, 4 chains, more chains. This order is the same for ions [PHP10].

To check if the transition to multiple chains is continuous or of first order,

we calculate the energy of the two, three and 4 chain configuration. Assuming translational symmetry along  $x$ , the energy of up to four chains is given by

$$\begin{aligned}
E_1/N &= \frac{C_D}{a^3} \sum_{j \neq 0} \frac{1}{j^3}, \\
E_2/N &= \frac{1}{2} m \omega_y^2 b^2 + \frac{1}{16} \frac{C_D}{a^3} \sum_{j \neq 0} \frac{1}{|j|^3} + \frac{C_D}{2a^3} \sum_{j \neq 0} \frac{1}{((2j+1)^2 + (b/a)^2)^{3/2}}, \\
E_3/N &= \frac{1}{3} m \omega_y^2 b^2 + \frac{1}{18} \cdot \frac{C_D}{a^3} \sum_{j \neq 0} |j|^{-3} + \frac{C_D}{a^3} \sum_j \frac{1}{(9(j+\frac{1}{2})^2 + (b/a)^2)^{3/2}} \\
&\quad + \frac{1}{2} \frac{C_D}{a^3} \sum_j \frac{1}{(9j^2 + 4(b/a)^2)^{3/2}}, \\
E_4/N &= \frac{1}{4} m \omega_y^2 (b^2 + c^2) + \frac{1}{32} \frac{C_D}{a^3} \sum_{j \neq 0} \frac{1}{|j|^3} \\
&\quad + \frac{C_D}{2} \sum_j \frac{1}{16(j^2 a^2 + 4c^2)^{3/2}} + C_D \sum_j \frac{1}{(16(j+\frac{1}{2})^2 a^2 + (c-b)^2)^{3/2}} \\
&\quad + C_D \sum_j \frac{1}{(16(j+\frac{1}{2})^2 + (c+b)^2)^{3/2}} + \frac{C_D}{2} \sum_j \frac{1}{(16j^2 a^2 + 4b^2)^{3/2}},
\end{aligned}$$

where  $E_n$  is the ground state energy of  $n$  chains and  $b$  and  $c$  are the distance of the particles along  $y$ .

By minimizing the energy with respect to the parameters,  $b$  and  $c$ , we obtain the minimum energy of the respective configurations. Fig. 5.5 shows the derivative of the energy of the minimum energy. A discontinuity of the derivative indicates a first-order transition. As for ions [PHP10], the transition between 2, 4, and 3 chains are all of first order.

## 5.4 Low energy description of the transition

In this section, we will derive a low-energy model that describes the linear to zigzag transition. To accomplish this, we perform a systematic expansion of the interaction energy about the configuration in which the ions form a single ring. To facilitate the expansion we use the center-of-mass and relative coordinates  $R_{jl} = (r_j + r_l)/2$ ,  $\rho_{jl} = r_j - r_l$  and  $\phi_{jl} = \phi_j - \phi_l$ , and cast  $U(r_j, \phi_j, r_l, \phi_l)$  into the form

$$U(R_{jl}, \rho_{jl}, \phi_{jl}) = \frac{C_D}{[\rho_{jl}^2 \cos^2(\phi_{jl}/2) + 4R_{jl}^2 \sin^2(\phi_{jl}/2)]^{\frac{\alpha}{2}}}. \quad (5.14)$$

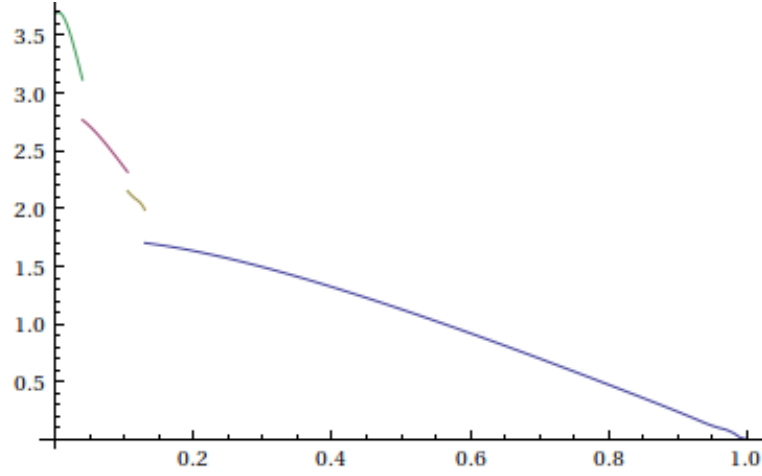


**Figure 5.5** – The derivative of the minimum energy  $\frac{dE}{d\omega_\tau}$  configuration versus the trap frequency. The blue curve indicates the 2 chain configuration, the yellow and green the 4 chain, and the red one the 3 chain configuration.

We then perform a systematic expansion of the interaction energy about the configuration in which the ions form a single ring, with the equilibrium positions  $r_j = R$ ,  $\phi_j = 2\pi j/N$ , see section 5.2. Setting  $r_j = R + a\Psi_j$  and  $\phi_j = 2\pi j/N + a\Theta_j/R$ , the expansion reads

$$V_{\text{int}} = \frac{1}{2} \sum_{j=1}^N \sum_{l \neq j}^N \sum_{0 \leq n_1 + n_2 + n_3 \leq 6} \frac{1}{n_1! n_2! n_3!} \frac{a^{n_1 + n_2 + n_3} \partial^{n_1} U \left( R, 0, \phi_j^{(0)} - \phi_l^{(0)} \right)}{2^{n_1} R^{n_3} \partial R^{n_1} \partial \rho^{n_2} \partial \phi^{n_3}} \times (\Psi_j + \Psi_l)^{n_1} (\Psi_j - \Psi_l)^{n_2} (\Theta_j - \Theta_l)^{n_3}, \quad (5.15)$$

where  $n_1, n_2, n_3$  are positive integers. In these derivatives all even-order derivatives in  $\rho$  vanish because of the symmetry of the single-ring configuration.

Next we write the deviations from the equilibrium positions in the eigenmodes of the single ring configuration,

$$\Psi_j = \frac{1}{\sqrt{N}} \sum_k \tilde{\Psi}_k e^{i(2\pi k j/N)}, \quad (5.16)$$

$$\Theta_j = \frac{1}{\sqrt{N}} \sum_k \tilde{\Theta}_k e^{i(2\pi k j/N)}. \quad (5.17)$$

These eigenmodes are the ones discussed in section 5.2, written in dimensionless units. We substitute eq. (5.16) and eq. (5.17) into equation (5.15) to obtain the Fourier transform of the expanded potential. For instance, the second order

terms are

$$\begin{aligned}
V_k^{(2)} = a^2 \sum_{l \neq 0} & \left[ \left| \tilde{\Psi}_k \right|^2 \frac{1}{4} \frac{\partial^2 U(R, 0, 2\pi l/N)}{\partial R^2} \cos^2(kla/2) \right. \\
& + \left| \tilde{\Psi}_k \right|^2 \frac{\partial^2 U(R, 0, 2\pi l/N)}{\partial \rho^2} \sin^2(kla/2) \\
& + \left| \tilde{\Theta}_k \right|^2 \frac{1}{R^2} \frac{\partial^2 U(R, 0, 2\pi l/N)}{\partial \phi^2} \sin^2(kla/2) \\
& \left. + \tilde{\Theta}_k \tilde{\Psi}_{-k} \frac{1}{4R} \frac{\partial^2 U(R, 0, 2\pi l/N)}{\partial \phi \partial R} \sin(kla) \right]. \quad (5.18)
\end{aligned}$$

The eigenmodes at the point where the single ring becomes mechanically unstable are shown in figure 5.1. The low energy eigenmodes are short wavelength ones in radial direction ( $\Psi$ ) and long wavelength in the angular direction ( $\Theta$ ). To get a low energy description, the eigenmodes are expanded  $k/N = k_0/N + \delta k/(2\pi)$  up to second order about  $k_0 = N/2$  for the radial modes, and about  $k_0 = 0$  for the angular ones. Specifically, we set  $|\tilde{\Psi}_k|^2 \cos^2(\pi lk/N) \approx |\tilde{\Psi}_k|^2 (\cos^2(l\pi/2) - \frac{1}{4}(-1)^{\Delta_l} \Delta_l^2 \delta k^2)$ , where

$$\Delta_l = \begin{cases} l, & \text{if } l \leq N/2 \\ N-l, & \text{if } l > N/2 \end{cases} \quad (5.19)$$

accounts for the periodicity of the cosine, and similarly for the other terms in eq. (5.18), yielding

$$\begin{aligned}
V^{(2)} = \sum_k & \left[ \left| \tilde{\Psi}_k \right|^2 \sum_{l \neq 0} \frac{\partial^2 U(R, 0, 2\pi l/N)}{\partial R^2} \frac{1}{4} \left( \cos^2(l\pi/2) - \frac{1}{4}(-1)^{\Delta_l} \Delta_l^2 \delta k^2 \right) \right. \\
& + \left| \tilde{\Psi}_k \right|^2 \sum_{l \neq 0} \frac{\partial^2 U(R, 0, 2\pi l/N)}{\partial \rho^2} \left( \sin^2(l\pi/2) + \frac{1}{4}(-1)^{\Delta_l} \Delta_l^2 \delta k^2 \right) \\
& \left. + \left| \tilde{\Theta}_k \right|^2 \sum_{l \neq 0} \frac{1}{R^2} \frac{\partial^2 U(R, 0, 2\pi l/N)}{\partial \phi^2} \frac{1}{4} \Delta_l^2 \delta k^2 \right]. \quad (5.20)
\end{aligned}$$

Next, we go over to a continuum description, setting  $\Theta_j \rightarrow \Theta(x)$  and  $(-1)^j \Psi_j \rightarrow \Psi(x)$ , where the staggered field  $\Psi(x)$  is now the position-dependent order parameter for the zigzag chain. The continuous fields are related to the

discrete Fourier components through the inverse transform

$$\Psi_k = \frac{1}{\sqrt{N}} \int dx e^{i2\pi\delta k \cdot x} \Psi(x), \quad (5.21)$$

$$\Theta_k = \frac{1}{\sqrt{N}} \int dx e^{i2\pi\delta k \cdot x} \Theta(x), \quad (5.22)$$

where  $x$  is a dimensionless quantity that runs along the ring from dipole to dipole between 0 and  $N - 1$ . The sum over  $k$  can be replaced by integrals for a large number of particles, setting  $\sum_k = \int d(\delta k)$ . We do the above procedure for all terms in the Taylor expansion (5.15), yielding the final expression in the low-energy limit for the complete potential energy,  $V_0 = V^{\text{eq}} + V_0$ , where  $V^{\text{eq}}$  is the equilibrium energy of the single ring and

$$V_0 = \frac{C_D}{a^\alpha} \int dx \left[ h_1^2 (\partial_x \Theta)^2 + h_2^2 (\partial_x \Psi)^2 + \Delta \Psi^2 + e (\partial_x \Theta) \Psi^2 + f \Psi^4 \right. \\ \left. + r (\partial_x \Psi)^2 \Psi^2 + \ell (\partial_x \Theta)^2 \Psi^2 + t \Psi^6 + p (\partial_x \Theta)^3 + q \Psi^4 \partial_x \Theta \right], \quad (5.23)$$

where the expansion coefficients are given by

$$h_1^2 = \frac{1}{4} \sum_{l \neq 0} l^2 \frac{a^2}{R^2} \frac{\partial^2 \tilde{U}(l)}{\partial \phi^2} \quad (5.24)$$

$$h_2^2 = -\frac{1}{4} \sum_{l \neq 0} (-1)^l (la)^2 \left( \frac{\partial^2 \tilde{U}(l)}{\partial \rho^2} - \frac{1}{4} \frac{\partial^2 \tilde{U}(l)}{\partial R^2} \right) \quad (5.25)$$

$$\Delta = (\omega_t^2 - \omega_t^{(c)2}) \frac{ma^{\alpha+2}}{C_D} \quad (5.26)$$

$$e = \sum_{l \neq 0} l^2 \frac{a^3}{R} \left( \frac{1}{4} \cos^2 \left( \frac{l\pi}{2} \right) \frac{\partial^3 \tilde{U}(l)}{\partial R^2 \partial \phi} - \sin^2 \left( \frac{l\pi}{2} \right) \frac{\partial^3 \tilde{U}(l)}{\partial \rho^2 \partial \phi} \right) \quad (5.27)$$

$$f = \frac{1}{3} \sum_{l \neq 0} a^4 \left( \frac{\partial^4 \tilde{U}(l)}{\partial \rho^4} \sin^4 \left( \frac{l\pi}{2} \right) + \frac{1}{16} \frac{\partial^4 \tilde{U}(l)}{\partial R^4} \cos^4 \left( \frac{l\pi}{2} \right) \right) \quad (5.28)$$

$$\ell = \sum_{l \neq 0} l^2 \frac{a^4}{R^2} \left( \frac{1}{8} \cos^2 \left( \frac{l\pi}{2} \right) \frac{\partial^4 \tilde{U}(l)}{\partial R^2 \partial \phi^2} - \frac{1}{2} \sin^2 \left( \frac{l\pi}{2} \right) \frac{\partial^4 \tilde{U}(l)}{\partial \rho^2 \partial \phi^2} \right) \quad (5.29)$$

$$r = \sum_{l \neq 0} l^2 a^4 \left( \frac{1}{2} \sin^4 \left( \frac{l\pi}{2} \right) \frac{\partial^4 \tilde{U}(l)}{\partial \rho^4} - \frac{1}{32} \cos^4 \left( \frac{l\pi}{2} \right) \frac{\partial^4 \tilde{U}(l)}{\partial R^4} + \frac{1}{8} \frac{\partial^4 \tilde{U}(l)}{\partial R^2 \partial \rho^2} \right) \quad (5.30)$$

$$t = \sum_{l \neq 0} a^6 \left( -\frac{2}{45} \sin^6 \left( \frac{l\pi}{2} \right) \frac{\partial^6 \tilde{U}(l)}{\partial \rho^6} + \frac{1}{1440} \cos^6 \left( \frac{l\pi}{2} \right) \frac{\partial^6 \tilde{U}(l)}{\partial R^6} \right) \quad (5.31)$$

$$p = \frac{1}{12} \sum_{l \neq 0} l^3 \frac{a^3}{R^3} \frac{\partial^3 \tilde{U}(l)}{\partial \phi^3} \quad (5.32)$$

$$q = \sum_{l \neq 0} l \frac{a^5}{R} \left( -\frac{1}{3} \sin^4 \left( \frac{\pi l}{2} \right) \frac{\partial^5 \tilde{U}(l)}{\partial \rho^4 \partial \phi} - \frac{1}{48} \cos^4 \left( \frac{\pi l}{2} \right) \frac{\partial^5 \tilde{U}(l)}{\partial R^4 \partial \phi} \right), \quad (5.33)$$

and we introduced  $\tilde{U} = U/(C_D/(a^\alpha))$ . All the dimensionless parameters above, depend only on the interaction, except  $\Delta$  which contains the trap frequency. If  $\Delta > 0$  the single ring is mechanically stable, if  $\Delta < 0$  it is not.

### 5.4.1 First-order transition

In this section, we will now look for uniform solutions for the fields  $\Psi$  and  $\Theta' = \partial_x \Theta$  minimizing the long-wavelength potential energy (5.23) for different values of  $\Delta$ , and thus of  $\omega_t$ . This allows us to find an analytical solution, with which we can verify whether there exists a parameter regime where the linear and the zigzag configurations are both local minima of the potential energy. The solutions are extrema of the potential, satisfying  $\partial V_0/\partial \Theta' = 0$  and  $\partial V_0/\partial \Psi = 0$  with positive-definite Hessian matrix. We determine an effective potential for the transverse-displacement field  $\Psi$  by eliminating the solution for  $\Theta'$ , which in the small- $\Psi$  limit reads

$$\Theta' = -\frac{1}{2h_1^2} \Psi^2 \left[ e + \left( q - \frac{el}{h_1^2} + \frac{3e^2 p}{4h_1^4} \right) \Psi^2 \right]. \quad (5.34)$$

Note that there is a second solution for  $\Theta'$ , which is finite at small  $\Psi$ , and thus inconsistent with our initial assumptions. Substitution of Eq. (5.34) in the expression (5.23) leads to the effective potential density

$$V_{\text{eff}} \propto \Delta \Psi^2 + u_{\text{eff}} \Psi^4/4 + \lambda \Psi^6, \quad (5.35)$$

where  $u_{\text{eff}} = (4f - e^2/h_1^2)$  and  $\lambda = \left( \frac{le^2}{4h_1^4} - \frac{e^3 p}{8h_1^6} - \frac{eq}{2h_1^2} + t \right)$ . Using the explicit form of the coefficients for the case of dipolar interactions we obtain that  $u_{\text{eff}} < 0$  and  $\lambda > 0$ . The effective model thus describes a first-order phase transition at  $\Delta = 0$ . It is interesting to point out that the sign of the quartic term is negative due to the coupling with the axial vibrations. Figure 5.6 shows the energy of the local minima and the corresponding displacement field  $\Psi$  obtained from the low-energy effective model as a function of the control parameter  $\Delta$ .

This solution predicts a sudden jump into two stable local minima near the dynamical instability of the single ring, which is characteristic of a first-order transition. Note that this solution is restricted to uniform transverse fields. Numerically, we find that the inhomogeneous solution is at lower energy,

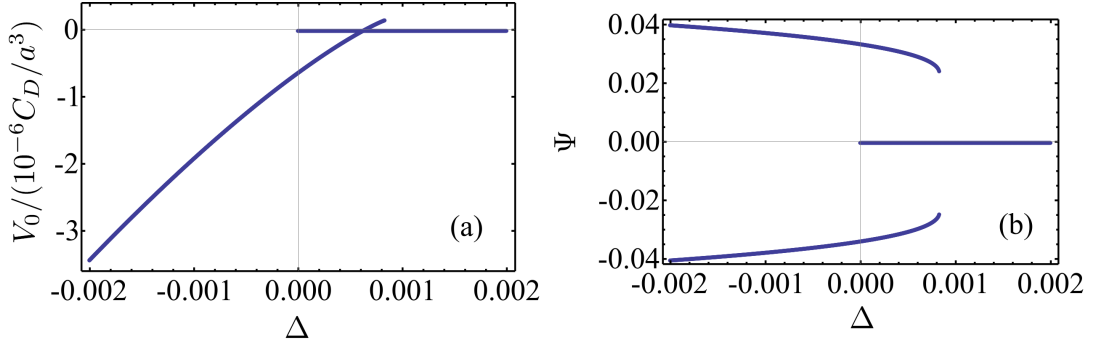


**Figure 5.6** – (a) Local minima of the energy in Eq. (5.23) for homogeneous solutions ( $\Psi' = 0$ ) and (b) corresponding transverse-displacement field (in units of distance  $a$  along the chain) as a function of  $\Delta$  (dimensionless) and in the thermodynamic limit. The region of coexistence of phases is in the interval  $\Delta \in [0, 0.0009]$ , corresponding to  $\omega_t^{(c)} \leq \omega_t \leq 1.000075 \omega_t^{(c)}$ .

corresponding to the coexistence of the zigzag and linear configurations. Quite remarkably, the parameter region of coexistence of phases is very narrow and close to the frequency  $\omega_t^{(c)}$ . Therefore, this transition is of 'weakly first-order' or of nearly second order [LP69, Imr74].

## 5.5 Finite-size system

We now address the predictions of the low-energy model for the displacement fields  $\Theta$  and  $\Psi$  in a ring of finite size. An analytical solution can be obtained if we keep just the leading order in the transverse-axial coupling, after setting  $r, \ell, t, p, q = 0$  in Eq. (5.23). This corresponds to a truncation of the effective potential to fourth order. This approach is clearly not capable to describe the nature of the phase in the thermodynamic limit, since it misses the sixth-order terms which stabilize the uniform solution. Nevertheless, in the finite-size ring, the solution is inhomogeneous, stabilized by the presence of the gradient terms in (5.23) and can be employed to account for the observed inhomogeneous configurations close to the transition point.

Using the variational principle we determine the equations for  $\Psi(x)$  and  $\Theta(x)$  which minimize Eq.(5.23),

$$\frac{d}{dx} (2h_1^2(\Theta') + e\Psi^2) = 0, \quad (5.36)$$

$$2h_2^2\Psi'' - 2\Delta\Psi - 2e\Theta'\Psi - 4f\Psi^3 = 0. \quad (5.37)$$

To find a solution to the Euler-Lagrange equations, we start by integrating

Eq. (5.36), obtaining

$$\Theta' = \frac{1}{2}B - \frac{1}{2}\frac{e}{h_1^2}\Psi^2, \quad (5.38)$$

where  $B$  is an integration constant. Substituting Eq. (5.38) into Eq. (5.37) gives

$$-2h_2^2\Psi'' + 2\Delta_{\text{eff}}\Psi + u_{\text{eff}}\Psi^3 = 0, \quad (5.39)$$

where  $\Delta_{\text{eff}} = \Delta + eB/2$  and  $u_{\text{eff}} = 4f - e^2/h_1^2$  are the renormalized constants entering the resulting effective potential-energy functional

$$V_{\text{eff}} = \frac{C_D}{a^\alpha} \int dx \left[ h_2^2(\Psi')^2 + \Delta_{\text{eff}}\Psi^2 + \frac{u_{\text{eff}}}{4}\Psi^4 \right].$$

Note that in the finite ring the boundary conditions effects yield a renormalization of the constant  $\Delta$ . This explains why the region of phase coexistence extends to negative values of  $\Delta$  for finite systems (see Fig. 5.3). Multiplying Eq. (5.39) by  $\Psi'$  and a subsequent integration leads to

$$(\Psi')^2 = \frac{1}{h_2^2}\Delta_{\text{eff}}\Psi^2 + \frac{1}{4h_2^2}u_{\text{eff}}\Psi^4 + \frac{1}{4}A, \quad (5.40)$$

where  $A$  is another integration constant. As this equation only depends on  $\Psi^2$ , we perform the substitution  $y = \Psi^2$  and obtain

$$(y')^2 = \frac{4}{h_2^2}\Delta_{\text{eff}}y^2 + \frac{1}{h_2^2}u_{\text{eff}}y^3 + Ay. \quad (5.41)$$

This equation can be solved by separating the variables [CLR00, KCU08]. We define the zeros of the right hand side of Eq.(5.41) as  $y_1 < y_2 < y_3$  and set  $g = -u_{\text{eff}}/4h_2^2$ . Eq. (5.41) can be integrated as

$$\int_0^x d\tilde{x} = \int_{y_3}^y \frac{d\tilde{y}}{\sqrt{-g(\tilde{y} - y_1)(\tilde{y} - y_2)(\tilde{y} - y_3)}}. \quad (5.42)$$

Finally we perform the substitution  $t^2 = \frac{\tilde{y} - y_2}{y_3 - y_2}$  and with

$$m = \frac{y_3 - y_2}{y_3 - y_1} = 1 - m', \quad (5.43)$$

we arrive at

$$\int_0^x d\tilde{x} = \frac{2}{\sqrt{g(y_3 - y_1)}} \int_1^Y \frac{dt}{\sqrt{(1 - t^2)(mt^2 + m')}}}, \quad (5.44)$$

where  $Y = \sqrt{(y - y_2)/(y_3 - y_2)}$ . This equation can be solved as

$$y(x) = \Psi^2(x) = y_3 \operatorname{cn}^2 \left( \frac{\sqrt{g(y_3 - y_1)}}{2} x | m \right), \quad (5.45)$$

where  $\operatorname{cn}(x|m)$  is a Jacobi elliptic function. The soliton discussed here is given by the case  $y_2 = 0$ . As our system is periodic, we will shift  $x$  by  $N/2$ , to center it between 0 and  $N$ . Substituting the eq. (5.45) into (5.38) gives then the solution for the angular displacements

$$\Theta'(x) = \frac{1}{2}B - \frac{1}{2} \frac{e}{h_1^2} \Psi^2(x). \quad (5.46)$$

The remaining constants  $y_1$  and  $y_3$  depend on the constants in the potential energy density in Eq. (5.23) and the integration constants  $A$  and  $B$ , which are determined by the boundary conditions,

$$y(0) = y(N), \quad (5.47)$$

$$\Theta(0) = \Theta(N). \quad (5.48)$$

Combining both boundary conditions, we find

$$\frac{2K(m)}{N} = \frac{\sqrt{g(y_3 - y_1)}}{2}, \quad (5.49)$$

$$B = 16 \frac{e}{gh_1^2} \frac{1}{N^2} K(m) (E(m) + (m - 1)K(m)), \quad (5.50)$$

where  $K(m)$  and  $E(m)$  are the complete elliptic integrals of the first and second kind, respectively and by solving eqs. (5.49) and (5.50), the two integration constants can be determined. By substituting eq. (5.45) into the long wavelength potential energy we finally determine the energy of the soliton solution.

Figure 5.7 displays the behaviour predicted by Eqs. (5.45-5.46) along the chain and the corresponding numerical results, showing a very good agreement within the model's regime of validity. The energy of the inhomogeneous configurations is obtained by substituting the corresponding solutions into the potential-energy density. It is found to be smaller than the energy of the zigzag case, in full agreement with the numerical observations. Inspection of Fig. 5.3 shows that in the numerical calculations for a finite ring the parameter region of phase coexistence is larger than in the thermodynamic limit, extending to negative values of  $\Delta$ . This can be explained noticing that boundary effects yield a renormalized control parameter  $\Delta_{\text{eff}}$  for the transition.

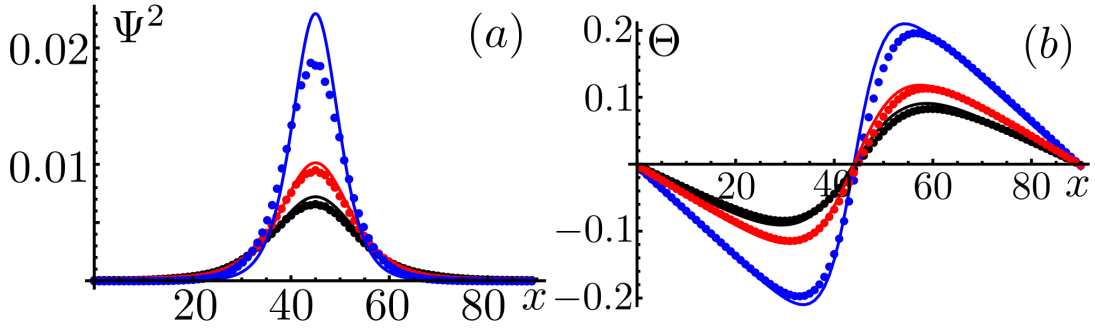


**Figure 5.7** – (a) Transverse squared displacement  $\Psi^2(x)$  and (b) axial displacement  $\Theta(x)$  (in units of distance  $a$  along the chain) as a function of distance  $x$  along the chain (in units of  $a$ ) for the minimal energy configurations on a ring with  $N = 90$  particles. Numerical Monte-Carlo data (circles) are compared to the solutions of Eqs. (5.45)-(5.46) (solid lines). From top to bottom, the blue, red and black curves correspond to trap frequencies  $\omega_t = 0.9915\omega_t^{(c)}$ ,  $0.99\omega_t^{(c)}$ ,  $0.985\omega_t^{(c)}$ , respectively.

### 5.5.1 Influence of thermal fluctuations

Our predictions are strictly valid when the effect of fluctuations is negligible. To study the effect of thermal fluctuations on the various configurations found at zero temperature, we have performed a finite temperature Monte-Carlo calculation, and determined the pair correlation function  $g_2(r, \phi) = \langle \sum_{i,j \neq i} \delta(r - (r_i - r_j)) \delta(\phi - (\phi_i - \phi_j)) \rangle$  for temperatures which are lower than the difference between the inhomogeneous and zigzag energies. Figure 5.8 displays the two-particle correlation functions for different values of  $\Delta < 0$ . The inhomogeneous configurations are clearly visible as the correlation is smeared along the radial direction in a semicircular shape, indicating varying radial displacements (thus, inhomogeneous  $\Psi(x)$ ). This result for the pair-correlation function is considerably different from both the one for the linear configuration, characterized by a periodic structure only along the tangential (axial) direction, and the one for a uniform two-ring configuration, where radially the only possible relative distances allowed are  $\pm\Psi$  and 0. The clear distinction between the various configurations is lost for temperatures higher than the energy barrier between the various configurations. Taking the value of the dipolar moment of LiCs molecules [DGR<sup>+</sup>08] and typical densities of the ongoing experiments [WPA<sup>+</sup>12], we estimate that the energy gap between the inhomogeneous and uniform configurations corresponds to a temperature of 0.2 nK. Although this value is still quite challenging from an experimental point of view, it can rapidly increase at increasing the density and the dipolar moment of the gases.

To estimate the parameter range for which the system is in a classical regime, we can compare the length scale associated with the quantum fluctuations  $a$ , with the length scale associated with the interactions  $r_0$ , which can be estimated

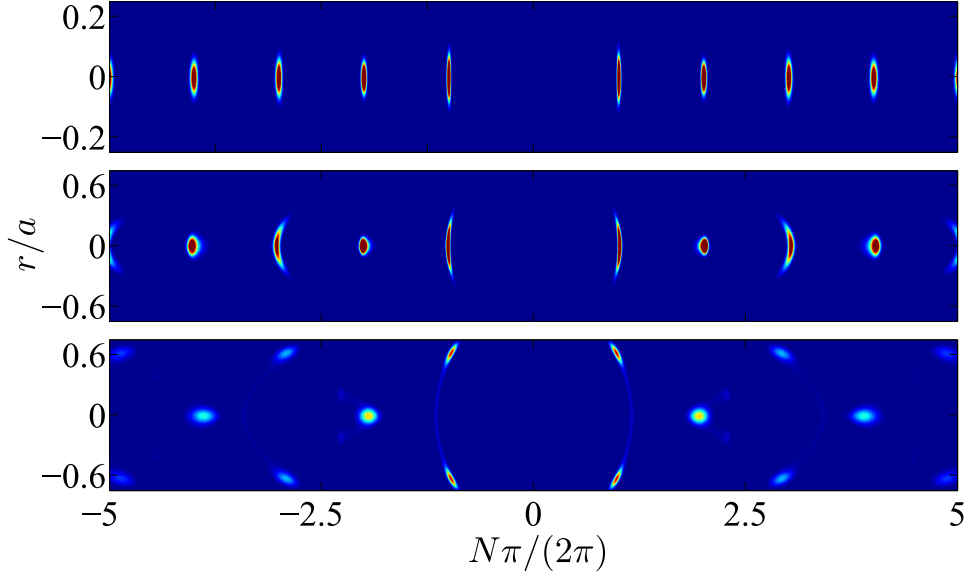


**Figure 5.8** – Two-particle correlator  $g_2(r, \phi)$  of 90 dipoles evaluated numerically and at  $T = 8 \times 10^{-4} C_D / (a^3 k_B)$ . The configurations correspond to a uniform single-ring (top,  $\omega_t = 1.05\omega_t^{(c)}$ ), an inhomogeneous structure (center,  $\omega_t = 0.98\omega_t^{(c)}$ ) and uniform two-ring configuration (bottom,  $\omega_t = 0.7\omega_t^{(c)}$ ).

to be  $r_0 = mC_D/\hbar^2$  [AMDCB08]. If  $a \ll r_0$ , the ground state energy of the system is well approximated by the classical ground state energy. In this regime, the quantum fluctuations have a similar effect as the temperature has in a classical system [ACMB09]. For LiCs molecules, the characteristic length is given by  $r_0 = 63 \mu\text{m}$ . Taking a Gaussian wave packet of the same size, the kinetic energy of a molecule can be estimated to be  $E \approx k_B \cdot 9 \mu\text{K}$ , which is larger than the energy gap of 0.2 nK. Thus, for the parameters of LiCs molecular gases, it is expected that quantum fluctuations will smear the transition.

In conclusion, we have shown that the linear-zigzag instability for power-law interactions  $\alpha > 2$  is a first-order phase transition, even though weak, whose hallmark is the appearance of inhomogeneous soliton-like structures which minimize the energy of finite systems. The instability is thus not described by a  $\phi^4$  model, since the coupling with the axial vibrations substantially modifies the properties of the transition. This is different from Coulomb systems, where the dispersion relation of the axial modes leads just to a renormalization of the coefficient of the  $\phi^4$  model in the critical region, without changing its nature [S<sup>+</sup>]. The dipolar system therefore realizes an example of Ising model coupled to axial phonons [LP69, Imr74]. Whether the weakly first-order nature of the transition survives the inclusion of quantum fluctuations is a question for future work. In the quantum regime, the instability is expected to exhibit the

---

existence of a critical point with enhanced symmetry and non-universal critical exponents, in analogy to the model discussed in Ref. [SRM<sup>+</sup>09]. While the study of the quantum problem on the continuum remains open, in the next chapter we present the study of the equivalent problem on a lattice.



## CHAPTER 6

---

### The quantum regime

---

In this chapter, we analyze the linear to zigzag transition of trapped polarized dipolar particles in the quantum regime. A similar setup as in chapter 5 is used, where the confinement of the dipoles is released along one direction, while keeping a tight axial confinement in the plain perpendicular to the dipole orientations. For the quantum case, in addition to the external harmonic confinement, we consider the case where an optical lattice is superimposed along the chain. In the tight-binding limit, we obtain a multi-mode extended Bose-Hubbard Hamiltonian to describe the system. The derivation is based on a low energy model, similar to the one introduced in chapter 5, but in this case the transverse motion is completely decoupled from the axial one, since the presence of the optical lattice pins the dipoles and suppresses the coupling of longitudinal and transverse excitations.

### 6.1 The structural transition for pinned particles

The dynamics we intend to analyse merges two models which have been recently studied in the literature. One is the extended Bose Hubbard model along one dimension [DTBA06, BSRG13]. The other is the transverse structural instability due to the repulsive interatomic potential. The structural instability has a classical and a quantum component: The first is important in order to choose a convenient single-particle basis set for the purpose of deriving an appropriate Bose-Hubbard model catching the relevant features of the system.

In this section we review the basic properties of the linear-zigzag instability, assuming an array of dipoles which are confined on a plane (which we choose to be the  $x - y$  plane) and are pinned at equidistant positions along  $x$ , such that  $x_j = ja$  with  $j = 1, \dots, N$ . The only motion the dipoles can perform is thus along the  $y$  axis, where they are confined by an external harmonic trap. Depending of the trap's frequency  $\omega_y$  and on the interparticle distance  $a$ , the classical ground state of the dipoles is either a linear array or a zigzag structure. In section 5.4 we derived a low energy model to describe the structural transition

when the motion along  $x$  is allowed. Using the same method, we highlight the main steps that were used to map the system to a  $\phi^4$  model if the particles are pinned.

The transition of the pinned particles was studied by Silvi et al. [SCMM14] in the quantum regime. We will in the following review the formalism that was introduced in [SCMM14] and later expand it to also include the motion along  $x$ .

### 6.1.1 Low energy model

We assume  $N$  particles with mass  $M$  and dipolar moment  $\mathbf{p}$ , which are polarized along the  $z$ -axis by an external electric field.<sup>1</sup> Their interaction potential as a function of the interparticle distance  $\mathbf{r}$  reads

$$U_a(\mathbf{r}) = \frac{p^2}{r^3} - \frac{3(\mathbf{p} \cdot \mathbf{r})^2}{r^5}, \quad (6.1)$$

and because of the polarizing field it is repulsive on the  $x - y$  plane.

The particles are confined in the  $y$ - and  $z$ -direction by an anisotropic harmonic trap, with potential

$$V_{\text{trap}}(\mathbf{r}) = \frac{1}{2}M(\omega_y^2 y^2 + \omega_z^2 z^2). \quad (6.2)$$

The motion along  $z$  is freezed out by assuming  $\omega_y \ll \omega_z$  and sufficiently low energies. Therefore, the particles motion is constrained on the  $x - y$  plane where the dipole-dipole interaction is repulsive and is governed by the Hamiltonian:

$$H = \sum_{j=1}^N \left[ \frac{p_{j,y}^2}{2M} + \frac{M\omega_y^2}{2} y_j^2 \right] + \frac{C_D}{2} \sum_{i \neq j} [a^2(i-j)^2 + (y_i - y_j)^2]^{-3/2}, \quad (6.3)$$

where  $p_j$  and  $y_j$  are the transverse momentum and position of dipole  $j$  and we assumed that the particles are pinned in the  $x$  direction corresponding to  $y = z = 0$ . For convenience we adopt dimensionless units and rescale  $\tilde{y}_j = y_j/a$ ,  $\tilde{H} = H/\mathcal{E}_0$ ,  $\tilde{p}_j = p_{y,j}/\sqrt{M\mathcal{E}_0}$ , and finally  $\tilde{\omega} = \omega_y/\sqrt{\mathcal{E}_0/Ma^2}$ , with  $\mathcal{E}_0 = C_D/a^3$  the energy scale, and rewrite Eq. (6.3) as

$$\tilde{H} = \frac{1}{2} \sum_{j=1}^N \left( \tilde{p}_j^2 + \tilde{\omega}^2 \tilde{y}_j^2 + \sum_{i \neq j} \frac{1}{[(i-j)^2 + (\tilde{y}_i - \tilde{y}_j)^2]^{3/2}} \right), \quad (6.4)$$

where now quantum fluctuations are determined by the effective Planck's con-

<sup>1</sup>For the sake of simplicity we consider electric dipoles, but the derivation holds also for magnetic dipoles, once they are aligned by a magnetic field.

stant  $\tilde{g}$ ,  $\tilde{g} = \sqrt{\hbar^2 a / (M C_D)}$ , such that the commutator  $[\tilde{y}_i, \tilde{p}_j] = i\tilde{g}\delta_{i,j}$ . In position representation, hence,  $\tilde{p}_j = -i\tilde{g}(\partial/\partial\tilde{y}_j)$ .

### 6.1.2 Low-energy theory

In the limit in which the dipoles are localized about the chain axis, the dipole-dipole interaction can be expanded in a Taylor series. In second-order, the analysis of the dispersion relation obtained for the quadratic form of Eq. (6.4) delivers the mean-field critical point, at which one eigenfrequency vanishes. The chain instability is driven by the zigzag mode  $\tilde{y}_j = (-1)^j y_0$ , with  $y_0$  a constant amplitude. Close to the instability, a low-energy expansion yields the effective Hamiltonian

$$\tilde{H} = \frac{1}{2} \sum_{j=1}^N \left[ -\tilde{g}^2 \frac{\partial^2}{\partial \tilde{y}_j^2} + (\tilde{\omega}^2 - \mathcal{M}_1) \tilde{y}_j^2 + \mathcal{N}_1 (\tilde{y}_j + \tilde{y}_{j+1})^2 + \mathcal{M}_2 \tilde{y}_j^4 \right], \quad (6.5)$$

which describes short-ranged interactions. This property is the result of a mapping, which is strictly valid in the low energy limit. The dimensionless coefficients read  $\mathcal{N}_1 = (9/4)\zeta(3)$ , and

$$\mathcal{M}_{q=1,2} = \frac{(2^{3+2q} - 1) \Gamma(q + \frac{3}{2})}{q! 4 \Gamma(\frac{3}{2})} \zeta(3 + 2q),$$

with  $\zeta(\ell)$  Riemann's zeta function and  $\Gamma(z)$  the Gamma's function [AS64]. From the form of Hamiltonian (6.5) one can directly read the mean-field critical frequency, at which the chain becomes unstable. We denote it by  $\tilde{\omega}_c = \sqrt{\mathcal{M}_1}$ , such that in physical units it reads

$$\omega_c = \sqrt{\mathcal{M}_1 p^2 / (M a^5)}. \quad (6.6)$$

For later convenience, we observe that we can recast Hamiltonian (6.5) in the sum of a local and of an interaction component:

$$\tilde{H} = \sum_j \left( H_{\text{loc}}^{(j)} + H_{\text{int}}^{(j,j+1)} \right),$$

with

$$H_{\text{loc}} = \frac{1}{2} \left[ -g^2 \frac{\partial^2}{\partial \tilde{y}^2} + (\tilde{\omega}^2 - \mathcal{M}_1) \tilde{y}^2 + \mathcal{M}_2 \tilde{y}^4 \right]. \quad (6.7)$$

This decomposition turns out to be convenient as it allows one to map this Hamiltonian to a  $\phi^4$  Landau model, treat  $H_{\text{int}}$  as a perturbation, and it will be important in order to define the single-particle basis set for developing the multi-mode Bose-Hubbard model.

### 6.1.3 Motion along the chain

The above derivation assumes that transverse and axial motion are decoupled, which is a valid assumption when the particles are pinned or in general when the chain is incompressible. The latter condition can be realised with ions interacting via the Coulomb repulsion: In this case transverse and axial modes effectively decouple and the transverse instability is described by a  $\phi^4$  model. For dipoles, instead, the chain is incompressible if the dipoles are trapped by a sufficiently deep optical lattice, forming a Mott-Insulator. In this case, there is an energy gap between axial and transverse excitations that allows to decouple their motion at sufficiently low energies. When instead the chain is compressible, for instance in the superfluid phase, we expect that this coupling becomes relevant, changing the nature of the transition. In the next section we will systematically develop a Bose-Hubbard model for the dynamics of ultracold dipolar bosons in a tube and analyse the interplay between dipolar repulsion, quantum fluctuations, and transverse confinement.

## 6.2 Derivation of the multi-mode Bose-Hubbard model

We now assume the same geometry as in the previous section, where now the dipolar molecules are ultracold, they obey Bose-Einstein statistics, and interact via the dipolar interaction and  $s$ -wave collision. They are confined by an optical lattice along the  $x$  direction, where  $a$  now is the lattice constant, and we account for their quantum fluctuations in all three directions of space. To establish a clear connection to the linear to zigzag transition of pinned particles, we will later split the dipolar interaction into the part of the pinned linear to zigzag transition, and the part that contains all remaining terms, such that the dipolar interaction energy is  $U_{int} = U_{incomp} + U_{rest}$ , with

$$U_{incomp} = \frac{C_D}{2} \sum_{[j \neq l]} \left[ \frac{1}{((j-l)^2 a^2 + (y_j - y_l)^2)^{3/2}} \right],$$

$$U_{rest} = \frac{C_D}{2} \sum_{j \neq l} \left[ \frac{1}{|\mathbf{r}_j - \mathbf{r}_l|^3} - \frac{3(z_j - z_l)^2}{|\mathbf{r}_j - \mathbf{r}_l|^5} \right] (1 - \delta(x_j - ja)\delta(x_l - la)\delta(z_j)\delta(z_l)).$$

For now, the Hamiltonian  $\mathcal{H}$  governing their quantum dynamics is reported in second quantization, with  $\Psi(\mathbf{r})$  the molecular field operator annihilating a

boson at position  $\mathbf{r}$  such that  $[\Psi(\mathbf{r}), \Psi(\mathbf{r}')^\dagger] = \delta^{(3)}(\mathbf{r} - \mathbf{r}')$ :

$$\begin{aligned} \mathcal{H} = & \int d^3r \Psi^\dagger(\mathbf{r}) \left[ -\frac{\hbar^2}{2M} \nabla^2 + V_L \cos^2(\pi x/a) + V_{\text{trap}}(\mathbf{r}) \right] \Psi(\mathbf{r}) \\ & + \frac{1}{2} \int d^3r \int d^3r' \Psi^\dagger(\mathbf{r}) \Psi^\dagger(\mathbf{r}') U(\mathbf{r} - \mathbf{r}') \Psi(\mathbf{r}') \Psi(\mathbf{r}), \end{aligned} \quad (6.8)$$

where  $V_L$  is the depth of the optical lattice and  $U(\mathbf{r}) = U_d(\mathbf{r}) + U_g(\mathbf{r})$  is the sum of the dipolar and of the contact interaction, where  $U_g(\mathbf{r}) = g\delta(\mathbf{r})$  and  $g$  a function of the  $s$ -wave scattering length.

### 6.2.1 Complete set of field operators

In the following we assume that the molecules are tightly bound at the minima of the optical lattice and we perform the single-band approximation. In this limit we denote by  $w_j(x)$  the real-valued Wannier function for the one-dimensional single-particle lattice Hamiltonian along  $x$ . The single-particle eigenstate in the  $y$  and  $z$  directions are the eigenstates of the corresponding single particle potentials with quantum numbers  $m, n$  and eigenfunction  $\phi_m(y)$  and  $\theta_n(z)$ . In particular,  $\phi_m(y)$  are the eigenstates of the local Hamiltonian (6.7), rescaled by  $\mathcal{E}_0$ , while  $\theta_n(z)$  are the eigenstates of the harmonic oscillator in the  $z$  direction. Using the eigenbasis  $\{|j, m, n\rangle\}$  we decompose the field operator as

$$\Psi(\mathbf{r}) = \sum_{j,m,n} w_j(x) \phi_m(y) \theta_n(z) a_{jmn}, \quad (6.9)$$

where  $a_{jmn}$  is the bosonic operator which annihilates a particle in the state  $|j, m, n\rangle$ .

We further assume that  $\omega_z$  is chosen to be sufficiently large that we can assume a quasi two-dimensional geometry, where only the lowest eigenstate  $\theta_0(z)$  of the  $z$ -oscillator is occupied. Thus we restrict the basis to the states

$$\Psi(\mathbf{r}) = \sum_{j,m} w_j(x) \phi_m(y) \theta_0(z) a_{jm}, \quad (6.10)$$

where  $a_{jm} \equiv a_{jm0}$ .

### 6.2.2 Multi-mode Bose-Hubbard model

Substituting Eq. (6.10) in Hamiltonian (6.8) and keeping only nearest neighbor interactions, we then obtain that the Hamiltonian can be decomposed as the

sum of the motion along  $x$ , the motion along  $y$ , and their interaction,

$$H_{BH} = H_x + H_y + H_I. \quad (6.11)$$

In detail,  $H_x = \sum_m H_m^x$  with

$$\begin{aligned} H_m^x &= -J^x \sum_j \left( a_{jm}^\dagger a_{j+1,m} + \text{H.c.} \right) + \sum_j \epsilon n_{jm} \\ &+ \frac{U_m^x}{2} \sum_j n_{j,m} (n_{j,m} - 1) + V_m^x \sum_j n_{j,m} n_{j+1,m} \\ &+ \frac{P_m^x}{2} \sum_j \left( a_{jm}^\dagger a_{jm}^\dagger a_{j+1,m} a_{j+1,m} + \text{H.c.} \right) \\ &- T_m^x \sum_j a_{jm}^\dagger (n_{jm} + n_{j+1,m}) a_{j+1,m} \end{aligned} \quad (6.12)$$

and  $n_{j,m} = a_{jm}^\dagger a_{jm}$ . The first three terms on the right-hand side are the typical terms of the Bose-Hubbard model, with  $\epsilon$  the single-particle energy in the lattice. This time, however, the coefficients depend on the excitation  $m$  in the transverse direction and the on-site interaction term contains the contribution of the dipole-dipole interaction. All other terms are solely due to dipole-dipole interaction. For  $m = 0$ , this Hamiltonian is the same as in Ref. [SDH<sup>+</sup>12]. Discarding the pair hopping term, proportional to  $P_m^x$ , and the density-dependent tunnelling, proportional to  $T_m^x$ , the Hamiltonian reduces to the extended Bose-Hubbard model studied in Refs. [DTBA06], [BSRG13], [BRS14].

The Hamiltonian governing the motion along  $y$ , coupling different excitations  $m$  keeping  $j$  fixed, takes the form  $H_y = \sum_j H_j^y$

$$\begin{aligned} H_j^y &= \sum_m \mathcal{E}_0 \epsilon_m n_{j,m} - \sum_{m,n} J_{m,n}^y a_{j,m}^\dagger a_{j,n} + \sum_{l,m,n,q}' U_{l,m,p,q}^y a_{jl}^\dagger a_{jm}^\dagger a_{j,n} a_{j,q} \\ &+ \sum_{l,m,n,q}' P_{l,m,n,q}^y a_{jl}^\dagger a_{jm}^\dagger a_{j,n} a_{j,q}, \end{aligned} \quad (6.13)$$

where  $\sum'$  indicates that at least one of the indices  $l, m, p, q$  is different from the others and  $\epsilon_m$  is the eigenenergy of state  $\phi_m(y)$  for Hamiltonian  $H_{\text{loc}}$ . Note that the coefficients are independent of the site  $j$  in the lattice being the Hamiltonian invariant per discrete translation.

Finally,  $H_I$  describes the interaction between excitations along the  $x$  and the  $y$  direction, it is solely due to the dipolar interaction and can be cast in the

sum  $H_I = \sum_j \sum_{l_1, l_2, l_3 \neq j} \sum'_{mnqr} h_{j:l_1 l_2 l_3:mnqr}$  with

$$h_{j:l_1 l_2 l_3:mnqr} = V_{l_1 l_2 l_3:mnqr} a_{jm}^\dagger a_{l_1, n}^\dagger a_{l_2, q} a_{l_3, r} \quad (6.14)$$

### 6.2.3 The Bose-Hubbard parameters

The purpose of this and the following sections is to determine the ground state of this multi-mode extended Bose-Hubbard model as a function of the relevant physical parameters, namely: (i) the size of quantum fluctuations  $J^x$ , which are controlled by the depth of the optical lattice  $V_L$ , (ii) the on-site interaction coefficients  $U_m^x$  and  $U_{l,m,p,q}^y$ , which are tuned by the  $s$ -wave scattering length, the lattice height  $V_L$  and the dipole moment; (iii) the transverse frequency  $\omega_y$  which determines the form of the transverse potential and thus affects the form of these coefficients; (iv) the dipole-dipole interaction, which can be tuned by changing the interparticle distance  $a$ ; (v) the size of the ground state along  $z$ , which affects the form of the dipolar interaction. Below we discuss in detail the form of the Bose-Hubbard parameters.

The tunneling term  $J^x$ ,  $J^y$  specifically read

$$J^x = \int dx w_j(x) \left( \frac{\hbar^2}{2M} \frac{\partial^2}{\partial x^2} - V_L \sin^2(kx) \right) w_{j+1}(x), \quad (6.15)$$

$$J_{mn}^y = -\mathcal{E}_0 \int dy \phi_m(y) \mathcal{N}_1 y^2 \phi_n(x), \quad (6.16)$$

while the on-site interaction coefficients take the form

$$U_m^x = \int d^3 r_1 \int d^3 r_2 U(\mathbf{r}_1 - \mathbf{r}_2) w_j(x_1)^2 \phi_m^2(y_1) \theta_0^2(z_1) w_j(x_2)^2 \phi_m^2(y_2) \theta_0^2(z_2), \quad (6.17)$$

$$U_{l,m,p,q}^y = \int d^3 r_1 \int d^3 r_2 U(\mathbf{r}_1 - \mathbf{r}_2) w_j^2(x_1) \theta_0^2(z_1) w_j^2(x_2) \theta_0^2(z_2) \phi_l(y_1) \phi_m(y_2) \phi_n(y_1) \phi_q(y_2), \quad (6.18)$$

where

$$U(\mathbf{r}_1 - \mathbf{r}_2) = U_g(\mathbf{r}_1 - \mathbf{r}_2) + U_d(\mathbf{r}_1 - \mathbf{r}_2)$$

includes the dipolar interaction and the interaction due to  $s$ -wave scattering.

Finally, the terms due to the dipole dipole interaction are given by the following integrals

$$V_m^x = \int d^3 r_1 \int d^3 r_2 U_d'(\mathbf{r}_1 - \mathbf{r}_2) w_j(x_1)^2 w_{j+1}(x_2)^2 |\phi_m(y_1) \phi_m(y_2)|^2 |\theta_0(z_1) \theta_0(z_2)|^2, \quad (6.19)$$

$$P_m^x = \int d^3r_1 \int d^3r_2 U'_d(\mathbf{r}_1 - \mathbf{r}_2) w_j(x_1) w_{j+1}(x_1) w_j(x_2) w_{j+1}(x_2) |\phi_m(y_1) \phi_m(y_2)|^2 |\theta_0(z_1) \theta_0(z_2)|^2, \quad (6.20)$$

$$T_m^x = - \int d^3r_1 \int d^3r_2 U'_d(\mathbf{r}_1 - \mathbf{r}_2) w_j(x_1)^2 w_j(x_2) w_{j+1}(x_2) |\phi_m(y_1) \phi_m(y_2)|^2 |\theta_0(z_1) \theta_0(z_2)|^2, \quad (6.21)$$

$$P_{l,m,n,q}^y = \int d^3r_1 \int d^3r_2 U'_d(\mathbf{r}_1 - \mathbf{r}_2) w_j(x_1)^2 w_j(x_2)^2 \phi_l^*(y_1) \phi_m^*(y_2) \phi_n(y_2) \phi_q(y_1) |\theta_0(z_1) \theta_0(z_2)|^2, \quad (6.22)$$

$$\begin{aligned} V_{l_1 l_2 l_3: m n q r} &= \int d^3r_1 \int d^3r_2 U'_d(\mathbf{r}_1 - \mathbf{r}_2) w_j(x_1) w_{l_1}(x_2) w_{l_2}(x_2) w_{l_3}(x_1) \\ &\quad \times \phi_m^*(y_1) \phi_n^*(y_2) \phi_q(y_1) \phi_r(y_2) |\theta_0(z_1) \theta_0(z_2)|^2 \\ &\quad + \delta_{j,l_2} \delta_{l_1,l_3} \mathcal{E}_0 \mathcal{N}_1 \int dy_1 \phi_m(y_1) y_1 \phi_q(y_1) \int dy_2 \phi_n(y_2) y_2 \phi_r(y_2). \end{aligned} \quad (6.23)$$

Here  $U'_d(\mathbf{r})$  corresponds to the term

$$U'_d(\mathbf{r}) = U_d(\mathbf{r})(1 - \delta(x-a)\delta(z)). \quad (6.24)$$

The numerical calculation of the integrals is performed by first integrating out the  $z$  variables in Fourier space, as we show in Appendix A.

These integrals show explicitly the dependence on the confinement in the  $z$  direction, which enters through the wavepacket

$$\theta_0(z) = \frac{1}{\sqrt{\sqrt{\pi}\sigma_z}} \exp\left(-\frac{z^2}{2\sigma_z^2}\right), \quad (6.25)$$

where  $\sigma_z = \sqrt{\hbar/(M\omega_z)}$ . Its effect is important: In fact, fluctuations along  $z$  are affected by the attractive component of the dipole-dipole interaction. As they increase, they can modify substantially the behaviour of some coefficients. One example is provided in Fig. 6.1, where it becomes visible that increasing  $\sigma_z$  can change the on-site interaction from repulsive to attractive.

### 6.3 Observables and Phases

The multi-mode Bose-Hubbard model we have derived contains several components, some of them correspond to a limit that has been discussed in the literature. We first focus on the one-dimensional model, which we obtain for  $\omega_y$  well above the critical value, such that there is an energy gap between the lowest and the first excitation of the transverse harmonic oscillator. In this case the model is effectively one-dimensional, and the phase diagram is de-

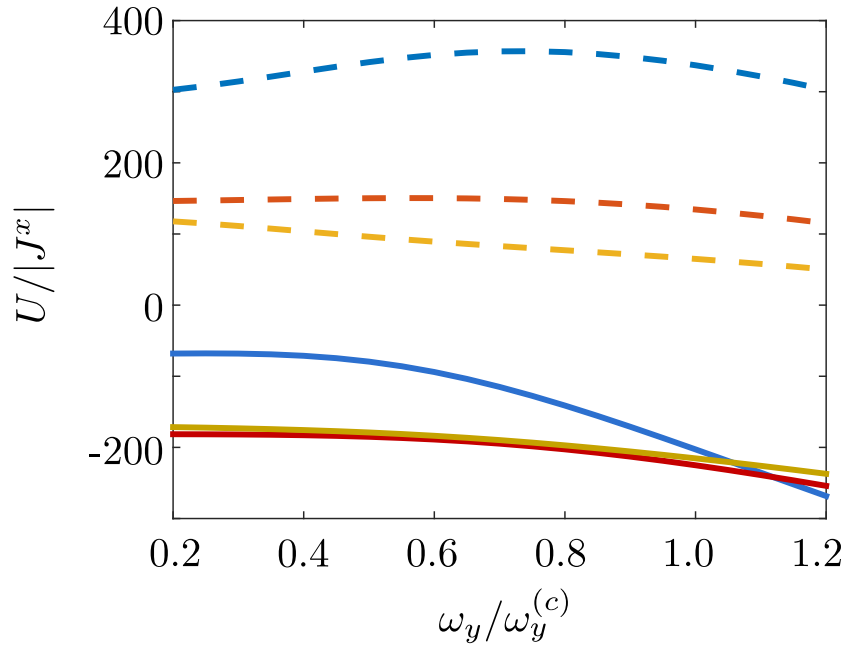


**Figure 6.1** – The on site interaction coefficients  $U_0^x$  (in units of  $|J^x|$ ) and as a function of  $\omega_y/\omega_y^{(c)}$  for  $\sigma_z = 0.3375a$  (solid lines) and  $\sigma_z = 0.18a$  (dashed lines) for an optical lattice depth of  $V_L = 10E_R$  for different trap frequencies  $\omega_y$ . Blue shows  $U_m^x$  for  $m = 0$ , red for  $m = 1$  and yellow for  $m = 2$ .

scribed by Hamiltonian of Eq. (6.12) for  $m = 0$  derived in Ref. [SDH<sup>+</sup>12]. For vanishing dipolar interactions, this Hamiltonian reduces to the Bose-Hubbard Hamiltonian that was introduced in chapter 2.2 and predicts the existence of Mott-insulating (MI) or superfluid (SF) phases, depending on the ratio between hopping and on-site interaction energy,  $J^x/U^x$ . The superfluid is characterized by long-range order in the off diagonal elements  $\langle a_j^\dagger a_l \rangle$  and a non-zero superfluid density. The quantities which are used in order to differentiate between these two phases in small systems are the local compressibility  $\delta n_j$  and the off-diagonal correlations (one-particle correlation function)  $\phi$ , namely:

$$\begin{aligned}\Delta n_j &= \langle \delta n_j \rangle^2, \\ \phi &= \sum_j \langle a_j^\dagger (a_{j+1} + a_{j-1}) \rangle,\end{aligned}$$

where

$$\delta n_j = n_j - \langle n_j \rangle \quad (6.26)$$

and the expectation value is taken over the ground state of the Hamiltonian and we use periodic boundary conditions. Note that the phase is incompressible when  $\delta n_j$  vanishes at all sites  $j$ . While the correlation function  $\phi$  is not exactly zero in the Mott insulating phase of a large system, it displays a sharp decrease from the value found in the superfluid and is an effective measure for exact diagonalization. For our multi-mode model and a numerical procedure based on exact diagonalization, we adopt a generalization of these quantities, such that

$$\Delta n_j \rightarrow \Delta n_j = \sum_m \langle n_{j,m}^2 \rangle - \langle n_{j,m} \rangle^2, \quad (6.27)$$

$$\phi \rightarrow \phi = \sum_{j,m} \langle a_{j,m}^\dagger (a_{j+1,m} + a_{j-1,m}) \rangle. \quad (6.28)$$

By taking the Hamiltonian (6.12) and including solely the term scaling with the coefficient  $V_m^x$  (thus arbitrarily setting  $T_m^x = P_m^x = 0$ ) the Hamiltonian for  $m = 0$  takes the form of the extended Bose-Hubbard model studied by Batrouni et al. [BSRG13] and Dalla Torre et al. [DTBA06], amongst others. The presence of  $V^x$  tends to induce a density modulation along  $x$ , that is signaled by a static structure form factor  $S_x(q)$  with non vanishing component at  $q = \pi$ , where

$$S_x(q) = N^{-2} \sum_{j,l=1}^N e^{i(j-l)q} (\langle n_j n_l \rangle - \langle n_j \rangle \langle n_l \rangle). \quad (6.29)$$

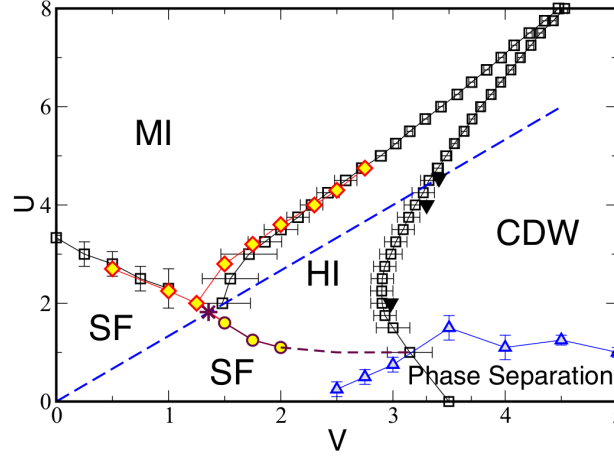


**Figure 6.2** – Phase diagram of the single-band extended Bose-Hubbard Hamiltonian taken from Batrouni et al. [BRSG14] for the filling  $\rho = \langle n_i \rangle = 1$ . The on-site interaction  $U$  and the nearest neighbor interaction  $V$  is given in units of  $J^x$ .

Provided  $S_x(\pi) \neq 0$ , when off-diagonal correlations do not vanish, the phase is super-solid (SS). When otherwise the phase is incompressible, then the phase is a charge-density wave (CDW) [KPS05]. For our multi-mode model, we will check for possible SS or CDW phases by monitoring the structure factor for the total density  $n_j = \sum_m n_{j,m}$ .

Nevertheless, recent works also highlighted the existence of the Haldane-insulator (HI) phase, which appears by varying  $V$  between the MI and the CDW in systems with filling  $\rho = \langle n_i \rangle = 1$ , which is incompressible and characterised by  $S(\pi) = 0$ . At filling  $\langle n_i \rangle = 1$  more than two particles per site for large  $V$  and  $U$  are very unlikely. Dalla Torre et al. [DTBA06] showed that, if the Hilbert space is cut to a maximum of two occupations per site ( $n_j = 0, 1, 2$ ), the Hamiltonian (6.12) with  $T_m^x = 0 = P_m^x$  can be mapped onto a spin model,  $S_j^z = \delta n_j = n_j - \langle n_j \rangle$ , with  $S = 1$ , leading to

$$H_{sp} = J \sum_j (S_j S_{j+1}^- + \text{h.c.}) + V \sum_j S_j^z S_{j+1}^z + \frac{U}{2} \sum_j (S_j^z)^2. \quad (6.30)$$

The phase diagram of this effective spin-1 XXZ chain, has already been studied in the literature [dNR89, KT92, Sch86], and is known to display a Haldane insulator sandwiched between the Mott and the density wave phase. The full phase diagram taken from Batrouni et al. [BRSG14] of the the single-band extended Hamiltonian (6.12) for  $T_m^x = 0 = P_m^x$  and filling  $\rho = \langle n_i \rangle = 1$  is shown in Fig. 6.2. In accordance to the spin model, one defines the string order that

	$\phi$	$O_s$	$\Delta n_i$	$O_p$	$S_x(\pi)$	$\Phi$
SF	$\neq 0$	0	$\neq 0$	0	0	0
SS	$\neq 0$	0	$\neq 0$	0	$\neq 0$	0
MI	0	0	0	$\neq 0$	0	0
CDW	0	$\neq 0$	0	$\neq 0$	$\neq 0$	0
HI	0	$\neq 0$	0	0	0	0
PSF	$\neq 0$	0	$\neq 0$	0	0	$\neq 0$

**Table 6.1** – *Salient properties for identifying the phases of the BH model of Eq. (6.12) by exact diagonalization. The corresponding observables are defined in the text.*

characterizes the Haldane insulating phase as

$$O_s(|j-l|) = \left\langle \delta n_j (-1)^{\sum_{k=j}^l \delta n_k} \delta n_l \right\rangle, \quad (6.31)$$

and parity order that characterizes the Mott insulating phase and is given by

$$O_p(|j-l|) = \left\langle (-1)^{\sum_{k=j}^l \delta n_k} \right\rangle. \quad (6.32)$$

In the limit  $|j-l| \rightarrow \infty$ , the parameters  $O_p$  and  $O_s$  become the order parameter of the Mott insulator to Haldane insulator transition. The string order is zero in the Mott insulator, and not zero in the Haldane phase, while the parity order this is reversed. In practice, one takes the largest distance  $|j-l| = L/2$  in simulations with periodic boundaries to evaluate the string and parity order parameters.

The phases summarized so far characterize the phase diagram of the extended Bose-Hubbard model. The Hamiltonian in Eq. (6.12) also includes pair tunnelling terms, which can give rise to pair superfluidity (PSF) [SDH<sup>+</sup>12]. Its appearance is signaled by a non-vanishing expectation value of operator

$$\Phi = \sum_{j,m} \left( a_{j,m}^\dagger a_{j,m}^\dagger a_{j+1,m} a_{j+1,m} + a_{j,m}^\dagger a_{j,m}^\dagger a_{j-1,m} a_{j-1,m} \right), \quad (6.33)$$

giving pair-correlation functions. The salient known properties of the phases discussed so far are summarized in Table 6.1.

The observable with which we characterize the structural linear zigzag transition is the structure form factor for at the (dimensionless) wave number  $q_y = \pi$ ,

namely:

$$S_y(\pi) = \frac{1}{N^2} \sum_{j \neq l} (-1)^{j-l} \langle y_j y_l \rangle \quad (6.34)$$

$$(6.35)$$

where

$$y_j = \sum_{m,n} Y_{mn} a_{j,m}^\dagger a_{j,n}, \quad (6.36)$$

and  $Y_{m,n} = \int dy \phi_m^*(y) \phi_n(y) y$  is a real matrix that depends on the parameters of the system. In particular,  $Y_{m,n} = 0$ , if both  $m$  and  $n$  labels eigenstates of the same local Hamiltonian with the same parity. Therefore, the operator  $y_j$  only couples states with opposite parity. When  $S_y(\pi) \neq 0$ , the dipoles form a zigzag transverse structure.

## 6.4 Phase diagrams

In the following we analyse the phase diagrams in some limits. We use the parameters of  $^{85}\text{Rb}-^{133}\text{Cs}$  bosonic molecules with electric dipole moment of 1.15 Debye, confined by an optical lattice along  $x$  at the interparticle distance  $a = 395 \cdot 10^{-9}$  nm, corresponding to half wavelength of the standing-wave laser. The phase diagrams are calculated by means of the exact diagonalization of a 4 to 12 sites Hamiltonian, depending on the number of states of the local basis we consider. In this section, moreover, we will restrict to the filling of one particle per site  $j$ , unless we explicitly say otherwise.

### 6.4.1 The classical vs quantum linear-zigzag transition

We first start benchmarking how many states of the local basis we shall take as a function of the values of the transverse frequency we explore. For this purpose we take 4 sites along  $x$  with open boundary conditions and compare the predictions of the full Hamiltonian, Eq. (6.11) for large lattice depths  $V_L$  (which we take  $V_L = 100E_r$ , with  $E_r$  the recoil energy) and tight confinement along  $z$  ( $\sigma_z = 10^{-4}a$ ), with the ones of the classical Hamiltonian, obtained by discarding quantum fluctuations in Eq. (6.5). We take the mass of RbCs bosonic molecules, but modify arbitrarily the strength of the dipole moment  $p$  so to explore regimes with very different values of the effective Planck constant  $g$ , thus sweeping from a more classical ( $g \ll 1$ ) to a quantum dynamics ( $g > 0.001$ ). While this value of  $\sigma_z$  is extremely small, it is appropriate for theoretically approaching the classical limit. We plot the squared root of Eq. (6.34) taken  $\xi = \sqrt{S_y(\pi)}$ , taking for the full Hamiltonian the three lowest eigenstates of the

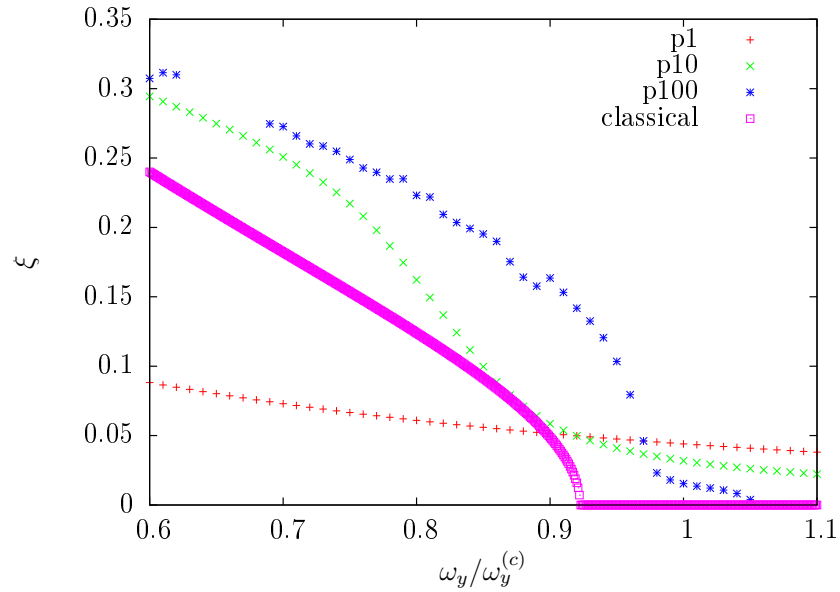


**Figure 6.3** – Parameter  $\xi = \sqrt{S_y(\pi)}$  as a function of  $\omega_y$  (in units of  $\omega_y^{(c)}$ ) for 4 particles and open boundary conditions. The purple curve shows the classical result, the other curves display the result for the ground state of  $H^{3D}$  taking  $\sigma_z = 0.01 a$  and  $V_L = 100E_r$  and a local basis composed by the first three low energy states  $\{\phi_0(y), \phi_1(y), \phi_2(y)\}$ . The color code is explained in the legenda, where p1 refers to a calculation where we took the dipole moment of RbCs molecules, p10 (p100) means that we increased  $p$  in the dipole-dipole interaction by a factor 10 (100). The third local excited state results to have occupation  $n_{j,2} = 0.001$  (red), 0.08 (green), 0.15 (blue).

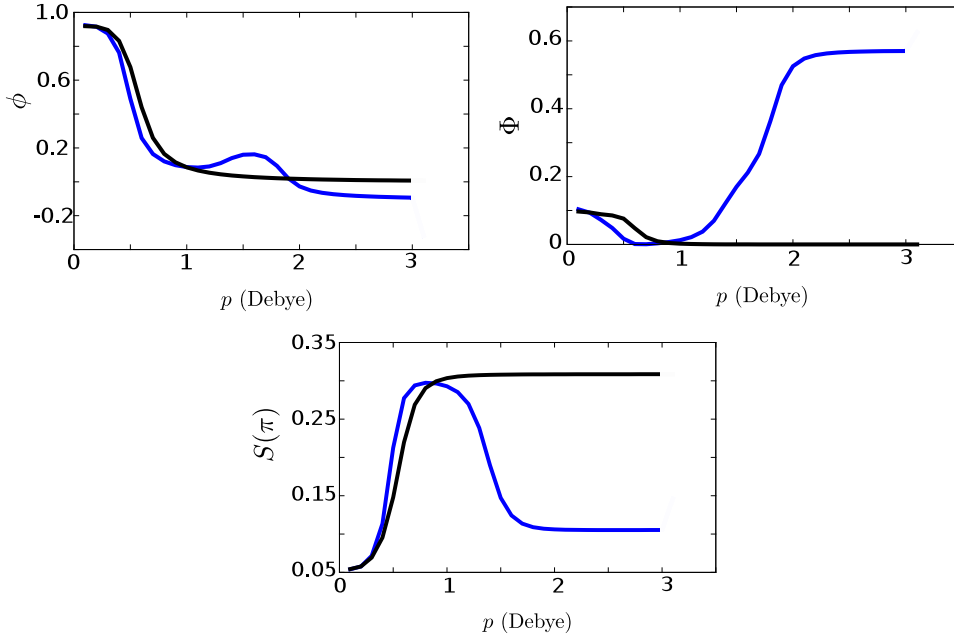


**Figure 6.4** – (a) Single-particle correlation  $\phi$ , (b) two-particle correlations  $\Phi$ , and (c)  $S(\pi)$  as a function of  $p$  for a lattice of 12 sites filled with 6 particles with periodic boundary conditions. The blue curve is for the ground state of Hamiltonian  $H_0^x$ , the black curve to the result found when we arbitrarily set  $T^x = P^x = 0$ .

transverse local Hamiltonian. Figure 6.3 shows the behaviour of  $\xi$  as a function of  $\omega_y$  for the classical prediction and the full simulation for values of the dipole moment which vary in the interval  $[1 : 100]p$ , with  $p$  the dipole moment of the RbCs molecule. As the dipole moment is increased the occupation of higher internal states increases, the same order of magnitude is found which by taking also a chain of 6 sites. Thus truncating the local basis to the first three states is justified only deep in the quantum regime. In this regime, however, the behaviour of the order parameter is a crossover, the typical features of the Landau phase transitions are lost. A more accurate calculation with TEBD and larger chain sizes will be done in section 6.5.

### 6.4.2 Benchmark: The quasi-one dimensional model

We then check whether our model reproduces the results of Ref. [SDH<sup>+</sup>12], where the phase diagram of dipolar molecules in a two-dimensional optical lattices was calculated in the regime where the Bose-Hubbard Hamiltonian can be reduced to  $H_0^x$ , namely, Eq. (6.12) with  $m = 0$ . There, it was found that the density assisted tunneling terms  $T_0^x$  and the pair tunneling terms  $P_0^x$  can lead to the appearance of pair superfluid phases. We then calculate the ground state

of the full Hamiltonian, (6.11), for  $m = 0$  and using exact diagonalization for a lattice with depth  $V_L = 6E_r$ ,  $a = 100a_0$ , and for  $\sigma_z = 0.2279a$ . We first verified that the behaviour of the coefficients of the Bose-Hubbard model as a function of  $\sigma_z$  follows the behaviour reported in Ref. [SDH<sup>+</sup>12]. Below we show the behaviour of some observables, such as the single particle correlation  $\phi$ , Fig. 6.4(a), the two-particle correlations  $\Phi$ , Fig. 6.4(b), and the structure factor  $S_x(\pi)$ , Fig. 6.4(c), as a function of  $p$  for 12 sites at half-filling with periodic boundary conditions. For each value of  $p$  we take the trap frequency  $\omega_y$  such that the lowest eigenfunction of  $H_{loc}$  has the same width as the Wannier function,  $\int dx x^2 w^2(x) = \int dy y^2 \phi_0^2(y)$ . Note that the model is valid when  $\omega_y > \omega_y^{(c)}$ , otherwise one shall take further eigenfunctions  $\phi_m(y)$ . For the parameters we choose we verified that this is fulfilled for a dipole moment of less than 3 Debye. Our calculations reproduce the results of Ref. [SDH<sup>+</sup>12]. In order to highlight the role of pair and density dependent tunneling, in all figures we also give the value obtained by setting  $T^x = P^x = 0$ . We see that these terms are essential for the appearance of two-particle correlations, signaling pair superfluidity. This occurs at sufficiently large value of  $p$ , which in turn scales the corresponding  $T^x$  and  $P^x$  coefficients. Our calculations reproduce the results of Ref. [SDH<sup>+</sup>12].

While the results in [SDH<sup>+</sup>12] are for small fillings, we are mainly interested in the ground state for the filling  $\langle n_j \rangle = 1$ . For this reason, we explore the phase diagram for this filling for various values of the s-wave scattering length and dipole moments. Figs. 6.5a-6.5c show the single particle correlation  $\phi$ , the two particle correlation  $\Phi$  and the structure factor  $S_x(\pi)$  calculated by exact diagonalization for 10 particles using  $a = 50a_0$ ,  $\omega_y = 1.45\omega_y^{(c)}$  and  $\sigma_z = 0.25a$ . For small dipole moments, the interaction, the neighbour interaction coefficient  $V_m^x \approx 0$  and the ground state has non-zero one- and two-particle correlations. We also verified that the local compressibility  $\kappa_i$  is zero in this region, which indicates a superfluid state. (This agrees with the prediction of the simple Bose-Hubbard Hamiltonian [BS92].) For large dipole moments and large transverse width  $\sigma_z$ , the on-site interaction coefficients  $U_0^x$  become negative. In these regions, the system is unstable (marked in red) as it favours configurations where all particles sit on one-site. Surrounding the unstable region is a checkerboard or density-wave region. It is characterized by a non-zero structure factor, while the single and two particle correlations  $\phi$ ,  $\Phi$  vanish. Interestingly  $\phi$  and  $\Phi$  are not zero just at the border to the density-wave phase, which might hint at a small region of supersolidity.

Finally the ground state for a constant dipole moment of  $p = 1.15$  Debye is calculated for various values of the contact interaction  $g$  and widths  $\omega_z$ . Figures 6.6a-6.6c show the three observables  $\phi$ ,  $\Phi$  and  $S(\pi)$ . A superfluid phase appears for a large range of s-wave scattering lengths, but a small interval of the transverse width  $\sigma_z$ . For slightly smaller values of  $\sigma_z$  the system is in a MI, for slightly larger values in a DW. The unstable region where  $U_0^x < 0$  occurs for

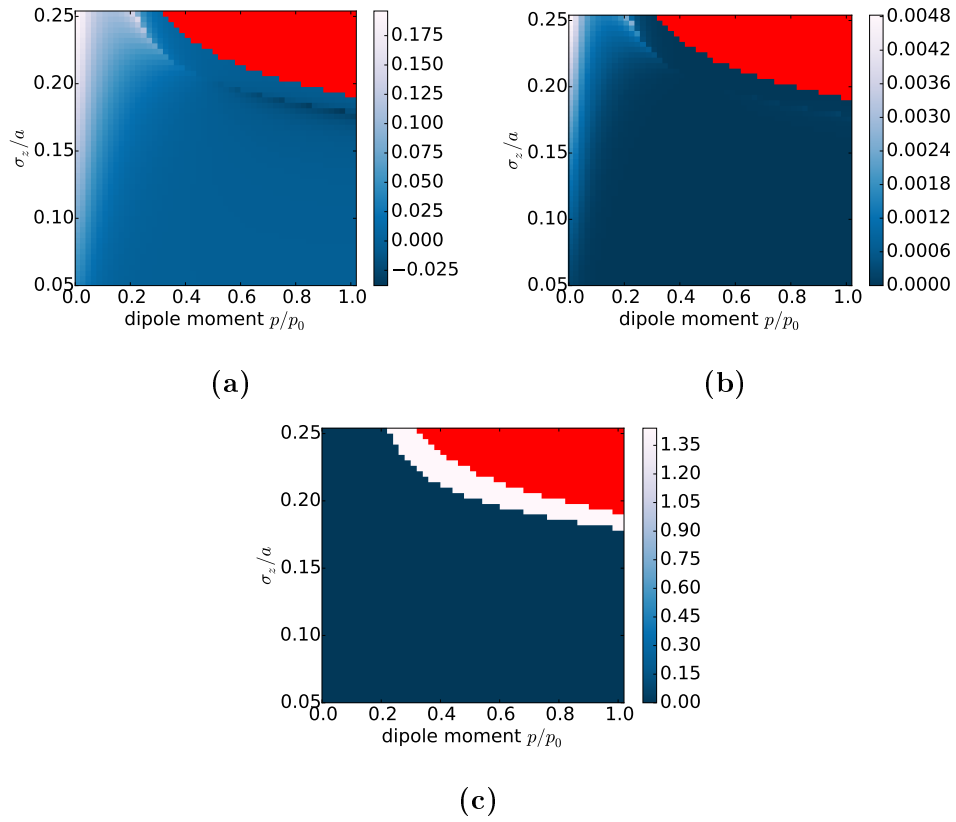


**Figure 6.5** – The single particle correlations  $\phi$  (a), the two particle correlations  $\Phi$  (b) and the structure factor  $S(\pi)$  (c) for  $\lambda = 20E_R$ ,  $a = 50a_0$  for varying  $\sigma_z$  and dipole moment  $p$  in units of  $p_0 = 1.15$  Debye. The red area is the region where the on-site interaction  $U_0^x$  is negative.

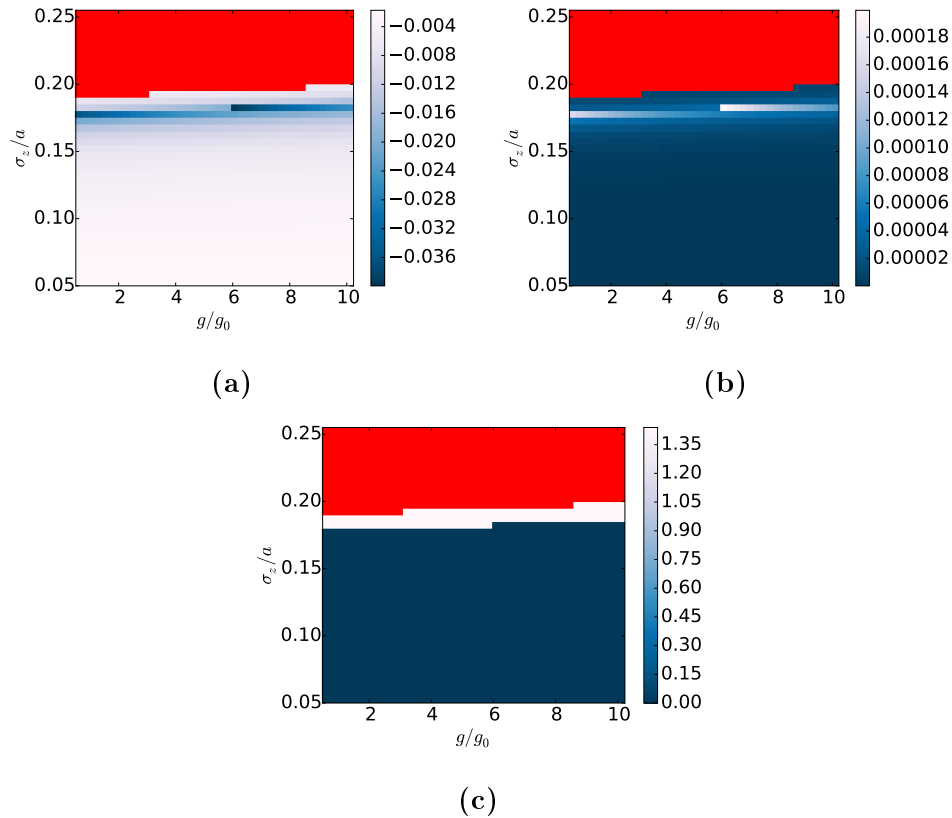


**Figure 6.6** – The single particle correlations  $\phi$  (a), the two particle correlations  $\Phi$  (b) and the structure factor  $S(\pi)$  (c) for  $\lambda = 20E_R$ ,  $a = 50a_0$  for varying  $\sigma_z$  and dipole moment  $p$  in units of  $p_0 = 1.15$  Debye. The red area is the region where the on-site interaction  $U_0^x$  is negative.

large  $\sigma_z$ .

In the next few section we will use two numerical methods that allow the study of larger systems. The first method is a finite temperature path integral Monte-Carlo (PIMC), that we use to analyze the single-band Hamiltonian and recover the exotic Haldane insulator phase. We also show in Appendix B that the PIMC is not able to analyze the full Hamiltonian, as there is the occurrence of a sign problem. For this reason, we resort to a second numerical method, the TEBD algorithm that is based on the Matrix Product State formalism to calculate the ground state of the system.

### 6.4.3 The results of the PIMC applied to the EBH

In the following, we will study the single band Hamiltonian (6.12) for  $T^x = P^x = 0$ , with the world line path integral Monte Carlo algorithm described

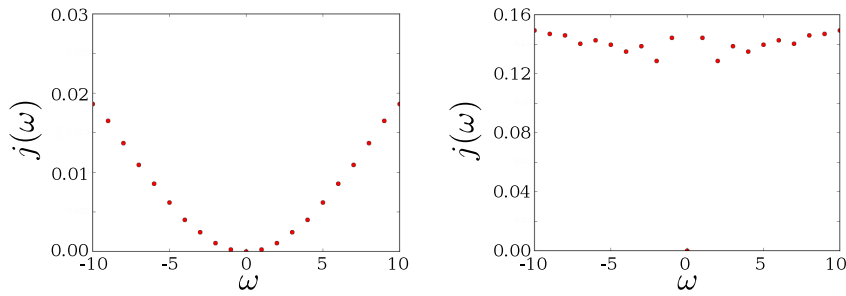


**Figure 6.7** – The Fourier transform of the pseudo-current correlator  $C_j(\omega)$  at  $U/|J^x| = 40$  for 32 sites for 32 particles (left) and 31 particles (right). The superfluid density is proportional to the value extrapolated at  $\omega \rightarrow 0$ .

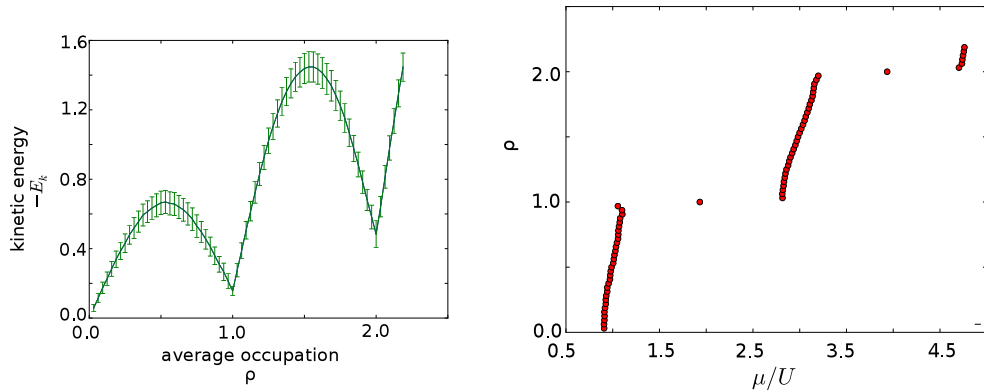
in Appendix B, where it is also explained why the full Hamiltonian cannot be studied with this algorithm.

First, we study the case of zero dipolar moment. In this limit, we benchmark the algorithm by checking that we recover the superfluid and Mott insulating phase. We identify the Mott lobes by calculating the kinetic energy for various numbers of particles at a fixed number of lattice sites. For commensurate fillings, the kinetic energy is minimal, indicating a Mott insulator. Figure 6.8a shows the kinetic energy for various fillings calculated with the PIMC.

Another feature of Mott insulators is the vanishing compressibility  $\kappa = \partial\rho/\partial\mu$ , where  $\mu$  is the chemical potential. Figure 6.8b shows the density  $\rho$  as a function of the chemical potential  $\mu = E(N+1) - E(N)$ . The superfluid to Mott transition is clearly visible by observing the density plateaus for varying values of the chemical potential.

Figure 6.7 shows the Fourier transform of the pseudo-current correlation function inside the Mott insulator and outside. As it is proportional to the superfluid density, it is zero in the Mott insulator, and non-zero in the superfluid.

If the dipole moment is not zero, one expects a new Haldane phase to appear. We check this by fixing the density to one particle per site  $\rho = \langle n \rangle = 1$  and calculate the string, parity order and the structure factor as described in section 6.3. We move horizontally in the phase diagram of Fig. 6.9 starting from small nearest neighbour interactions  $V/J^x$  at fixed onsite interactions  $U/J^x$ . We find that the structure factor is zero and the string order parameter is zero, while the parity order is not, signaling a Mott insulator. For increasing values of  $V/J^x$ , the string order increases while the structure factor is still vanishing. This is an indication of the Haldane phase. At further increasing  $V/J^x$  the structure factor increases thus entering the density wave phase. We therefore recover the results of Dalla Torre et al. [DTBA06] and Batrouni et al. [BSRG13]. For smaller  $U/J^x$  and  $V/J^x$ , the system was found to be in a superfluid phase



(a) The kinetic energy versus the density at  $V = 0$  and  $U/|J^x| = 40$  at  $\beta = 32$ . The kinetic energy is minimal in the Mott insulator. The cusps signal the MI to SF transition. (b) Density versus the chemical potential. This was calculated at  $U/t = 40$ ,  $\beta = 32$  for 32 sites. The plateaus in the density as a function of the chemical potential correspond to the incompressible Mott phase.

Figure 6.8

[DTBA06, BSRG13], while for small  $U/J^x$  but large  $V/J^x$  the system is expected to be in a mixed supersolid and superfluid phase [BRS14].

However, the PIMC that we employed does not converge in the region where the tunneling is large and the dipole moment is not zero, where one expects to find the superfluid to Haldane insulator transition, or the region of phase separation that was seen in [BRS14]. For this reason we resorted to other numerical techniques, such as exact diagonalization or time evolving block decimation.

## 6.5 Time Evolving Block Decimation

In the previous section a Path integral Monte Carlo method was used to analyze the extended Bose-Hubbard Hamiltonian. However, it was only possible to analyze the phases when one set  $T^x = P^x = 0$ , as these terms lead to a sign problem in the formulation of the algorithm. Therefore, we resort to another way to numerically analyze the ground state, a Time Evolving Block Decimation (TEBD) method [Vid04, Vid03], which does not have a sign problem (see Appendix C).

### 6.5.1 Results for the single band Hamiltonian

First we apply the TEBD algorithm to the single band Hamiltonian (6.12) for  $m = 0$  for the same parameters as in section 6.4, where we saw that the

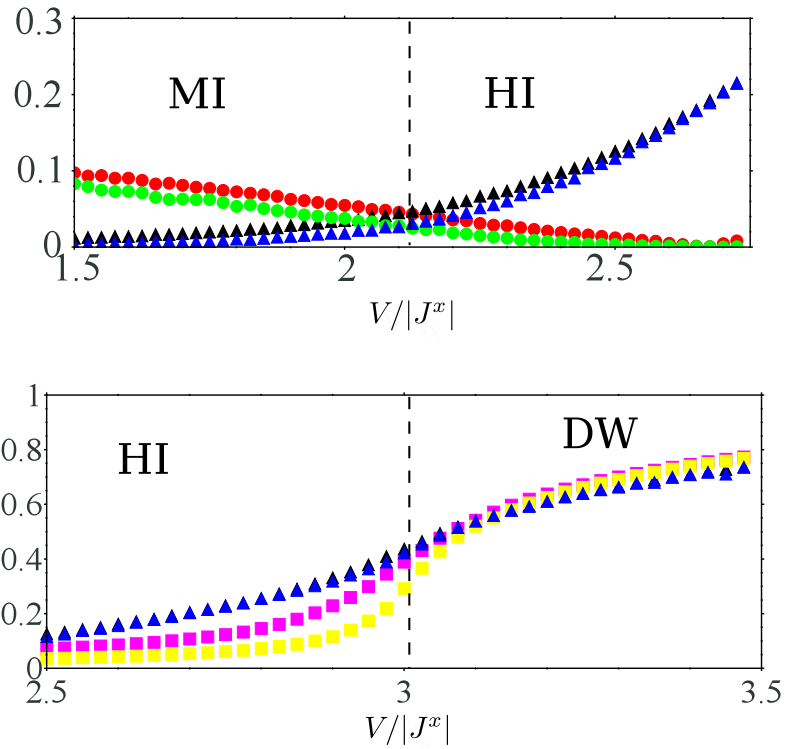


**Figure 6.9** – The string order, parity order and structure factor  $S(\pi)$  at  $U = 4$  at  $\beta = 32$ . The parity order for  $64$  and  $32$  particles is shown as red and green circles, respectively. The string order parameter is shown in blue ( $64$ ) and black ( $32$ ) triangles, the structure factor in magenta ( $32$ ) and yellow ( $64$ ) squares .

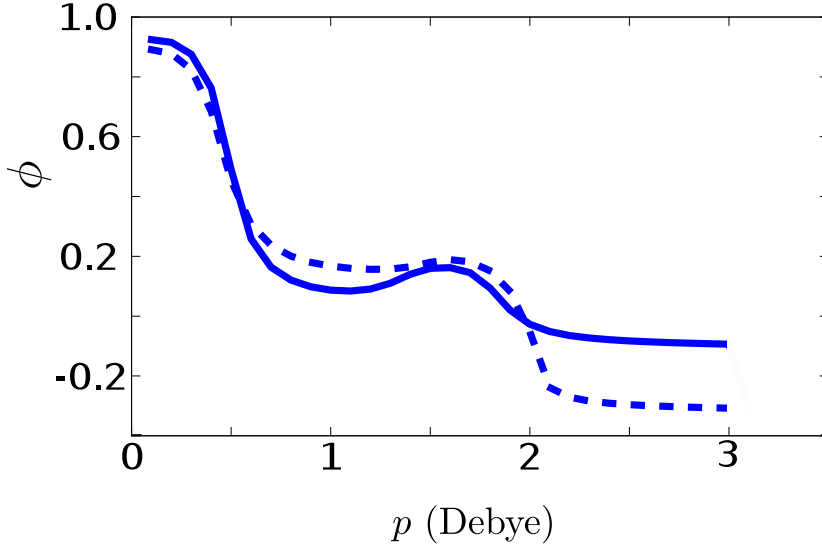


**Figure 6.10** – The single particle correlations for neighboring sites  $\phi$  for the parameters in Fig. 6.4 for 40 sites (dashed line) and 12 sites (solid line).

pair tunneling terms  $P_m^x$  and the density assisted tunneling terms  $T_m^x$  cannot be neglected when discussing small systems. By using TEBD, we are able to study larger systems and test whether these new phases are still found for a larger number of particles. Figure 6.10 shows the single particle correlation function  $\phi$  for exactly the same parameters as in Fig. 6.4, but this time for 40 sites. The single particle correlations show qualitatively the same behavior for small and large systems, but the single particle correlations are increased for larger systems. Beside the nearest neighbour correlator  $\phi$ , we also calculate the long-range correlations for the off-diagonal elements  $\Phi_{j,j+l} = a_j^\dagger a_{j+l}$  and the density-density correlations  $\langle n_j n_{j+l} \rangle$ . Both are shown in Figs. 6.11-6.13 for different dipole moments.

For small dipole moments, we indeed have a superfluid phase, as the off-diagonal correlations span over many sites. At the same time the density-density correlations show now apparent structure. A density-wave phase can be found at intermediate dipole moments of 1 Debye, where there are no long-range off-diagonal correlations, but long-range density correlations. At even larger dipole moments, one finds a different checkerboard phase, that is not a superfluid, but is brought upon by the density assisted and pair tunneling terms. The bosons occur in pairs, as can be seen in the density-density correlations.

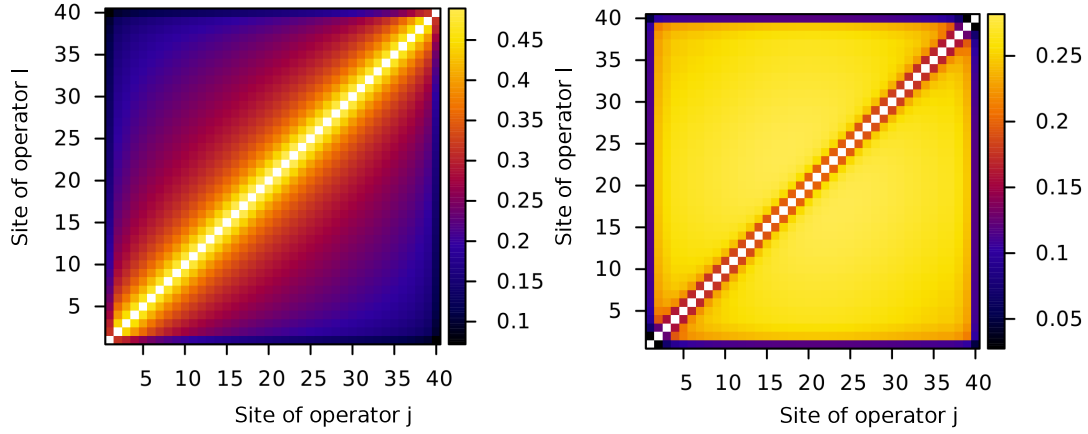


**Figure 6.11** – The single particle correlations  $a_j^\dagger a_l$  (left) and the density-density correlations  $n_j^\dagger n_l$  (right) of a lattice of 40 sites for the dipole moment  $p = 0.1$  Debye and the same parameters as in Fig. 6.4.

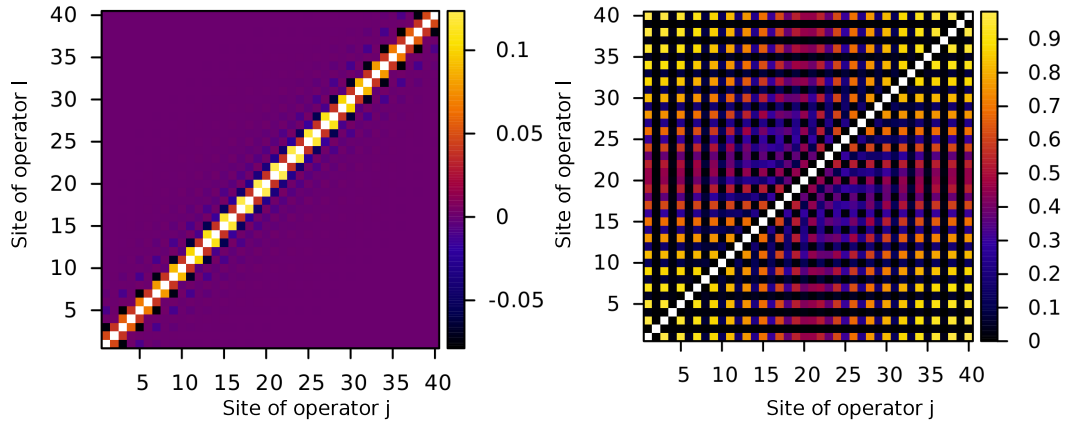


**Figure 6.12** – The single particle correlations  $a_j^\dagger a_l$  (left) and the density-density correlations  $n_j^\dagger n_l$  (right) of a lattice of 40 sites for the dipole moment  $p = 1$  Debye and the same parameters as in Fig. 6.4.

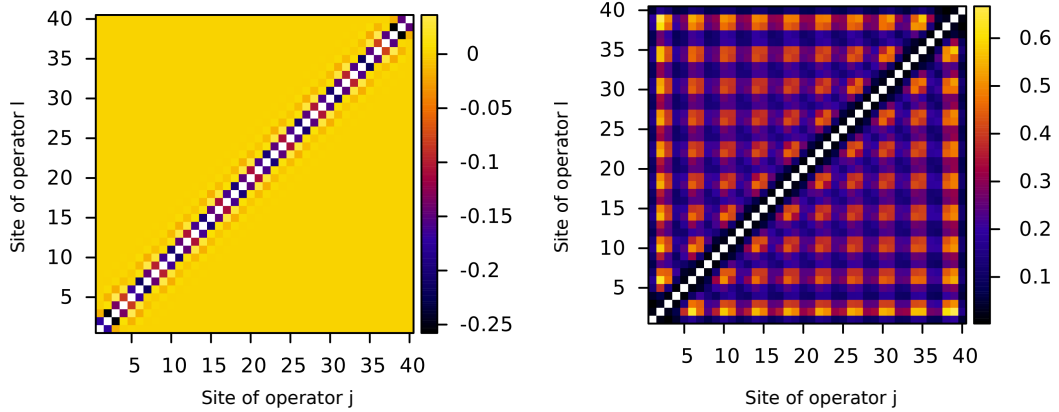


**Figure 6.13** – The single particle correlations  $a_j^\dagger a_l$  (left) and the density-density correlations  $n_j^\dagger n_l$  (right) of a lattice of 40 sites for the dipole moment  $p = 3$  Debye and the same parameters as in Fig. 6.4.

### 6.5.2 The zigzag transition

By using exact diagonalization, we already studied in section 6.4.1 the ground state of a few particles deep in the tight-binding limit ( $V_L = 20E_R$ ) for very tight anisotropic confinement. This is a similar regime as the one studied in Ref. [SCMM14], where a completely incompressible chain was studied. In particular, we found that the linear to zigzag transition was lost for realistic values of polar molecules for deep optical lattices.

In the following, we present the ground state of multiple bands close to the transition using TEBD for larger systems and shallower optical lattices where we expect that the quantum fluctuations will have an influence on the transition. The results presented here are, as in section 6.4, for the polar molecule  $^{85}\text{Rb-}^{133}\text{Cs}$ . The system is tightly confined in a plane with  $\sigma_z = 0.013a$  and the analysis of section 6.4 expects to find a Mott insulator for tight confinements  $\omega_y$ . We then study the calculate the ground state for various frequencies  $\omega_y$  down to the regime, where a single dipolar chain is not classically stable.

Figure 6.14 shows the zigzag order parameter  $\xi$  for different numbers calculated by TEBD for a shallow optical lattice of  $V_L = 6E_R$ . For 4 particles the TEBD gives the same result as the exact diagonalization within numerical accuracy. For larger numbers of particles, the ground state can only be calculated using TEBD, as the memory and runtime requirement is too large for the exact diagonalization. For particle numbers there is a clear increase in the structure factor  $\xi$  that indicates zigzag order for decreasing trap frequency. Interestingly, this increase starts at trap frequencies that are larger than the classical critical trap frequency. For all values of the trap frequency  $\omega_y$  value of  $\xi$  increases with increasing particle number, showing no clear transition between a linear and

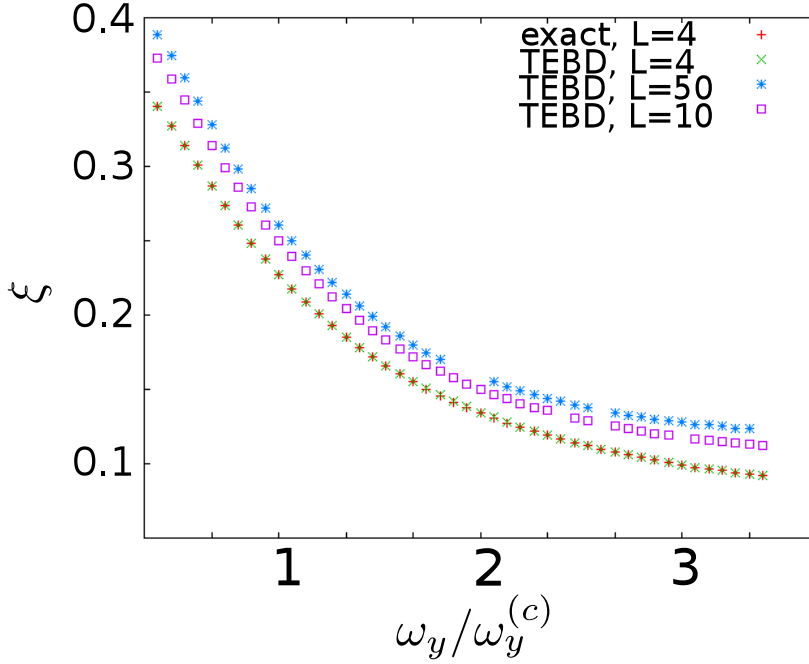


**Figure 6.14** – The structure factor  $\xi$  indicating zigzag order for  $\sigma_z = 0.013 a$  at an optical lattice depth of  $V_L = 6E_R$  for various numbers of particles.

a zigzag phase. This parameter range lies at the border of the validity of our analysis with a basis of three internal states, as the average occupation in the third orbital is here about 6%.

For slightly deeper optical lattice of  $V_L = 15E_R$  this behaviour changes significantly, here the occupation is less than 0.1%. Figure 6.15 shows the order parameter  $\xi$ . In the linear phase, the structure factor  $\xi$  decreases with increasing particle number, while it increases at small trap frequencies  $\omega_y$  with the particle number. Furthermore,  $\xi$  shows a clear increase that appears for trap frequencies that are smaller than the classical critical frequency. The curves of  $\xi$  for different particle numbers intersect at the same point around  $\omega_y = 0.5\omega_y^{(c)}$ . A more detailed study with larger particle numbers is necessary to reveal whether a finite size scaling similar to the one in [SCMM14] can be done in this regime.

## 6.6 Conclusion and Outlook

We have analyzed the ground state of dipolar bosons in a quasi-one dimensional optical lattice near the regime where the classical linear to zigzag instability is found. We have introduced a multi-mode extended Bose-Hubbard model that is valid in the tight binding limit and is based on the low energy classical theory of the structural instability. In the linear phase our model reduces to a single

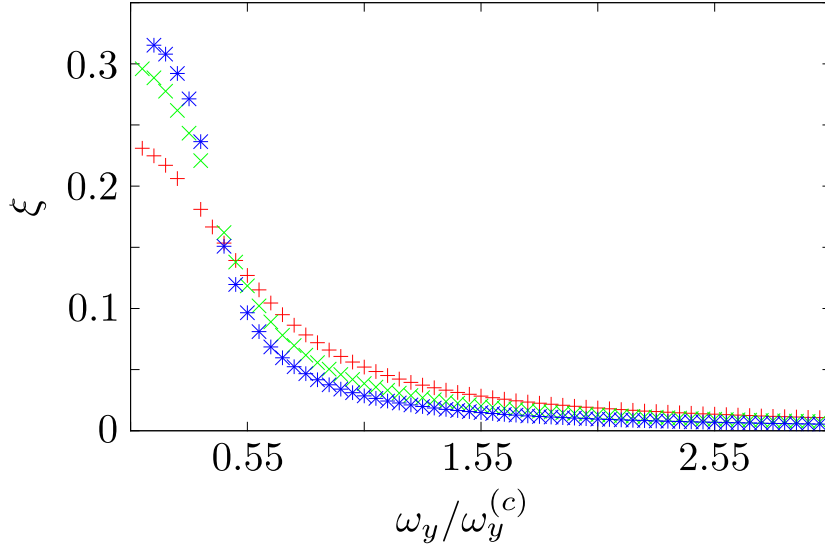


**Figure 6.15** – The structure factor  $\xi$  indicating zigzag order for  $\sigma_z = 0.013a$  at an optical lattice depth of  $V_L = 15E_R$  for 4 particles (red points), 10 particles (green) 20 particles (blue points).

band Hamiltonian and, using exact diagonalization, we find the same phases as the ones reported in [SDH<sup>+</sup>12]. When the trap frequency is large, deep in the tight-binding limit and for experimentally achievable dipole moments our analysis shows that it is sufficient to take only the three lowest bands into account. For realistic values of polar molecules, we explored the phase diagram of the single band Hamiltonian using exact diagonalization.

By setting the pair and density assisted tunneling terms to zero, a PIMC algorithm was used to explore the ground states for a larger number of particles, where we found the Haldane that was also seen in Refs. [DTBA06, BSRG13]. The PIMC has two shortcomings: a) for large tunneling and small on-site interaction the convergence is too slow, and b) Due to a sign problem, the full Hamiltonian cannot be studied with this algorithm.

For these reasons, a TEBD algorithm was used to solve the full Hamiltonian, where the sign problem does not play a role. We studied the multiband model in the regime of tight confinement along  $z$  for various strength of the optical lattice for commensurate fillings. For deep optical lattices the motion along the  $x$  axis is practically decoupled, and there is no tunneling between different lattice sites. For realistic values of experiments the effective Planck constant  $g$  is large, effectively destroying the linear to zigzag transition (see Fig. 6.3). On the other hand, in weak optical lattices the zigzag correlation increases with decreasing transverse confinement significantly, but there is no clear transition visible. In this regime the tunneling between different sites will lead to non-

negligible population in the third bands and a more detailed analysis with more internal states is necessary here.

However, for an intermediate optical lattice strength of  $V_L = 15E_R$ , the linear to zigzag transition is visible and appears at smaller values of the critical frequency, expanding the linear phase. Further studies can focus on this intermediate regime, where it appears that the the tunneling along  $x$  acts in a similar way as the quantum fluctuations in incompressible ion chains [SCMM14], which increase the unordered phase. By taking into account a larger local basis, future works could be able to see whether the linear to zigzag transition also survives for weak optical lattices.

As we have seen, the Bose-Hubbard parameters depend strongly on the confinement along  $z$ , and in this work the multi-band model was always studied for parameters where the system is compressible in the linear chain. A natural extension of this work is the exploration of the system for smaller  $\sigma_z$  near one of the other phases of the single band model, such as superfluidity or the Haldane insulator. According to a long-wavelength analysis [AMPC10] the pair tunneling and density assisted tunneling terms are irrelevant for the criticality of the Haldane insulator, and our full multi-mode model might also display a Haldane phase.

The optical lattice in our model was used to make the dipolar chain incompressible, and reduce the coupling between axial and transverse modes. In the classical case, we saw that this coupling leads to a modification of the critical behaviour. Future studies could extend our analysis to weak lattices and explore whether the nearly second order character survives the inclusion of quantum effects.



# CHAPTER 7

---

## Conclusions

---

In this thesis we theoretically discussed several situations in which the interplay of quantum fluctuations, interactions, and dimensionality is essential in determining the state of ultracold bosonic atoms. We focused on quasi-one dimensional systems, which can be realized by means of a tight atomic wave guide, and considered the effect of a one-dimensional optical lattice along the wave guide. In the first part we analyzed the out-of equilibrium dynamics of hard-core bosons, forming initially a gapped insulating state, when the optical lattice is suddenly switched off. We derived an exact solution valid in the limit of infinite interactions and in the thermodynamic limit we showed that the system reaches a non-equilibrium steady-state characterized by the absence of quasi-long-range order that is approached in time with a power law.

We then analyzed the quantum phases of ultracold dipolar bosons in the same geometry, when the dipoles are aligned perpendicularly to the wave guide and the transverse confinement is relaxed. Classically, we showed that the structural transition from a linear array to a zigzag structure is a first-order phase transition. The quantum mechanical state is analyzed in an optical lattice and is described by a multi-mode Bose-Hubbard model, which we derive in detail and which reduces in the one-dimensional limit to an extended Bose-Hubbard model. We then analyzed the phase diagram by means of exact diagonalization, and found signatures of a rich phase diagram where the onset of long-range zigzag diagonal order can be observed. We then set the stage for a path-integral and a TEBD based numerical simulations, which shall give a quantitative prediction of the complex phase diagram. The numerical analysis based on these methods is underway. Among the specific predictions on the phase diagram as a function of the various physical parameters, we are specifically interested in verifying whether an incompressible Mott-insulator state of dipolar bosons in one dimension undergoes a structural instability to a zigzag structure described by quantum Ising model in transverse fields. This is expected on the basis of studies performed on ion chains [MML07, SMF11, SDCC<sup>+</sup>13], where due to the Coulomb interaction the chain is incompressible and the classical transition is

of second order. The other question is then what is the nature of the transition if the bosons are in a superfluid state? More generally, how do quantum fluctuations affect the crossover between one- and two-dimensional geometries?

Experimentally, ultracold dipolar gases with these geometries can be realized with molecules and Rydberg atoms [MP14]. Analogous dynamics are also expected in systems of ultracold atoms in driven optical resonators, where multiple-photon scattering induces the formation of long-range order also in one dimension [BGBE10]. The interplay between long-range and contact interaction is here at the basis of a rich phase diagram, including charge density wave, Mott insulator, superfluid and supersolid phases [LHD<sup>+</sup>16].

Our analysis sets also the basis for a systematic study of quenches across the linear-zigzag phase transition. Of particular interest is to understand how interaction-induced pair superfluidity - giving rise to non-trivial off-diagonal order- and the classical part of the dipolar interaction - giving rise to structural defects - affect the onset of equilibrium.

# APPENDIX A

---

## The 2d effective potential

---

In this Appendix the effective dipole-dipole interaction in two dimensions is calculated, which is needed for the numerical calculation of the Bose-Hubbard coefficients. In general one needs to determine integrals of the form

$$V_{j,k,l,m} = \int dx dy \int dx' dy' A_{j,l}(x, y) I(\mathbf{r} - \mathbf{r}') B_{lm}(x, y), \quad (\text{A.1})$$

where  $I$  is the effective dipole-dipole interaction and the  $z$ -direction has been integrated out. This integral can be calculated using a Bloch expansion or a convolution method [WC13]. We will choose the latter and write the integral as

$$V_{j,k,l,m} = \int dx dy A(r) \mathcal{F}_{k \rightarrow r}^{-1} [\mathcal{F}_{r \rightarrow k} [I(r)] \mathcal{F}_{r \rightarrow k} [B(r)]], \quad (\text{A.2})$$

where  $\mathcal{F}$  is the Fourier transform and we dropped the indices for convenience. This allows one to calculate the integral by computing a 2d Fourier transform and a 2d integration instead of integrating a four dimensional integral in real space, which this saves computing time, and allows one to use a finer grid of discretization.

We start by integrating out the center of mass in

$$V_{2d}(x, y) = \int dz_1 dz_2 \theta_0^2(z_1) \theta_0^2(z_2) U_d(\mathbf{r}_1 - \mathbf{r}_2), \quad (\text{A.3})$$

to arrive at

$$V_{2D}(x, y) = \int dz \frac{1}{\sqrt{2\pi\sigma_z}} e^{-z^2/(2\sigma^2)} U_d(x, y, z). \quad (\text{A.4})$$

Going into Fourier space gives

$$V_{2D}(x, y) = \int dz \frac{1}{2\pi} \int dk'_z \tilde{A}(k'_z) e^{ik'_z z} \frac{1}{(2\pi)^3} \int d^3k \tilde{U}(\mathbf{k}) e^{i\mathbf{k}\cdot\mathbf{r}} \quad (\text{A.5})$$

$$= \int dk_x dk_y e^{i(k_x x + k_y y)} \frac{1}{(2\pi)^3} \int dk_z \tilde{A}(-k_z) \tilde{U}(k_x, k_y, k_z) \quad (\text{A.6})$$

$$= \frac{1}{(2\pi)^2} \int dk_x dk_y e^{i(k_x x + k_y y)} \tilde{V}_{2D}(k_x, k_y), \quad (\text{A.7})$$

where

$$\tilde{A}(k_z) = e^{-k_z^2 \sigma_z^2 / 2}, \quad (\text{A.8})$$

and

$$\tilde{U}(\mathbf{k}) = \int d^3r e^{-i\mathbf{k}\cdot\mathbf{r}} U_d(\mathbf{r}) = C_D \frac{4\pi}{3} \left( 3 \frac{k_z^2}{k_x^2 + k_y^2 + k_z^2} - 1 \right). \quad (\text{A.9})$$

This integral can be calculated analytically, and the Fourier transform of the 2d effective potential is

$$\tilde{V}_{2D}(q = \sqrt{k_x^2 + k_y^2}) = \frac{1}{2\pi} \int dk_z \tilde{A}(k_z) \tilde{U}(k_x, k_y, k_z) \quad (\text{A.10})$$

$$= \frac{C_D 2\pi}{\sigma_z} \left[ \frac{2}{3} \sqrt{\frac{2}{\pi}} - q \sigma_z \operatorname{erfcx}(q \sigma_z / \sqrt{2}) \right], \quad (\text{A.11})$$

where  $\operatorname{erfcx}(x)$  is the scaled complementary error function<sup>1</sup>. This expression is identical to the one in Ref. [BD12], except for the constant term, which modifies the on-site interaction [DCR13]

In real space, the effective integral of the interaction potential is:

$$V_{2d}(x, y) = p^2 \left[ \frac{1}{\sqrt{8\pi}\sigma_z^5} e^{\frac{\rho^2}{4\sigma_z^2}} \left( (\rho^2 + 2\sigma_z^2) K_0 \left( \frac{\rho^2}{4\sigma_z^2} \right) - \rho^2 K_1 \left( \frac{\rho^2}{4\sigma_z^2} \right) \right) - \frac{\sqrt{2\pi}}{3\sigma_z} \delta(x, y) \right].$$

---

<sup>1</sup> $\operatorname{erfcx}(x) = e^{x^2} \operatorname{erfc}(x)$

# APPENDIX B

---

## Path Integral Monte Carlo

---

In this appendix the method of Path-Integral Monte Carlo method (PIMC) is described, which was introduced by Batrouni et al. [BS92], and also was successfully used to study the Bose-Hubbard Hamiltonian with long-range interactions[HWP<sup>+</sup>13]. We will then present an overview of the results that we obtained using the PIMC, in particular the occurrence of a Haldane insulating phase. Finally, we will discuss why the PIMC cannot be extended to treat the problem of a multi-band extended Bose-Hubbard Hamiltonian. This will bring us to resort to exact diagonalization in section 6.5.

In general, Monte-Carlo methods allow one to approximate integrals,

$$I = \int_a^b dx f(x)p(x),$$

where we have written the integral as a product of two functions  $f$  and  $p$ . One can approximate this integral by the discrete sum

$$I \approx \sum_{j=1}^L f(x_j)p(x_j), \tag{B.1}$$

where  $x_j$  are uniformly chosen random points in  $[a, b]$ . With increasing number of points  $L$ , the sum converges to the value of the integral as  $1/\sqrt{N}$ .

If  $p(x)$  is positive and  $\int_a^b p(x) = 1$ , one can interpret the function  $p$  as a probability. Instead of choosing uniformly distributed random values, we will chose  $L$  points  $x_p$  generated with the probability  $p(x)$ . Then, the integral approximation is simply

$$I \approx \sum_{p=1}^L f(x_p). \tag{B.2}$$

This makes the convergence towards the exact value of the integral faster, especially if the probability distribution  $p(x)$  is sharply peaked.

A common strategy to generate points according to the probability  $p(x)$  is the Metropolis-Hastings algorithm. From a random configuration  $x_i$ , new trial configurations  $x'$  are randomly chosen according to a distribution  $g(x', x)$ . The trial state is accepted according to [HAS70]

$$A(x_o, x') = \min \left( \frac{p(x')g(x_o, x')}{p(x_o)g(x', x_o)} \right). \quad (\text{B.3})$$

If new configuration is accepted, the system transitions to the new point, if not it remains in the same state. States that are generated according to this algorithm are distributed randomly with  $p(x)$ .

In our case, we need to calculate the expectation values of operators  $O$ , that in a canonical ensemble are given by

$$\langle O \rangle = \text{Tr} (O e^{-\beta H}) / Z, \quad (\text{B.4})$$

where  $Z$  is the partition function and  $\beta$  the inverse temperature.

The trace can be written as a path integral

$$\langle O \rangle = \frac{\int Dx O(x) e^{-\beta H}}{\int Dx e^{-\beta H}}. \quad (\text{B.5})$$

If we set  $T_0^x = 0 = P_0^x$  one can split the lattice Hamiltonian (6.12) into an even and an odd part

$$H = H_{\text{even}} + H_{\text{odd}}, \quad (\text{B.6})$$

with  $H_{\text{even}} = \sum_j H_{j,j+1}$ , and  $H_{\text{odd}} = H_{j+1,j+2}$ , and

$$H_{j,j+1} = K_{j,j+1} + \frac{1}{2}(P_j + P_{j+1}) + P_{j,j+1}, \quad (\text{B.7})$$

where we further decomposed the Hamiltonian into parts that are diagonal in the Fock number representation and those which are not,

$$K_{j,j+1} = J^x (a_j^\dagger a_{j+1} + a_j a_{j+1}^\dagger), \quad (\text{B.8})$$

$$P_j = U n_j (n_j - 1), \quad (\text{B.9})$$

$$P_{j,j+1} = V n_j n_{j+1}. \quad (\text{B.10})$$

In the following, we define  $\tau = \beta/m$  and write the partition function as

$$Z = \lim_{m \rightarrow \infty} Z_m, \quad (\text{B.11})$$

$$Z_m = \sum_{\Psi_1, \dots, \Psi_{2m}} \langle \Psi_1 | e^{-\tau H_{\text{even}}} | \Psi_2 \rangle \cdot \dots \cdot \langle \Psi_{2m-1} | e^{-\tau H_{\text{even}}} | \Psi_{2m} \rangle \langle \Psi_{2m} | e^{-\tau H_{\text{odd}}} | \Psi_1 \rangle, \quad (\text{B.12})$$

where  $|\Psi\rangle$  is a complete set of occupation number states. Now the expectation value of an operator that is diagonal in the basis  $\Psi$  can be written as

$$\langle O \rangle = \sum_{\Psi_1, \dots, \Psi_{2m}} O(\Psi_1) P(\Psi_1, \dots, \Psi_{2m}), \quad (\text{B.13})$$

where

$$P(\Psi_1, \dots, \Psi_{2m}) = \frac{\prod_{l=0}^{m-1} \langle \Psi_{2l+1} | e^{H_{\text{even}}} | \Psi_{2l+2} \rangle \langle \Psi_{2l+2} | e^{H_{\text{odd}}} | \Psi_{2l+3} \rangle}{\sum_{\Psi_1, \dots, \Psi_{2m}} \prod_{l=0}^{m-1} \langle \Psi_{2l+1} | e^{H_{\text{even}}} | \Psi_{2l+2} \rangle \langle \Psi_{2l+2} | e^{H_{\text{odd}}} | \Psi_{2l+3} \rangle} \quad (\text{B.14})$$

is the weight of the configuration and  $\Psi_1 = \Psi_{2m+1}$ . If  $P(\Psi_1, \dots, \Psi_{2m}) > 0$  we can interpret it as the probability of the configuration.

The numerical algorithm will generate configurations with the probability that is given by the weight of the configuration. The expectation value of an operator is then simply calculated by averaging over all generated configurations.

Every term  $\langle \Psi_m | e^{\beta H} | \Psi_{m+1} \rangle$  consists of a product of independent two-site problems. For the numerical algorithm, we first need to calculate all the matrix elements of the two-site problems, where we used the Fock basis as the basis of the Hilbert space. The matrix elements that have to be computed are

$$M = \langle n_j n_{j+1} | \exp(-\tau H_{j,j+1}) | m_j m_{j+1} \rangle. \quad (\text{B.15})$$

Here,  $(n)$  denotes the occupation numbers at the bottom of a squares, and  $(m)$  the occupation numbers at the top of a squares. For small values of  $\tau$  we can use the Trotter decomposition to write the Matrix elements as

$$M = \langle n_j, n_{j+1} | e^{-\frac{\tau}{2}P} (1 - \tau K) e^{-\frac{\tau}{2}P} | m_j, m_{j+1} \rangle, \quad (\text{B.16})$$

where we divided the contribution of the potential energy into two equal parts, one for the bottom and one for the top of the square.

To sample the phase space we start in a random configuration and then change it by local moves in a way that ensures that the probability of the generation of new configurations is given by eq. (B.14). In addition, we add global updates, that insert and delete straight world lines to improve convergence. If the simulation was done in a grand-canonical ensemble, these global moves would be necessary, but in our case they are only optional.

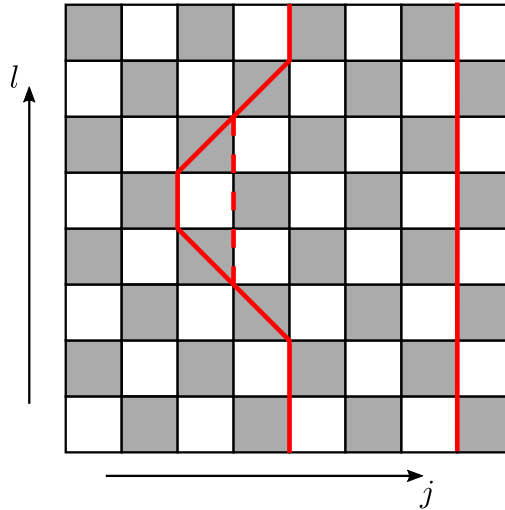


**Figure B.1** – Example configuration of two bosons in an optical lattice of eight sites. The dashed line shows a possible local update.

The partition function is given by the product over all “squares”, which we can imagine being ordered in a two dimensional lattice, see Fig. B.1. Because we divided the Hamiltonian into a sum over even and odd contributions, at times  $2l$  only the pairs  $j = (1, 2), (3, 4), \dots$  interact and at times  $2l + 1$  only the pairs  $(N, 1), (2, 3), \dots$  interact. This means that in Fig. B.1 the particle number in each shaded cube must be conserved, and the acceptance probability (B.3) is easy to calculate as a few squares of the hole system change.

All quantities that are diagonal in the Fock basis are easy to measure using this world line algorithm. For example the density is averaged over all slices

$$\langle n_j \rangle = \frac{1}{2L} \sum_{l=0}^{2L-1} n(j, l). \quad (\text{B.17})$$

Quantities that are not diagonal in the particle number representation are more challenging to evaluate. The superfluid density is therefore usually calculated in the world line algorithm over the winding number  $W$ , which is the number of world lines that are wound along the lattice. The mean square of the winding number is related to the superfluid density by

$$\rho_s = N \frac{\langle W^2 \rangle}{2\beta t_x}. \quad (\text{B.18})$$

But because the algorithm works in the canonical ensemble, the number of particles is conserved and the winding number is constraint to  $W = 0$ , but it

still can be computed via the pseudo-current,

$$j(l) = \frac{1}{2} \sum_{j=0}^{N-1} [n(j, l) - n(j+1, l)n(j, l+1) + n(j+1, l+1)], \quad (\text{B.19})$$

that measures at a given time slices  $l$  the number of particles moving right minus the number of particles moving left. In the simulation, one measures the pseudo-current correlator

$$C_j(l) = \langle j(l)j(0) \rangle. \quad (\text{B.20})$$

One can show that the Fourier transform of the pseudo-current correlator,  $C_j(\omega) = \sum_l e^{il\omega n} C_j(l)$ , is related to the winding number, via [PC87]

$$\langle W^2 \rangle = C_j(0) \frac{2L}{N^2}. \quad (\text{B.21})$$

While the pseudo-current correlator is restricted to zero at  $\omega = 0$ , one can estimate its value via the extrapolation  $\omega \rightarrow 0$ .

### The full extended Bose-Hubbard

The full single band Hamiltonian (6.12), cannot be studied with the PIMC for realistic parameter ranges. If one decomposes the lattice Hamiltonian in a similar way as before, one finds two additional kinetic energy terms in the decomposition (B.7):

$$K_T = T_0^x \sum_j \left( a_j^\dagger (n_j + n_{j+1}) a_{j+1} + \text{h.c.} \right), \quad (\text{B.22})$$

$$K_P = P_0^x \sum_j \left( a_j^\dagger a_j^\dagger a_{j+1} a_{j+1} + \text{h.c.} \right). \quad (\text{B.23})$$

The matrix elements of the Trotter decomposition (B.16) give

$$M = \langle n_j, n_{j+1} | e^{-\frac{\tau}{2}P} (1 - \tau(K + K_T + K_P)) e^{-\frac{\tau}{2}P} | m_j, m_{j+1} \rangle. \quad (\text{B.24})$$

Here we can see that if  $T = P = 0$ , all the matrix elements are positive, as  $t_x < 0$ , which allows us to interpret the above decomposition as probability for the Metropolis sampling. But as  $T > 0$  for dipolar gases in optical lattices, the matrix elements are not strictly positive, if we include pair tunneling and density assisted tunneling. This means that we cannot interpret the matrix element as the weight of a configuration. Therefore, the PIMC can only be used in regimes where  $T$  and  $P$  can be neglected.



# APPENDIX C

---

## Time Evolving Block Decimation

---

This appendix gives information about the TEBD [Vid04, Vid03] algorithm that used in 6.5. The TEBD algorithm was provided by Ferdinand Tschirsich, Pietro Silvi and Simone Montangero from the Institute for Complex Quantum Systems at the University of Ulm.

For the algorithm to work, the Hilbert space must be written as a tensor product of local Hilbert spaces of finite dimension. The system Hamiltonian must then be a sum of at most neighbor interactions between the local Hilbert spaces with open boundary conditions. The full Hamiltonian of dipoles in optical lattices (6.8) has continuous quantum variables and is therefore not suitable to be calculated using TEBD. However, the Bose-Hubbard Hamiltonian (6.11) can be used, provided that the local Hilbert space is cut to a few particles per lattice site, which is correct for sufficiently strong interactions.

It works by applying the imaginary time evolution operator  $U = \exp(-dt H)$  to a (random) initial product state for small time steps  $dt$  via Trotter decomposition to the MPS representation of the quantum state.

In particular, we cut the local Hamiltonian such that:

- the number of orbitals is restricted  $m \leq M$ , where  $M$  is the maximum occupied band,
- the maximum number of particles per site is restricted,  $n_j = \sum_m n_{j,m} \leq C$ , where  $n_{j,m}$  is the particle number at site  $j$  in band  $m$ ,
- the maximum number of particles per orbital is smaller than a given value,  $n_{j,m} \leq D$ .

When multiple bands are simulated, we typically chose  $M = 3$ ,  $C = 3$  and  $D = 2$ , which gives a total of 17 possible local states  $|\Psi_q\rangle$  with  $q = 0, 1, \dots, 16$ . Via tensor product states of the single-site basis states  $|\Psi_q\rangle_1 \otimes |\Psi_q\rangle_2 \otimes \dots \otimes |\Psi_q\rangle_L$  the resulting many-body computational state is constructed. For the simulation all operators in the Hamiltonian, as well as all measurement operators must be written in the reduced local basis.

While we used the particle number per site and band to represent the ground state of the system for the exact diagonalization and for the PIMC, it is best to use a basis that uses the largest local symmetry group under which our Hamiltonian is invariant for the TEBD. By specifying local symmetries of the Hamiltonian and by using a symmetry-aware representation of the Hamiltonian, the computational cost and memory requirements can be substantially reduced. The reason for this is that if a Hamiltonian commutes with an Abelian group of operations, then the Hilbert space can be decomposed into dynamically uncoupled sectors, which are invariant under the action of the Hamiltonian.

Our Hamiltonian has two symmetries. The first is the number of particles,  $[H, N] = 0$ . The second is the parity: the structure of Bose-Hubbard coefficients in eq. (6.11) is such that the number of particles in even and odd orbitals is conserved. This is because we the Bose-Hubbard Hamiltonian was found by expanding the wave function as  $\Psi(\mathbf{r}) \sim \sum_{j,m} w_j(x)\phi_m(y)$ , where  $\phi_m(y)$  are the eigenstates of the local Hamiltonian (6.7). As this local Hamiltonian is invariant under sign change,  $y \rightarrow -y$ , the parity is also conserved for the global Hamiltonian. The additional symmetries are encoded within this local basis.

---

## Bibliography

---

- [ABKL07] G. E. Astrakharchik, J. Boronat, I. L. Kurbakov, and Yu. E. Lozovik. Quantum phase transition in a two-dimensional system of dipoles. *Phys. Rev. Lett.*, 98:060405, Feb 2007.
- [ACMB09] G E Astrakharchik, Gabriele De Chiara, Giovanna Morigi, and Jordi Boronat. Thermal and quantum fluctuations in chains of ultracold polar molecules. *Journal of Physics B: Atomic, Molecular and Optical Physics*, 42(15):154026, 2009.
- [AM76] N.W. Ashcroft and N.D. Mermin. *Solid State Physics*. Saunders College, Philadelphia, 1976.
- [AMDCB08] G. E. Astrakharchik, Giovanna Morigi, Gabriele De Chiara, and J. Boronat. Ground state of low-dimensional dipolar gases: Linear and zigzag chains. *Phys. Rev. A*, 78:063622, Dec 2008.
- [AMPC10] L Amico, G Mazzearella, S Pasini, and F S Cataliotti. Hidden order in bosonic gases confined in one-dimensional optical lattices. *New Journal of Physics*, 12(1):013002, 2010.
- [AS64] M. Abramowitz and I.A. Stegun. *Handbook of Mathematical Functions: With Formulas, Graphs, and Mathematical Tables*. Applied mathematics series. Dover Publications, 1964.
- [BBZ03] H. P. Büchler, G. Blatter, and W. Zwerger. Commensurate-incommensurate transition of cold atoms in an optical lattice. *Phys. Rev. Lett.*, 90:130401, Apr 2003.
- [BD12] Mehrtash Babadi and Eugene Demler. Collective excitations of quasi-two-dimensional trapped dipolar fermions: Transition from collisionless to hydrodynamic regime. *Phys. Rev. A*, 86:063638, Dec 2012.
- [BDL<sup>+</sup>07] H. P. Büchler, E. Demler, M. Lukin, A. Micheli, N. Prokof'ev, G. Pupillo, and P. Zoller. Strongly correlated 2d quantum phases with cold polar molecules: Controlling the shape of the interaction potential. *Phys. Rev. Lett.*, 98:060404, Feb 2007.

- [BDZ08] Immanuel Bloch, Jean Dalibard, and Wilhelm Zwerger. Many-body physics with ultracold gases. *Rev. Mod. Phys.*, 80:885–964, Jul 2008.
- [BGBE10] Kristian Baumann, Christine Guerlin, Ferdinand Brennecke, and Tilman Esslinger. Dicke quantum phase transition with a superfluid gas in an optical cavity. *Nature*, 464(7293):1301–1306, April 2010.
- [BKW92] G. Birkl, S. Kassner, and H. Walther. Multiple-shell structures of laser-cooled 24mg+ ions in a quadrupole storage ring. *Nature*, 357(6376):310–313, May 1992.
- [BRSG14] G. G. Batrouni, V. G. Rousseau, R. T. Scalettar, and B. Grémaud. Competing phases, phase separation, and coexistence in the extended one-dimensional bosonic hubbard model. *Phys. Rev. B*, 90:205123, Nov 2014.
- [BS92] Ghassan George Batrouni and Richard T. Scalettar. World-line quantum monte carlo algorithm for a one-dimensional bose model. *Phys. Rev. B*, 46:9051–9062, Oct 1992.
- [BSRG13] G. G. Batrouni, R. T. Scalettar, V. G. Rousseau, and B. Grémaud. Competing supersolid and haldane insulator phases in the extended one-dimensional bosonic hubbard model. *Phys. Rev. Lett.*, 110:265303, Jun 2013.
- [Caz06] M. A. Cazalilla. Effect of suddenly turning on interactions in the luttinger model. *Phys. Rev. Lett.*, 97:156403, Oct 2006.
- [CC06] Pasquale Calabrese and John Cardy. Time dependence of correlation functions following a quantum quench. *Phys. Rev. Lett.*, 96:136801, Apr 2006.
- [CCM13] Florian Cartarius, Cecilia Cormick, and Giovanna Morigi. Stability and dynamics of ion rings in linear multipole traps. *Phys. Rev. A*, 87:013425, Jan 2013.
- [CK12] Jean-Sébastien Caux and Robert M. Konik. Constructing the generalized gibbs ensemble after a quantum quench. *Phys. Rev. Lett.*, 109:175301, Oct 2012.
- [CLR00] Lincoln D Carr, Mary Ann Leung, and William P Reinhardt. Dynamics of the bose-einstein condensate: quasi-one-dimension and beyond. *Journal of Physics B: Atomic, Molecular and Optical Physics*, 33(19):3983, 2000.

- [CODPC07] R. Citro, E. Orignac, S. De Palo, and M. L. Chiofalo. Evidence of luttinger-liquid behavior in one-dimensional dipolar quantum gases. *Phys. Rev. A*, 75:051602, May 2007.
- [CSC13] Mario Collura, Spyros Sotiriadis, and Pasquale Calabrese. Equilibration of a tonks-girardeau gas following a trap release. *Phys. Rev. Lett.*, 110:245301, Jun 2013.
- [DCR13] F. Deuretzbacher, J. C. Cremon, and S. M. Reimann. Erratum: Ground-state properties of few dipolar bosons in a quasi-one-dimensional harmonic trap [phys. rev. a **81**, 063616 (2010)]. *Phys. Rev. A*, 87:039903, Mar 2013.
- [DGR<sup>+</sup>08] J. Deiglmayr, A. Grochola, M. Repp, K. Mörtilbauer, C. Glück, J. Lange, O. Dulieu, R. Wester, and M. Weidemüller. Formation of ultracold polar molecules in the rovibrational ground state. *Phys. Rev. Lett.*, 101:133004, Sep 2008.
- [dNR89] Marcel den Nijs and Koos Rommelse. Preroughening transitions in crystal surfaces and valence-bond phases in quantum spin chains. *Phys. Rev. B*, 40:4709–4734, Sep 1989.
- [DO99] Daniel H. E. Dubin and T. M. O’Neil. Trapped nonneutral plasmas, liquids, and crystals (the thermal equilibrium states). *Rev. Mod. Phys.*, 71:87–172, Jan 1999.
- [DTBA06] Emanuele G. Dalla Torre, Erez Berg, and Ehud Altman. Hidden order in 1d bose insulators. *Phys. Rev. Lett.*, 97:260401, Dec 2006.
- [EFG<sup>+</sup>05] Fabian H. L. Essler, Holger Frahm, Frank Göhmann, Andreas Klümper, and Vladimir E. Korepin. *The One-Dimensional Hubbard Model*. Cambridge University Press, 2005. Cambridge Books Online.
- [FDCCM08] Shmuel Fishman, Gabriele De Chiara, Tommaso Calarco, and Giovanna Morigi. Structural phase transitions in low-dimensional ion crystals. *Phys. Rev. B*, 77:064111, Feb 2008.
- [FR66] Michael E. Fisher and David Ruelle. The stability of many-particle systems. *Journal of Mathematical Physics*, 7(2):260–270, 1966.
- [FSG<sup>+</sup>08] A. Friedenauer, H. Schmitz, J. T. Glueckert, D. Porras, and T. Schaetz. Simulating a quantum magnet with trapped ions. *Nat Phys*, 4(10):757–761, October 2008.

- [GA15] Garry Goldstein and Natan Andrei. Equilibration and generalized gibbs ensemble for hard wall boundary conditions. *Phys. Rev. B*, 92:155103, Oct 2015.
- [Gir60] M. Girardeau. Relationship between systems of impenetrable bosons and fermions in one dimension. *Journal of Mathematical Physics*, 1(6):516–523, 1960.
- [GMM<sup>+</sup>05] S. Gupta, K. W. Murch, K. L. Moore, T. P. Purdy, and D. M. Stamper-Kurn. Bose-einstein condensation in a circular waveguide. *Phys. Rev. Lett.*, 95:143201, Sep 2005.
- [GNT04] Alexander O Gogolin, Alexander A Nersesyan, and Alexei M Tsvelik. *Bosonization and strongly correlated systems*. Cambridge University Press, 2004.
- [GSL02] K. Góral, L. Santos, and M. Lewenstein. Quantum phases of dipolar bosons in optical lattices. *Phys. Rev. Lett.*, 88:170406, Apr 2002.
- [GW00] M. D. Girardeau and E. M. Wright. Breakdown of time-dependent mean-field theory for a one-dimensional condensate of impenetrable bosons. *Phys. Rev. Lett.*, 84:5239–5242, Jun 2000.
- [HAS70] W. K. HASTINGS. Monte carlo sampling methods using markov chains and their applications. *Biometrika*, 57(1):97–109, 1970.
- [HHM<sup>+</sup>10] E. Haller, R. Hart, M. J. Mark, J. G. Danzl, L. Reichsöllner, M. Gustavsson, M. Dalmonte, G. Pupillo, and H.-C. Nägerl. Pinning quantum phase transition for a Luttinger liquid of strongly interacting bosons. *Nature*, 466:597–600, July 2010.
- [HNSF08] W H Heathcote, E Nugent, B T Sheard, and C J Foot. A ring trap for ultracold atoms in an rf-dressed state. *New Journal of Physics*, 10(4):043012, 2008.
- [HRMB09] K Henderson, C Ryu, C MacCormick, and M G Boshier. Experimental demonstration of painting arbitrary and dynamic potentials for bose–einstein condensates. *New Journal of Physics*, 11(4):043030, 2009.
- [HWP<sup>+</sup>13] Hessam Habibian, André Winter, Simone Paganelli, Heiko Rieger, and Giovanna Morigi. Bose-glass phases of ultracold atoms due to cavity backaction. *Phys. Rev. Lett.*, 110:075304, Feb 2013.

- [IC09] A. Iucci and M. A. Cazalilla. Quantum quench dynamics of the luttinger model. *Phys. Rev. A*, 80:063619, Dec 2009.
- [Imr74] Yoseph Imry. Tricritical points in compressible magnetic systems. *Phys. Rev. Lett.*, 33:1304–1307, Nov 1974.
- [JBC<sup>+</sup>98] D. Jaksch, C. Bruder, J. I. Cirac, C. W. Gardiner, and P. Zoller. Cold bosonic atoms in optical lattices. *Phys. Rev. Lett.*, 81:3108–3111, Oct 1998.
- [JFB<sup>+</sup>12] Thibaut Jacqmin, Bess Fang, Tarik Berrada, Tommaso Roscilde, and Isabelle Bouchoule. Momentum distribution of one-dimensional bose gases at the quasicondensation crossover: Theoretical and experimental investigation. *Phys. Rev. A*, 86:043626, Oct 2012.
- [KCK<sup>+</sup>10] K. Kim, M.-S. Chang, S. Korenblit, R. Islam, E. E. Edwards, J. K. Freericks, G.-D. Lin, L.-M. Duan, and C. Monroe. Quantum simulation of frustrated ising spins with trapped ions. *Nature*, 465(7298):590–593, June 2010.
- [KCU08] Rina Kanamoto, Lincoln D. Carr, and Masahito Ueda. Topological winding and unwinding in metastable bose-einstein condensates. *Phys. Rev. Lett.*, 100:060401, Feb 2008.
- [KLM<sup>+</sup>08] T. Koch, T. Lahaye, J. Metz, B. Frohlich, A. Griesmaier, and T. Pfau. Stabilization of a purely dipolar quantum gas against collapse. *Nat Phys*, 4(3):218–222, March 2008.
- [KPS05] D. L. Kovrizhin, G. Venketeswara Pai, and S. Sinha. Density wave and supersolid phases of correlated bosons in an optical lattice. *EPL (Europhysics Letters)*, 72(2):162, 2005.
- [KT92] Tom Kennedy and Hal Tasaki. Hidden  $z_2 \times z_2$  symmetry breaking in haldane-gap antiferromagnets. *Phys. Rev. B*, 45:304–307, Jan 1992.
- [KWW04] Toshiya Kinoshita, Trevor Wenger, and David S. Weiss. Observation of a one-dimensional tonks-girardeau gas. *Science*, 305(5687):1125–1128, 2004.
- [KWW06] Toshiya Kinoshita, Trevor Wenger, and David S. Weiss. A quantum newton’s cradle. *Nature*, 440(7086):900–903, April 2006.

- [LHD<sup>+</sup>16] Renate Landig, Lorenz Hruby, Nishant Dogra, Manuele Landini, Rafael Mottl, Tobias Donner, and Tilman Esslinger. Quantum phases from competing short- and long-range interactions in an optical lattice. *Nature*, 532(7600):476–479, April 2016.
- [LP69] A. I. Larkin and S. A. Pikin. Phase transitions of the first order but nearly of the second. *Zh. Eksp. Teor. Fiz.*, 29(5):891, 1969. [Sov. Phys. JETP **29**, 891 (1969)].
- [LPR<sup>+</sup>14] Yan Levin, Renato Pakter, Felipe B. Rizzato, Tarcísio N. Teles, and Fernanda P.C. Benetti. Nonequilibrium statistical mechanics of systems with long-range interactions. *Physics Reports*, 535(1):1 – 60, 2014. Nonequilibrium statistical mechanics of systems with long-range interactions.
- [LRB<sup>+</sup>13] H Landa, B Reznik, J Brox, M Mielenz, and T Schaetz. Structure, dynamics and bifurcations of discrete solitons in trapped ion crystals. *New Journal of Physics*, 15(9):093003, 2013.
- [LSA<sup>+</sup>07] Maciej Lewenstein, Anna Sanpera, Veronica Ahufinger, Bogdan Damski, Aditi Sen(De), and Ujjwal Sen. Ultracold atomic gases in optical lattices: mimicking condensed matter physics and beyond. *Advances in Physics*, 56(2):243–379, 2007.
- [LŠBG12] K. Lelas, T. Ševa, H. Buljan, and J. Goold. Pinning quantum phase transition in a tonks-girardeau gas: Diagnostics by ground-state fidelity and the loschmidt echo. *Phys. Rev. A*, 86:033620, Sep 2012.
- [MBS<sup>+</sup>12] Stuart Moulder, Scott Beattie, Robert P. Smith, Naaman Tam-muz, and Zoran Hadzibabic. Quantized supercurrent decay in an annular bose-einstein condensate. *Phys. Rev. A*, 86:013629, Jul 2012.
- [MCL<sup>+</sup>06] Olivier Morizot, Yves Colombe, Vincent Lorent, H el ene Perrin, and Barry M. Garraway. Ring trap for ultracold atoms. *Phys. Rev. A*, 74:023617, Aug 2006.
- [MML07] Julia S. Meyer, K. A. Matveev, and A. I. Larkin. Transition from a one-dimensional to a quasi-one-dimensional state in interacting quantum wires. *Phys. Rev. Lett.*, 98:126404, Mar 2007.
- [MP14] T. Macr i and T. Pohl. Rydberg dressing of atoms in optical lattices. *Phys. Rev. A*, 89:011402, Jan 2014.

- [Ols98] M. Olshanii. Atomic scattering in the presence of an external confinement and a gas of impenetrable bosons. *Phys. Rev. Lett.*, 81:938–941, Aug 1998.
- [PB07] R. Pezer and H. Buljan. Momentum distribution dynamics of a tonks-girardeau gas: Bragg reflections of a quantum many-body wave packet. *Phys. Rev. Lett.*, 98:240403, Jun 2007.
- [PC87] E. L. Pollock and D. M. Ceperley. Path-integral computation of superfluid densities. *Phys. Rev. B*, 36:8343–8352, Dec 1987.
- [PC04] D. Porras and J. I. Cirac. Effective quantum spin systems with trapped ions. *Phys. Rev. Lett.*, 92:207901, May 2004.
- [PHP10] G. Piacente, G. Q. Hai, and F. M. Peeters. Continuous structural transitions in quasi-one-dimensional classical wigner crystals. *Phys. Rev. B*, 81:024108, Jan 2010.
- [PS08] C. J. Pethick and H. Smith. *Bose–Einstein Condensation in Dilute Gases*. Cambridge University Press, second edition, 2008.
- [PWM<sup>+</sup>04] Belen Paredes, Artur Widera, Valentin Murg, Olaf Mandel, Simon Fölling, Ignacio Cirac, Gora V. Shlyapnikov, Theodor W. Hansch, and Immanuel Bloch. Tonks-girardeau gas of ultracold atoms in an optical lattice. *Nature*, 429(6989):277–281, May 2004.
- [PZSK09] Stefan Palzer, Christoph Zipkes, Carlo Sias, and Michael Köhl. Quantum transport through a tonks-girardeau gas. *Phys. Rev. Lett.*, 103:150601, Oct 2009.
- [RAC<sup>+</sup>07] C. Ryu, M. F. Andersen, P. Cladé, Vasant Natarajan, K. Helmerison, and W. D. Phillips. Observation of persistent flow of a bose-einstein condensate in a toroidal trap. *Phys. Rev. Lett.*, 99:260401, Dec 2007.
- [RDTHA12] J. Ruhman, E. G. Dalla Torre, S. D. Huber, and E. Altman. Non-local order in elongated dipolar gases. *Phys. Rev. B*, 85:125121, Mar 2012.
- [RDYO07] Marcos Rigol, Vanja Dunjko, Vladimir Yurovsky, and Maxim Olshanii. Relaxation in a completely integrable many-body quantum system: An *Ab Initio* study of the dynamics of the highly excited states of 1d lattice hard-core bosons. *Phys. Rev. Lett.*, 98:050405, Feb 2007.
- [S<sup>+</sup>] P. Silvi et al.

- [SC14] Spyros Sotiriadis and Pasquale Calabrese. Validity of the gge for quantum quenches from interacting to noninteracting models. *Journal of Statistical Mechanics: Theory and Experiment*, 2014(7):P07024, 2014.
- [Sch86] H. J. Schulz. Phase diagrams and correlation exponents for quantum spin chains of arbitrary spin quantum number. *Phys. Rev. B*, 34:6372–6385, Nov 1986.
- [SCMM14] Pietro Silvi, Tommaso Calarco, Giovanna Morigi, and Simone Montangero. *Ab initio* characterization of the quantum linear-zigzag transition using density matrix renormalization group calculations. *Phys. Rev. B*, 89:094103, Mar 2014.
- [SDCC<sup>+</sup>13] Pietro Silvi, Gabriele De Chiara, Tommaso Calarco, Giovanna Morigi, and Simone Montangero. Full characterization of the quantum linear-zigzag transition in atomic chains. *Annalen der Physik*, 525(10-11):827–832, 2013.
- [SDH<sup>+</sup>12] Tomasz Sowiński, Omjyoti Dutta, Philipp Hauke, Luca Tagliacozzo, and Maciej Lewenstein. Dipolar molecules in optical lattices. *Phys. Rev. Lett.*, 108:115301, Mar 2012.
- [SMF11] Efrat Shimshoni, Giovanna Morigi, and Shmuel Fishman. Quantum zigzag transition in ion chains. *Phys. Rev. Lett.*, 106:010401, Jan 2011.
- [SRM<sup>+</sup>09] M. Sitte, A. Rosch, J. S. Meyer, K. A. Matveev, and M. Garst. Emergent lorentz symmetry with vanishing velocity in a critical two-subband quantum wire. *Phys. Rev. Lett.*, 102:176404, Apr 2009.
- [vAvEW<sup>+</sup>08] A. H. van Amerongen, J. J. P. van Es, P. Wicke, K. V. Kheruntsyan, and N. J. van Druten. Yang-yang thermodynamics on an atom chip. *Phys. Rev. Lett.*, 100:090402, Mar 2008.
- [Vid03] Guifré Vidal. Efficient classical simulation of slightly entangled quantum computations. *Phys. Rev. Lett.*, 91:147902, Oct 2003.
- [Vid04] Guifré Vidal. Efficient simulation of one-dimensional quantum many-body systems. *Phys. Rev. Lett.*, 93:040502, Jul 2004.
- [WC13] M L Wall, , and L D Carr. Dipole–dipole interactions in optical lattices do not follow an inverse cube power law. *New Journal of Physics*, 15(12):123005, 2013.

- [WD97] David J. Wales\* and Jonathan P. K. Doye. Global optimization by basin-hopping and the lowest energy structures of lennard-jones clusters containing up to 110 atoms. *The Journal of Physical Chemistry A*, 101(28):5111–5116, 1997.
- [WPA<sup>+</sup>12] Cheng-Hsun Wu, Jee Woo Park, Peyman Ahmadi, Sebastian Will, and Martin W. Zwierlein. Ultracold fermionic feshbach molecules of  $^{23}\text{Na}^{40}\text{K}$ . *Phys. Rev. Lett.*, 109:085301, Aug 2012.



---

## Acknowledgments

---

At this point I would like to thank all the people who made this thesis possible.

I would like to express my deep gratitude to my supervisors Prof. Giovanna Morigi and Dr. Anna Minguzzi for making this joint dissertation a possibility. They offered patient guidance, enthusiastic encouragement and useful critique of this research work and have helped me to finish this great scientific project.

I would like to thank Ferdinand Tschirsich, Dr. Pietro Silvi and Prof. Simone Montangero for their hospitality at the University of Ulm and them introducing me to matrix product states and the fruitful discussions about physics.

My grateful thanks are also extended to André Winter for the helpful and stimulating discussions about path integral Monte Carlo methods and long-range interactions.

I would also like to thank all the people in the LPMMC in Grenoble and the theoretical quantum physics group in Saarbrücken for a welcoming and stimulating atmosphere. In particular, I would like to thank Eiji Kawasaki for great conversations about physics and pleasant time working together. A special thanks goes to Stefan Schütz and Andreas Buchheit for helping me in the last stages of the thesis with organizational problems and proofreading. I would also like to thank Ralf Betzholz for helping with Mathematica and Latex problems on many occasions.